SeaWiFS Technical Report Series

Stanford B. Hooker and Elaine R. Firestone, Editors

Volume 13, Case Studies for SeaWiFS Calibration and Validation, Part 1

Charles R. McClain, Josefino C. Comiso, Robert S. Fraser, James K. Firestone, Brian D. Schieber, Eueng-nan Yeh, Kevin R. Arrigo, and Cornelius W. Sullivan

NASA Technical Memorandum 104566, Vol. 13

SeaWiFS Technical Report Series

Stanford B. Hooker, Editor
NASA Goddard Space Flight Center
Greenbelt, Maryland

Elaine R. Firestone, Technical Editor
General Sciences Corporation
Laurel, Maryland

Volume 13, Case Studies for SeaWiFS Calibration and Validation, Part 1

Charles R. McClain, Josefino C. Comiso, Robert S. Fraser
NASA Goddard Space Flight Center
Greenbelt, Maryland

James K. Firestone, Brian D. Schieber, and Eueng-nan Yeh
General Sciences Corporation
Laurel, Maryland

Kevin R. Arrigo
Oak Ridge Institute for Science and Education
Oak Ridge, Tennessee

Cornelius W. Sullivan
University of Southern California
Los Angeles, California

National Aeronautics and
Space Administration

Goddard Space Flight Center
Greenbelt, Maryland 20771

1994

PREFACE

The Sea-viewing Wide Field-of-view Sensor (SeaWiFS) Calibration and Validation Program has a broad spectrum of responsibilities as outlined in Volume 3 of the *SeaWiFS Technical Report Series* (McClain et al. 1992a). The four primary functions of the program are 1) bio-optical algorithm development, 2) atmospheric correction algorithm development, 3) sensor calibration and characterization, and 4) product verification and quality control. Each of these categories encompass a number of activities presently underway at the National Aeronautics and Space Administration's (NASA) Goddard Space Flight Center (GSFC), and within the science community as supported by contracts and grants from the SeaWiFS Project and NASA Headquarters. The SeaWiFS Project places great emphasis on documentation of its development activities through volumes in the *SeaWiFS Technical Report Series* and the refereed literature, e.g., Hooker et al. 1993. Other volumes of the series published under Calibration and Validation Program support include Volumes 4 (McClain et al. 1992b), 5 (Mueller and Austin 1992), 7 (Darzi 1992), 10 (Woodward et al. 1993), and 14 (Mueller 1993). Because many of the studies and other activities undertaken by the Calibration and Validation Program are not extensive enough to require dedicated volumes of the series, it was decided to publish volumes composed of brief chapters. Volume 13 is the first in a set of such volumes.

The Calibration and Validation Program relies on the outside research community for the bio-optical and atmospheric correction data collection, as well as for algorithm development, but does have the responsibility for evaluating and comparing the algorithms and for ensuring that the algorithms are properly implemented within the SeaWiFS Data Processing System. Volume 13 consists primarily of sensitivity and algorithm (bio-optical, atmospheric correction, and quality control) studies based on the Coastal Zone Color Scanner (CZCS) and historical ancillary data undertaken to assist in the development of SeaWiFS specific applications.

Greenbelt, Maryland   — C. R. McClain
June 1993

C. McClain, J. Comiso, R. Fraser, J. Firestone, B. Schieber, E. Yeh, K. Arrigo, and C. Sullivan

Table of Contents

Table of Contents *cont.*

C. McClain, J. Comiso, R. Fraser, J. Firestone, B. Schieber, E. Yeh, K. Arrigo, and C. Sullivan

ABSTRACT

Although the Sea-viewing Wide Field-of-view Sensor (SeaWiFS) Calibration and Validation Program relies on the scientific community for the collection of bio-optical and atmospheric correction data as well as for algorithm development, it does have the responsibility for evaluating and comparing the algorithms and for ensuring that the algorithms are properly implemented within the SeaWiFS Data Processing System. This report consists of a series of sensitivity and algorithm (bio-optical, atmospheric correction and quality control) studies based on Coastal Zone Color Scanner (CZCS) and historical ancillary data undertaken to assist in the development of SeaWiFS specific applications needed for the proper execution of that responsibility. The topics presented are as follows: 1) CZCS bio-optical algorithm comparison, 2) SeaWiFS ozone data analysis study, 3) SeaWiFS pressure and oxygen absorption study, 4) pixel-by-pixel pressure and ozone correction study for ocean color imagery, 5) CZCS overlapping scenes study, 6) a comparison of CZCS and *in situ* pigment concentrations in the Southern Ocean, 7) the generation of ancillary data climatologies, 8) CZCS sensor ringing mask comparison, and 9) sun glint flag sensitivity study.

Prologue

The purpose of the Sea-viewing Wide Field-of-view Sensor (SeaWiFS) Project is to obtain valid ocean color data of the world ocean for a five-year period, to process that data in conjunction with ancillary data to meaningful biological parameters, and to make that data readily available to researchers. The National Aeronautics and Space Administration's (NASA) Goddard Space Flight Center (GSFC) will develop a data processing and archiving system in conjunction with the Earth Observing Satellite Data and Information System (EOSDIS), which includes a ground receiving system, and will oversee a calibration and validation effort to ensure the integrity of the final products.

The Calibration and Validation Team (CVT) has three main tasks: calibration of the SeaWiFS instrument, development and validation of the operational atmospheric correction algorithm, and development and validation of the derived product algorithms, such as chlorophyll *a* concentration. Some of this work will be done internally at GSFC while the remainder will be done externally at other institutions. NASA and the Project place the highest priority on assuring the accuracy of derived water-leaving radiances globally, and over the entire mission. If these criteria are met, development of global and regional biogeochemical algorithms can proceed on many fronts. These activities are discussed in detail in *The SeaWiFS Calibration and Validation Plan* (McClain et al. 1992a).

Because many of the studies and other works undertaken with the program are not extensive enough to require dedicated volumes of the *SeaWiFS Technical Report Series*, the CVT has decided to publish volumes composed of brief, but topically specific, chapters. Volume 13 is the first in a set of such volumes and consists primarily of sensitivity and algorithm (bio-optical, atmospheric correction, and quality control) studies based on CZCS and historical ancillary data undertaken to assist in the development of SeaWiFS specific applications. A short synopsis of each chapter is given below.

1. CZCS Bio-optical Algorithm Comparison

Several pigment concentration algorithms developed for use with Coastal Zone Color Scanner (CZCS) data are described and compared. These include the standard two-channel switching algorithm of Gordon et al. (1983), an iterative algorithm by Smith and Wilson (1981), a three-channel algorithm by D. Clark (Muller-Karger et al. 1990) and an algorithm developed by the European community for the reprocessing of CZCS data from European waters.

2. SeaWiFS Ozone Data Analysis Study

Sensitivity analyses are performed on CZCS imagery to simulate the impact of erroneous estimates of ozone optical thickness on satellite derived water-leaving radiances and pigment concentrations. Time series of total ozone from the Total Ozone Mapping Spectrometer (TOMS) provide an indication of the spatial and temporal variability within a CZCS scene.

3. SeaWiFS Pressure and Oxygen Absorption Study

Sensitivity analyses are performed on CZCS imagery to simulate the impact of erroneous estimates of Rayleigh optical thickness on satellite derived water-leaving radiances and pigment concentrations. Time series of sea level pressure from the National Meteorological Center (NMC) provide an indication of the spatial and temporal variability within a CZCS scene.

4. Pixel-by-Pixel Pressure and Ozone Correction Study for Ocean Color Imagery

Sensitivity analyses are performed on CZCS imagery to estimate the impact of erroneous estimates of Rayleigh and ozone optical thicknesses on satellite derived pigment concentrations.

5.   CZCS Overlapping Scenes Study

Two coincident scenes from consecutive CZCS orbits are analyzed to investigate the consistency of the derived products under differing satellite and solar azimuth and zenith angles. The Miami DSP CZCS edge mask algorithm is described.

6.   A Comparison of CZCS and In Situ Pigment Concentrations in the Southern Ocean

The large-scale distribution of pigments in the Southern Ocean, as viewed from the CZCS, shows extensive blooms and enhanced pigments which are distributed asymmetrically about the Antarctic continent. Comparative analysis with an extensive database of historical *in situ* data reveals that the magnitude of these enhanced pigments may actually be 1.8 times higher than previously reported. Pigment concentrations are computed using a new Southern Ocean CZCS algorithm adjusted to reflect regional differences in bio-optical properties of the water column and compared to estimates made using an extensive database of *in situ* pigment data.

7.   The Generation of Ancillary Data Climatologies

The method used for generating monthly climatological averages computed on a global basis, of wind speed, total ozone, atmospheric pressure, and relative humidity at the ocean surface is described. The calibration and validation element has computed the climatologies, and placed the results in a separate file in the National Center for Supercomputing Applications (NCSA) Hierarchical Data Format (HDF) for each of the ancillary parameters. This chapter describes the method used for the generation of the climatologies.

8.   CZCS Sensor Ringing Mask Comparison

Three different methods for handling CZCS bright target recovery are described and compared using a CZCS test scene from the Bering Sea. The three techniques are the Mueller (Mueller 1988), the SEAPAK (McClain et al. 1991a and 1991b and Brock et al. 1991) and the Miami DSP (Evans and Gordon 1993) methods.

9.   Sun Glint Flag Sensitivity Study

The statistical wind speed dependent surface slope distribution of Cox and Munk (1954a and 1954b) is used to estimate the sun glint affected area in a CZCS image. The probability of a pixel being contaminated by glitter is a function of sea surface wind speed and satellite viewing geometry. In the sample case presented, the areal extent of the flag expands very little as wind speed increases beyond about $7\,\mathrm{m\ s^{-1}}$.

C. McClain, J. Comiso, R. Fraser, J. Firestone, B. Schieber, E. Yeh, K. Arrigo, and C. Sullivan

Chapter 1

CZCS Bio-optical Algorithm Comparison

Charles R. McClain
NASA Goddard Space Flight Center, Greenbelt, Maryland

Eueng-nan Yeh
General Sciences Corporation, Laurel, Maryland

Abstract

Several pigment concentration algorithms developed for use with CZCS data are described and compared. These include the standard two-channel switching algorithm of Gordon et al. (1983), an iterative algorithm by Smith and Wilson (1981), a three-channel algorithm by D. Clark (Muller-Karger et al. 1990) and an algorithm developed by the European community for the reprocessing of CZCS data from European waters. The first three produce the greatest similarity because they are based on the NIMBUS Experiment Team (NET) data set (Clark 1981).

1.1 INTRODUCTION

The total radiance received by the CZCS is governed by the following equation:

$$L_t(\lambda_i) = t(\lambda_i)L_W(\lambda_i) + L_r(\lambda_i) + L_a(\lambda_i) \qquad (1)$$

where λ_i=443, 520, 550, and 670 nm, respectively for i=1–4; L_t is the total radiance; L_W is the water-leaving radiance; L_r is the Rayleigh radiance, L_a is the aerosol radiance, and t is the diffuse transmittance of the atmosphere. For a given satellite viewing geometry, L_r can be calculated from the multiple scattering radiative transfer theory (Gordon et al. 1988). $L_a(\lambda_i)$, is related to $L_a(670)$ by the expression:

$$
\begin{aligned}
S(\lambda_i) &= \frac{L_a(\lambda_i)}{L_a(670)} \\
&= \frac{F_0(\lambda_i)\,T_{\text{oz}}(\lambda_i)}{F_0(670)\,T_{\text{oz}}(670)}\left(\frac{\lambda}{670}\right)^{n(\lambda_i)},
\end{aligned}
\qquad (2)
$$

where $n(\lambda_i)$ is conceptually similar to the Ångström exponent (Ångström 1964), F_0 is the incident solar irradiance, and T_{oz} is the diffuse transmittance of ozone. Making use of (2), (1) becomes

$$t(\lambda_i)L_W(\lambda_i) = L_t(\lambda_i) - L_r(\lambda_i) - S(\lambda_i)L_a(670). \quad (3)$$

The water-leaving radiance, L_W, can be converted to subsurface water radiance L_s using

$$L_s(\lambda_i) = \frac{m^2 L_W(\lambda_i)}{1-\rho}, \qquad (4)$$

where m is the index of refraction and ρ is the Fresnel reflectivity.

1.2 METHODOLOGIES

The system described in (3), consists of 4 equations (for the first 4 CZCS bands) and 5 unknowns, i.e., $L_W(\lambda_i)$, i=1–4, and $L_a(670)$, if the $n(\lambda_i)$ terms are specified. To close the system and enable a solution, an additional condition is required and the various algorithms employ different approaches in doing so. If the $n(\lambda_i)$ terms are not specified, more conditions must be assumed.

1.2.1 Gordon et al. Method

Gordon et al. (1983) proposed a total absorption condition at 670 nm, i.e., $L_s(670)$=0. This is a reasonable assumption for most low pigment Case 1 (Morel and Prieur 1977) waters where the optical characteristics are dominated by phytoplankton and their covarying detrital material. Fig. 1 is a schematic of the Gordon et al. method.

Usually, the $n(\lambda_i)$ terms are assumed to be 0.12, 0.00, and 0.00, for 443, 520, and 550 nm, respectively, which are typical marine haze values. If the $n(\lambda_i)$ terms are variable, then assumptions on clear water radiances at 520 and 550 nm (Gordon and Clark 1981) can be assumed for low pigment pixels and the $n(\lambda_i)$ terms can be estimated. Examples of studies where the $n(\lambda_i)$ terms were derived on a scene-by-scene basis are Barale et al. (1986), Banse and McClain (1986), McClain et al. (1988), and Muller-Karger et al. (1989). Brock et al. (1991) and Brock and McClain (1992) used the same principle to derive summer mean $n(\lambda_i)$ terms for the Arabian Sea.

The pigment concentration algorithms utilize ratios of $L_s(\lambda_i)$ which are interchangable with ratios of $L_W(\lambda_i)$ because, the index of refraction and Fresnel reflectivity are essentially independent of wavelength over this spectral range and cancel out. The bio-optical relation between pigment concentration, C, and the subsurface water radiances of CZCS bands 1, 2, and 3 proposed by Gordon et al. has two branches where each branch uses an algorithm based on a ratio of water-leaving radiances, i.e., $L_W(443)/L_W(550)$ or $L_W(520)/L_W(550)$. Formulations using these bands and radiance ratios are as follows:

$$C_{13} \;=\; 1.1298 \left[\frac{L_W(443)}{L_W(550)} \right]^{-1.71} \tag{5}$$

and

$$C_{23} \;=\; 3.3266 \left[\frac{L_W(520)}{L_W(550)} \right]^{-2.40}, \tag{6}$$

where the C subscripts indicate the bands used. These algorithms are developed from field observations from the waters of the US East and West Coasts, the Gulf of Mexico, and also the Sargasso Sea waters.

The C_{13} algorithm is primarily used for low chlorophyll concentration waters (Case 1) whereas the C_{23} algorithm encompasses both Case 1 and Case 2 waters. The C_{13} algorithm is used when C_{13} is less than $1.5\,\mathrm{mg\,m^{-3}}$ or when C_{13} is greater than $1.5\,\mathrm{mg\,m^{-3}}$, but C_{23} is less than $1.5\,\mathrm{mg\,m^{-3}}$; otherwise, C_{23} is used.

In SEAPAK, a PC-based image processing and analysis package developed at GSFC (McClain et al. 1991a and 1991b), if $L_s(443)$ is less than $0.15\,\mathrm{mW\,cm^{-2}\,\mu m^{-1}\,sr^{-1}}$, C_{23} is used. This is because spurious high pigment values can occur when the C_{23} switch condition is not satisfied. Imperfections in the switching criteria at $1.5\,\mathrm{mg\,m^{-3}}$ can distort the pigment frequency distribution; a three-channel algorithm (Muller-Karger et al. 1990) was developed by D. Clark (unpub.) to avoid this type of distortion:

$$C \;=\; 5.56 \left[\frac{L_s(443) + L_s(520)}{L_s(550)} \right]^{-2.252}. \tag{7}$$

1.2.2 Smith and Wilson Method

Smith and Wilson (1981) proposed an iterative approach based on the empirical equation:

$$L_s(670) \;=\; 0.08291 L_s(443) \left[\frac{L_s(443)}{L_s(550)} \right]^{-1.661} \tag{8}$$

in order to avoid the assumption that $L_s(670) = 0$ which is particularly unrealistic for coastal waters where pigment and sediment concentrations are high (Case 2 waters). In the SEAPAK implementation of the algorithm, the pigment concentrations are calculated using (5) and (6) rather than the pigment algorithms proposed by Smith and Wilson. Their method is illustrated in Fig. 2.

1.2.3 European Method

The so-called *European* method (Bricaud and Morel 1987, Andre and Morel 1991, Andersen 1991, and Sturm 1993) has been developed by the Ocean Colour European Archive Network (OCEAN) project, an initiative of the Joint Research Center (JRC) of the Commission of the European Communities (CEC) and of the European Space Agency (ESA), for the purpose of processing CZCS data in regions adjacent to the European continent. The atmospheric correction and bio-optical algorithms are significantly different than those described above. Starting with (1), terms are normalized as reflectances, R, and the system of equations become:

$$\begin{aligned} \dot{R}_t(\lambda_i) \;&=\; R_s(\lambda_i) \;+\; \dot{R}_a(\lambda_i) \\ &=\; R_s(\lambda_i) \;+\; G(\lambda_i)\dot{R}_a(670), \end{aligned} \tag{9}$$

where $\dot{R}_t = (R_t - R_r)/(qT_{2r})$, $\dot{R}_a = R_a/(qT_{2r})$, and R_s is the subsurface reflectance, T_{2r} is the two-way diffuse transmittance for Rayleigh attenuation, q is the water transmittance factor, and

$$\begin{aligned} G(\lambda_i) \;&=\; \frac{\dot{R}_a(\lambda_i)}{\dot{R}_a(670)} \\ &=\; \frac{T_{2r}(670)}{T_{2r}(\lambda_i)} \left(\frac{670}{\lambda} \right)^{\gamma}, \end{aligned} \tag{10}$$

where γ is the Ångström exponent and is independent of wavelength. A system of four equations with five unknowns is given by (9): $R_s(\lambda_i)$, i=1–4 and γ.

Empirical relations (derived from third-order polynomial curve fits) between $R_s(670)$ and the reflectance ratios, $R_s(443)/R_s(550)$ and $R_s(520)/R_s(550)$, are introduced to complete the nonlinear system. The approach is illustrated in Fig. 3. It is iterative, operates on each pixel to determine γ, and, through a sequence of reflectance value tests, categorizes the pixel as Case 1 low pigment, Case 1 high pigment, or Case 2. The method assumes the following initial conditions: γ is any specified value, $R_s(670) = 0$, and the pixel is assumed to be Case 1 low pigment. The iteration incorporates convergence tests for $R_s(670)$ and γ (Case 1 only). A test for Case 2 water using $R_s(550)$ is applied and, if satisfied, the calculation branches to the Case 2 water algorithm.

Pigment concentrations are derived from a third order polynomial function of $R_s(443)/R_s(550)$ for Case 1 low pigment concentrations. A pigment concentration test for low concentration Case 1 water is performed and, if the test fails, the calculation branches to the Case 1 high pigment concentration algorithm. Once beyond these two tests, an Ångström convergence test is applied. If the convergence criterion is satisfied, the final reflectances, pigment concentration, and γ values are output; if not satisfied, the calculation initiates another iteration using the computed Ångström exponent.
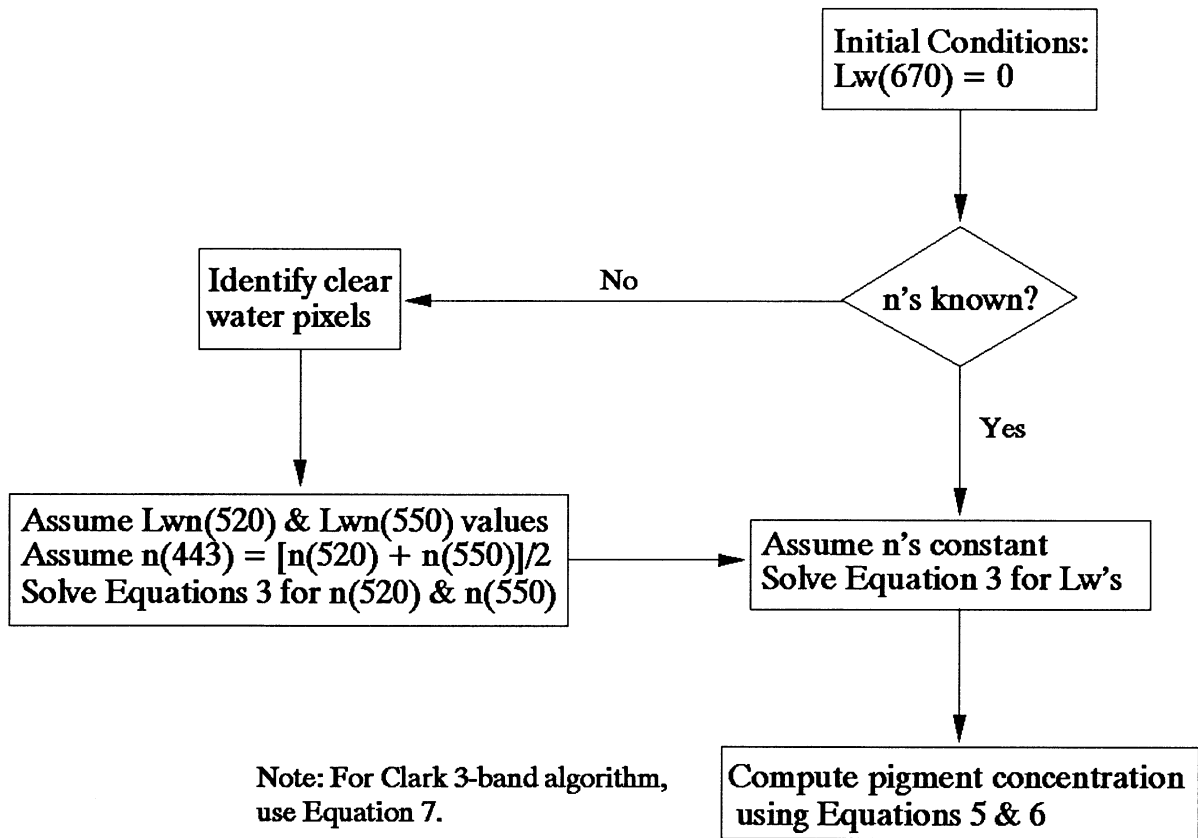
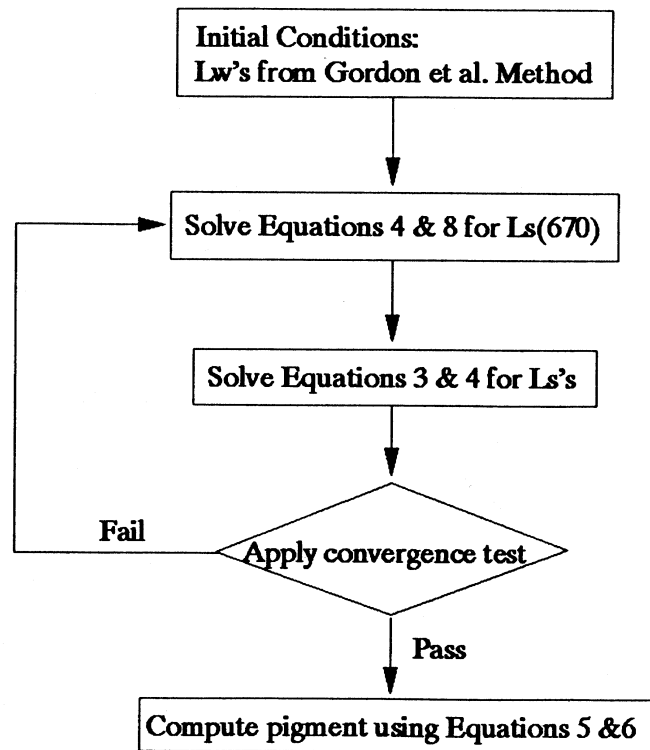**Fig. 1.** Flow diagram for the Gordon et al. (1983) algorithm.

Fig. 2. Flow diagram for the Smith and Wilson (1981) algorithm.

Fig. 3. Flow diagram for the European methods.

C. McClain, J. Comiso, R. Fraser, J. Firestone, B. Schieber, E. Yeh, K. Arrigo, and C. Sullivan
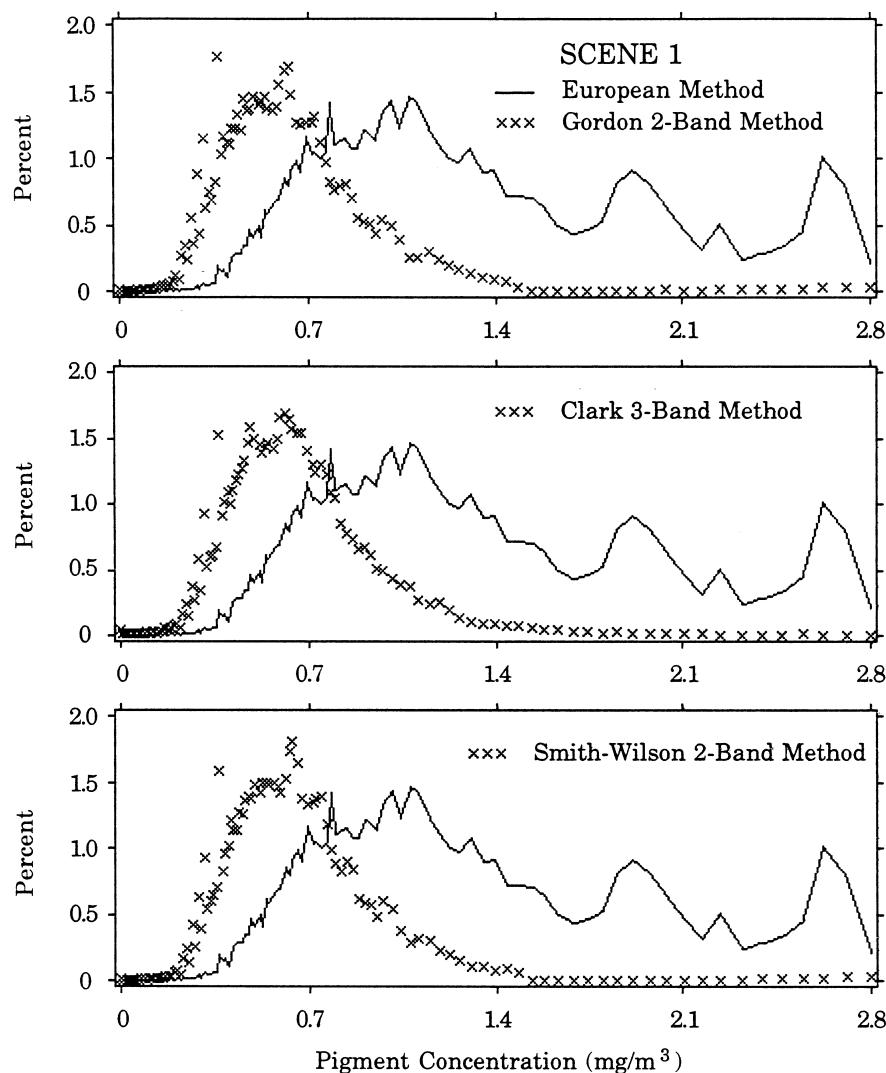
Fig. 4. Histograms among Gordon 2-band, Clark 3-band, Smith-Wilson, and European methods.

Similar procedures apply to Case 1 high chlorophyll pixels except the pigment algorithm which is a function of the ratio $R_s(520)/R_s(550)$. The iteration branches the Case 2 algorithm if $R_s(550)$ exceeds a predefined threshold value or the derived pigment is greater than or equal to $10\,\text{mg}\,\text{m}^{-3}$.

For a Case 2 pixel, the subsurface reflectance will be estimated using a specified value of the Ångström exponent, i.e., no iteration on γ. The iteration scheme is applied only using an $R_s(670)$ convergence test. The pigment concentration is derived from either a polynomial relation based on $R_s(520)/R_s(550)$ or $R_s(443)/R_s(550)$ depending on whether or not $R_s(443)$ is greater than the threshold value of 0.4.

1.3 RESULTS

The algorithms discussed above were implemented in SEAPAK and applied to two CZCS scenes. Under these comparisons, the Rayleigh optical thicknesses (0.237, 0.123, 0.098, and 0.044 for 443, 520, 550, and 670 nm, respectively) were assumed to be constants for both scenes. With the exception of the European method, the $n(\lambda_i)$ exponents were assumed to be constants (0.12, 0.00, and 0.00 for 443, 520, and 550 nm, respectively). The ozone value used was the TOMS data located nearest to the center pixel in the scene. These were the standard values used in the global CZCS processing (Esaias et al. 1986 and Feldman et al. 1989).

Plate 1 (orbit 8,889, 28 July 1980, sequential day 210) depicts the pigment concentrations derived from the different algorithms. The scene center ozone value is 385 Dobson units (DU). The Ångström exponent γ derived from the European method is illustrated in Plate 2 which varies significantly from location to location. The histograms in Fig. 4 and the pigment values in Table 1 indicate the European algorithm produces less pigment variability, but higher mean pigment values than the other algorithms,
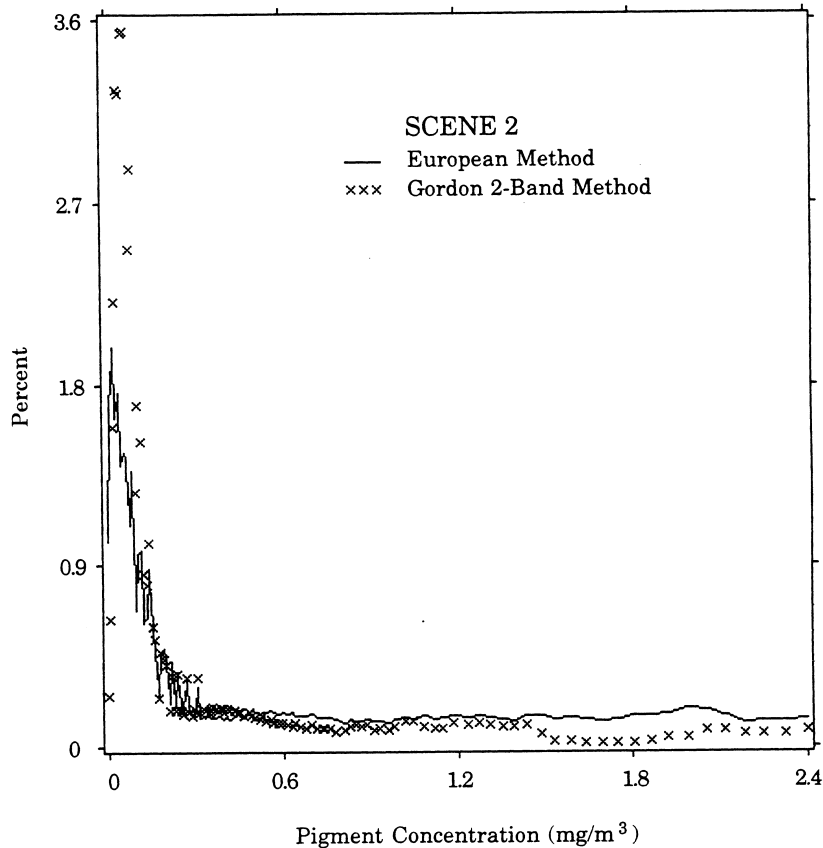
Fig. 5. Pigment frequency distributions produced using the Gordon et al. 2-band and European methods for scene 2 (Plate 3).

i.e., approximately 1.75 times higher than the other algorithms. Also, the Gordon et al. 2-band, Clark 3-band, and Smith and Wilson algorithms produced consistently similar results.

Table 1. Pigment mean, μ, and standard deviation, σ, for the Norwegian Sea scene (Plate 1, orbit number 8,889). The means are in units of mg m^{-3}.

Value	Gordon-2	Clark-3	Smith-Wilson	European
μ	0.717	0.705	0.688	1.248
σ	1.686	1.581	1.191	0.790

The second scene, Plate 3, is an East Coast scene (orbit 5,106, 28 October 1979, sequential day 301) with a scene center ozone value of 313 DU. Two methods, the Gordon 2-channel and the European, were compared. As in the previous scene, the γ value (Plate 4) varied significantly within the scene. Table 2 compares the standard deviations and mean pigment concentrations between these two methods for the second scene. The European algorithm mean pigment value was 29% greater than that derived using the Gordon et al. 2-band algorithm while the standard deviations between the two were comparable. The pigment frequency distributions for the two algorithms are shown in Fig. 5.

Table 2. Pigment mean, μ, and standard deviation, σ, for the US East Coast scene (Plate 3, orbit number 5,106). The means are in units of mg m^{-3}.

Value	Gordon-2	European
μ	0.637	0.823
σ	1.822	1.782

1.4 CONCLUSIONS

Four different CZCS pigment algorithms were compared in one case and two in a second case. In the former, the differences among the Gordon et al. 2-band switching, the Clark 3-band non-switching, and the Smith and Wilson iterative algorithms produced similar results. This is not surprising because all are based on the same bio-optical data used for computing pigment concentration. The pigment concentrations derived from the European method averaged about 30–175% higher than the other methods. Scene 2 statistics are heavily weighted by the large number of low pigment pixels which should produce more favorable comparisons because of the relative simplicity of the optical properties of the Gulf Stream as compared to scene 1. The Ångström exponents derived using the European algorithm varied significantly within both scenes with ranges greater than would be expected.

C. McClain, J. Comiso, R. Fraser, J. Firestone, B. Schieber, E. Yeh, K. Arrigo, and C. Sullivan

Chapter 2

SeaWiFS Ozone Data Analysis Study

CHARLES R. MCCLAIN
NASA Goddard Space Flight Center, Greenbelt, Maryland

EUENG-NAN YEH
General Sciences Corporation, Laurel, Maryland

ABSTRACT

Ozone is a key parameter in the atmospheric correction of ocean color data because visible radiation is differentially absorbed as it passes into and out of the atmosphere. Sensitivity analyses are performed on CZCS imagery to simulate the impact of erroneous estimates of ozone optical thickness on the derived water-leaving radiances and pigment concentrations. Time series of total ozone from TOMS provide an indication of the spatial and temporal variability within a CZCS scene. It is concluded that the use of climatologies, e.g., monthly, would seriously compromise the primary objective of the SeaWiFS mission, i.e., estimation of surface oceanic chlorophyll to within 35%.

2.1 INTRODUCTION

The importance of ozone absorption of visible radiation was recognized early in the development of the CZCS atmospheric correction algorithm (Gordon 1978, Sørensen 1981, Sturm 1981, and Williams et al. 1985). Ozone absorbs differentially in the visible and has an absorption peak at 602 nm. In the standard CZCS atmospheric correction method (Gordon et al. 1983), the total radiance received by the CZCS is described by (1). The Rayleigh radiance, L_r, depends upon the geometric orientation between the sun, Earth, and satellite, and, for this analysis, $L_W(670)$ is assumed to be zero. $L_a(\lambda_i)$ is related to $L_a(670)$ through the expression

$$L_a(\lambda_i) \; \propto \; \left(\frac{\lambda_i}{670} \right)^{n(\lambda_i)} L_a(670), \qquad (11)$$

where $n(\lambda_i)$ is conceptually similar to the Ångström exponent. In the expressions for t, $L_a(\lambda_i)$ and $L_r(\lambda_i)$, ozone optical thickness appears explicitly. Therefore, errors in the estimation of ozone concentration propagate throughout all components of the correction in a nonlinear manner.

As discussed in Williams et al. (1985), Sørensen (1981), and Sturm (1981), the original correction scheme assumed climatological values of ozone optical thickness based on season and latitude range. This procedure was used in the early NIMBUS Project processing. However, during the global CZCS processing (Esaias et al. 1986 and Feldman et al. 1989), each scene was processed using a single ozone concentration value from the gridded TOMS data

for the same day. The value used was the TOMS value located nearest to the center pixel of the first scan line. A two-minute CZCS scene covered an area of approximately 1,600 km (along scan) by 800 km (along track). While it was known that errors in the ozone concentration were significant, André and Morel (1989) were the first to publish sensitivity studies which quantified the magnitude of the errors. They found that errors in ozone concentration within the natural range of variability (± 50 DU) could result in errors in the estimated pigment concentration of at least 25% at low concentrations and exceed 100% at concentrations above 8 mg m^{-3}.

The SeaWiFS objectives are to quantify chlorophyll a concentrations to within 35% over the range of 0.05–50 mg m^{-3} (Hooker et al. 1992). The work of André and Morel is strictly theoretical. The purpose of this report is to use the operational CZCS algorithm on a sample scene to actually show the effects on level-2 products. It must be noted that SeaWiFS will use algorithms very similar to those developed for the CZCS, but the instrument will quantify radiances much more precisely due to its 10-bit quantitization (CZCS was 8-bit) and higher signal-to-noise ratios (greater by approximately a factor of two).

2.2 DATA ANALYSIS

The sample scene used was one from the US East Coast: orbit 5,106, 28 October 1979, sequential day 301 (McClain and Atkinson 1985). This scene includes coastal and open ocean water masses providing a wide range of surface pigment concentrations (approximately 0.1–10 mg m^{-3}). The
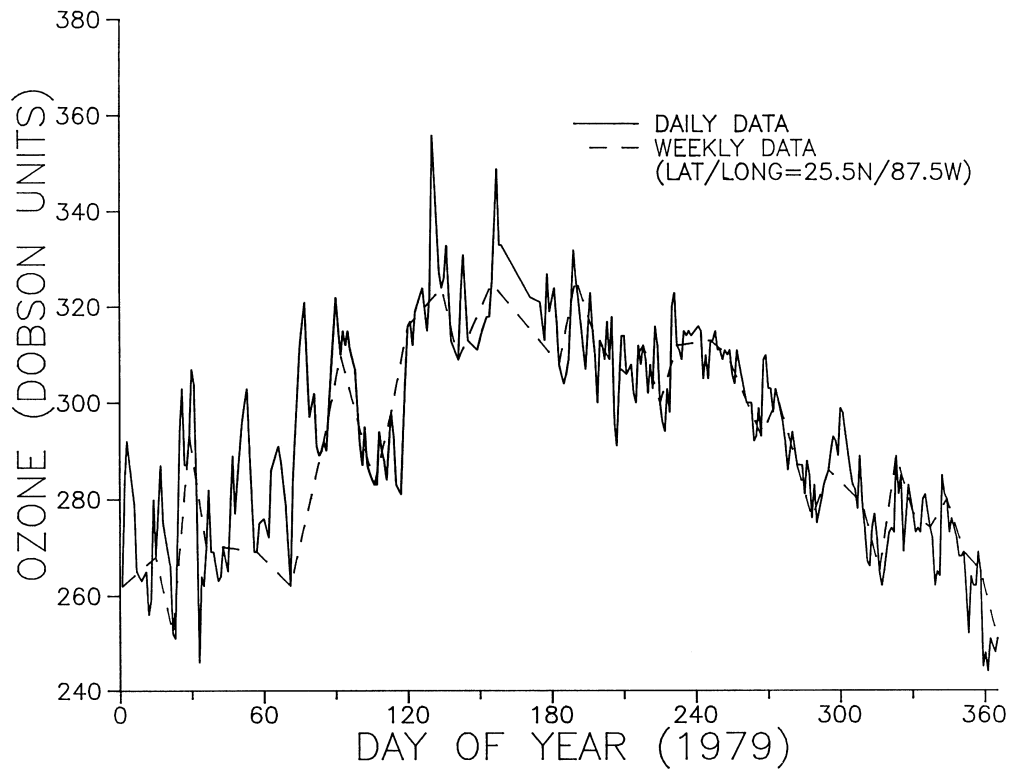
Fig. 6. 1979 time series of daily (solid line) and weekly (dashed line) values of ozone concentration at a point (87.5° W,25.5° N) within the CZCS scene.
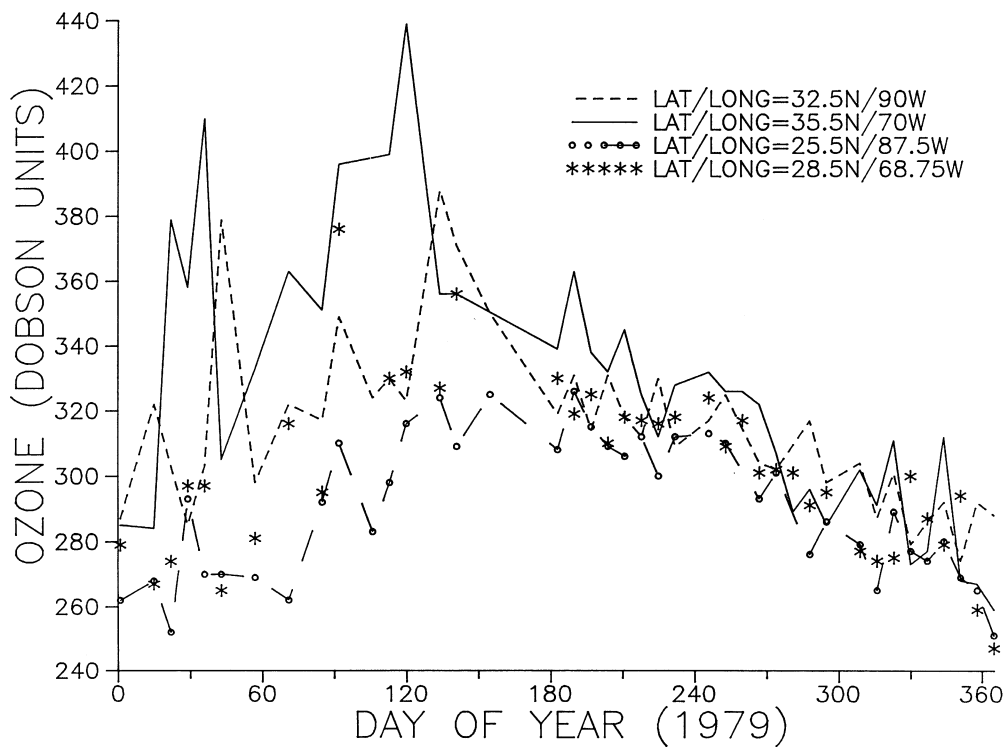
Fig. 7. 1979 time series of weekly values of ozone concentration at the four corners of the CZCS scene.

RT COMPONENT		Lt(443)	Lr(443)	La(443)	Lw(443)	Lt(550)	Lr(550)	La(550)	Lw(550)	Pigx10
226 DU		6.403	5.211	0.376	1.705	2.262	2.089	0.377	0.318	0.640
301 DU		6.403	5.208	0.385	1.693	2.262	2.056	0.380	0.380	0.880
376 DU		6.403	5.205	0.394	1.681	2.262	2.023	0.383	0.442	1.150

"n" exponents = (0.12, 0, 0)
for 443, 520 & 550 nm, respectively

Fig. 8. Comparison of values of terms in (1) at a low pigment concentration pixel for the three ozone concentrations. The data was obtained from orbit 5106 on 28 October 1979.

RT COMPONENT		Lt(520)	Lr(520)	La(520)	Lw(520)	Lt(550)	Lr(550)	La(550)	Lw(550)	Pigment
226 DU		3.207	2.506	0.457	0.490	2.602	1.918	0.438	0.496	2.362
301 DU		3.207	2.528	0.451	0.456	2.602	1.950	0.436	0.432	2.915
376 DU		3.207	2.550	0.445	0.424	2.602	1.983	0.433	0.369	3.420

"n" exponents = (0.12, 0, 0)
for 443, 520 & 550 nm, respectively

Fig. 9. Comparison of values of terms in (1) at a high pigment concentration pixel for the three ozone concentrations. The data was obtained from orbit 5106 on 28 October 1979.

RT COMPONENT		t(443)*	t(520)*	t(550)*	t(670)*	Lt(lc)	Lr(lc)	La(lc)	Lt(hc)	Lr(hc)	La(hc)
226 DU		0.0768	1.0400	2.0100	0.9040	1.0990	0.7820	0.3170	1.1110	0.7340	0.3760
301 DU		0.102	1.380	2.680	1.204	1.099	0.776	0.323	1.111	0.740	0.371
376 DU		0.128	1.730	3.350	1.504	1.099	0.771	0.328	1.111	0.746	0.365

* Values x 100
lc=low concentration, hc=high concentration

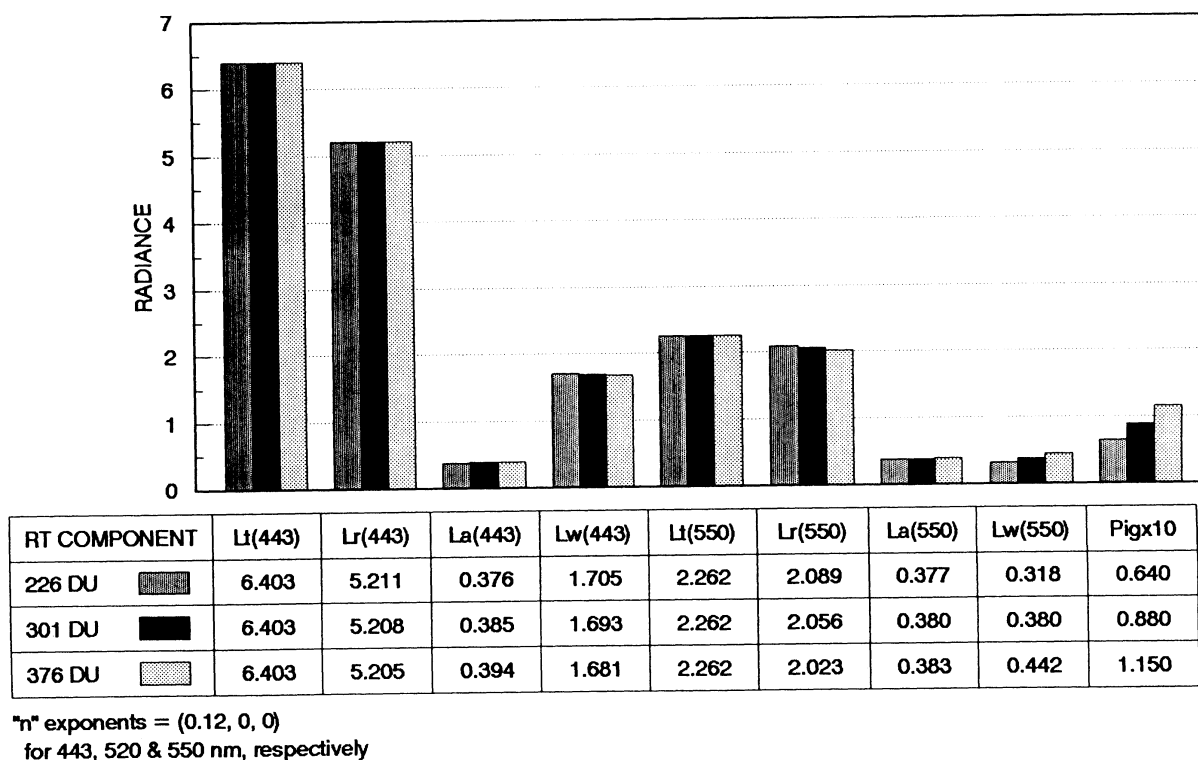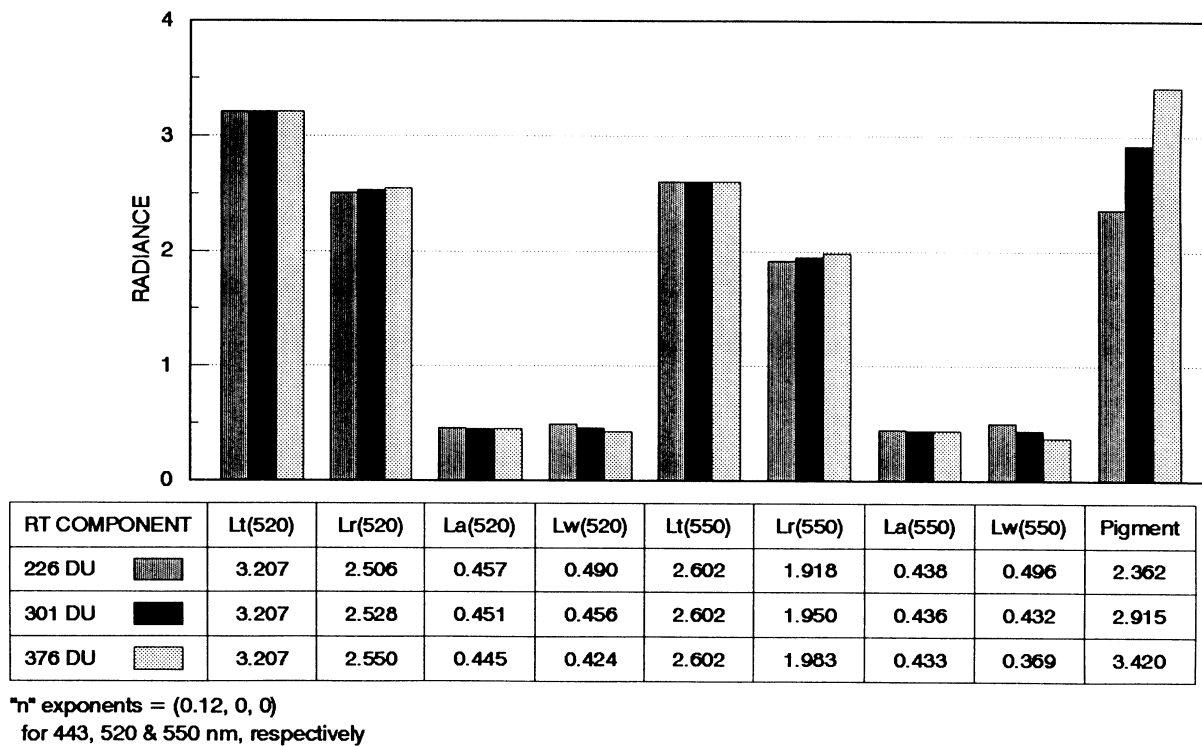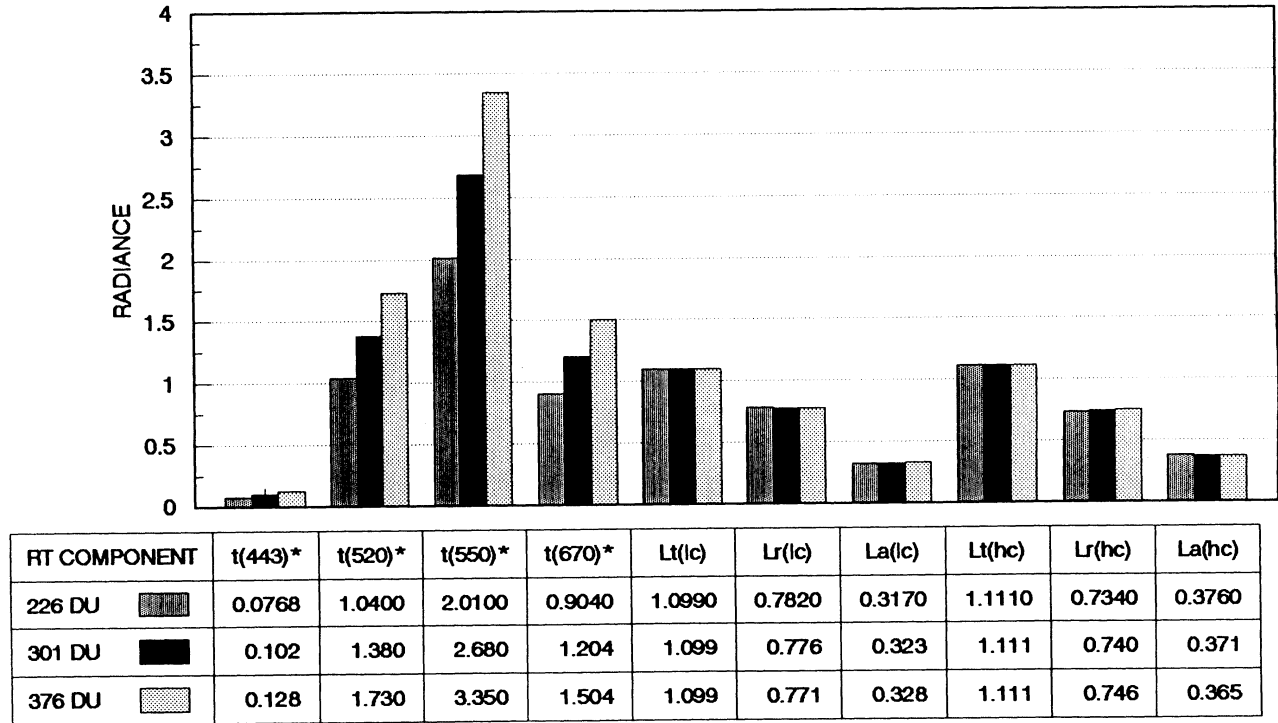**Fig. 10.** Comparison of ozone optical thicknesses and 670 nm radiance values for the terms in (1). Water-leaving radiance is assumed to be zero at 670 nm. The data was obtained from orbit 5106 on 28 October 1979.

scene was processed using the atmospheric correction algorithm of Gordon et al. (1988), the calibration of Evans (unpub.) used in the global CZCS processing, and three different ozone concentrations (226, 301, and 376 DU). The $n(\lambda_i)$ exponents used (0.12, 0.00, and 0.00 for 443, 520, and 550 nm, respectively) were those applied to all scenes processed during the global CZCS processing. The CZCS algorithm requires a fixed set of $n(\lambda_i)$ exponents be used for all pixels within a scene. Plate 5 provides the pigment products from the three analyses and the frequency distributions of log[pigment].

The 301 DU value corresponds to the TOMS value at the center of the scene. The other two values are 75% and 125% of the actual value, respectively. According to Bowman and Krueger (1985), the climatological mean value (October 1978 to September 1982) for this site is about 300 DU with an rms deviation of 30 DU. To examine the temporal variability at this location, Fig. 6 provides a one-year time series at a location within the scene. As can be seen, the daily fluctuations can be as large as 50 DU and the annual range is about 100 DU. In order to establish the spatial variability within a scene, Fig. 7 provides annual time series of weekly ozone concentrations (every seventh day) at the four corners of the scene. This information

indicates the spatial variability can exceed 100 DU.

To better understand how the terms in (1) vary as ozone concentration is varied given constant total radiances, two locations within the scene are used, one *low* concentration site and one *high* concentration site. Fig. 8 presents the low concentration example. Values for 443 nm and 550 nm are shown because these two wavelengths are used in the pigment concentration algorithm at concentrations below 1.5 mg m^{-3} (Gordon et al. 1983). Note that the pigment concentrations are multiplied by 10 in order to display the values in the graph. Fig. 9 presents the high concentration site values for 520 nm and 550 nm wavelengths because these wavelengths are used for concentrations above 1.5 mg m^{-3}. Note that the high concentration value of approximately 3.0 mg m^{-3} is still low compared to the range of values over which SeaWiFS is expected to perform accurately. These examples indicate how the small perturbations in the Rayleigh and aerosol radiances produce sizable changes in the derived water-leaving radiances and pigment concentrations. Fig. 10 provides a comparison of the ozone optical thicknesses and the terms in (1) for 670 nm at the low and high concentration pixels.

According to Bowman and Krueger (1985), the mid-latitude locations, such as the present case, have a moder-
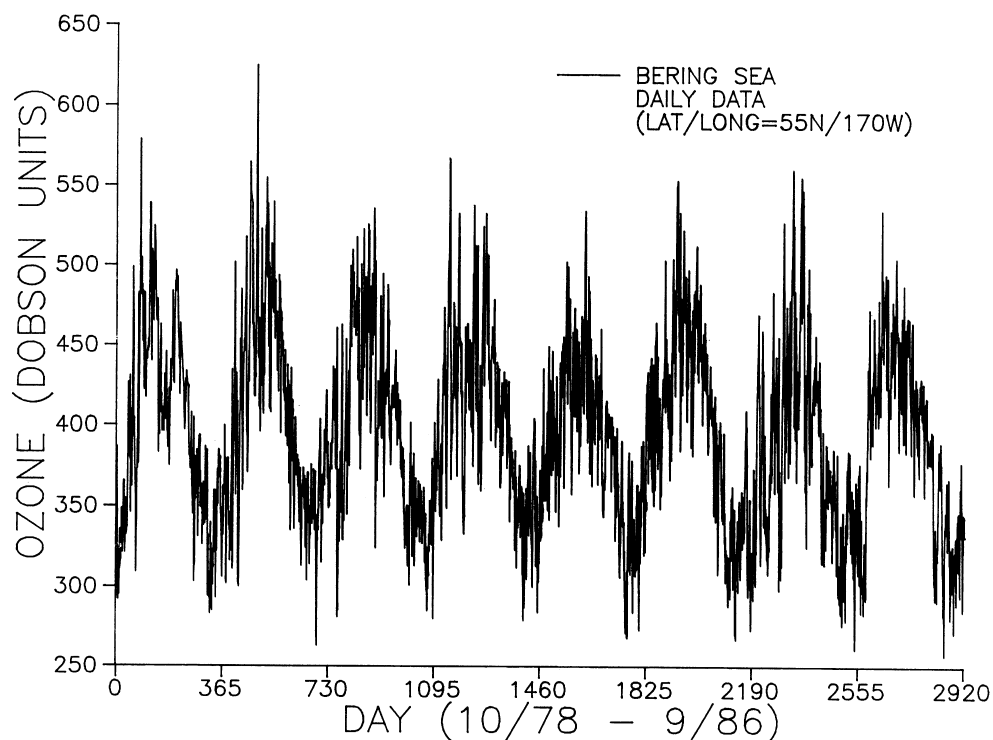
Fig. 11. Eight-year time series (October 1978 to September 1986) of ozone concentrations over the Bering Sea (170° W,55° N).
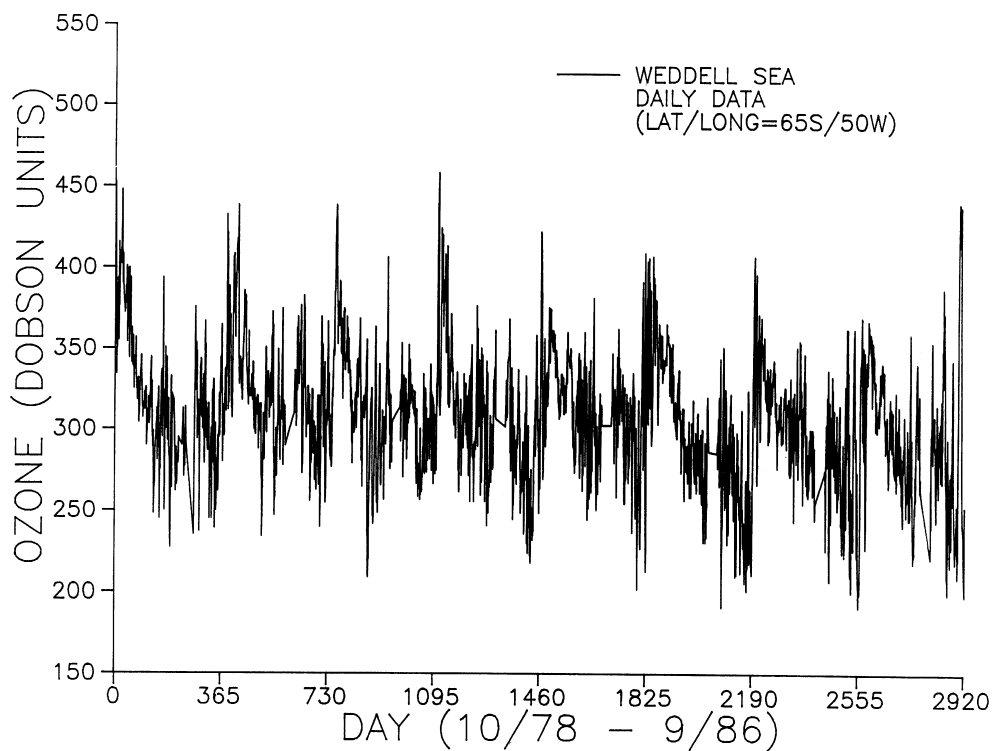

Fig. 12. Eight-year time series (October 1978 to September 1986) of ozone concentrations over the Weddell Sea (50° W,65° S). Data gaps are evident in the data and straight lines have been plotted across the gap.

ate level of ozone variability with the north polar regions having the highest mean and rms deviation values. The Bering Sea is one of the world's most biologically productive regions and is of particular interest to US fisheries.

Fig. 11 displays an eight-year time series of ozone concentration over the Bering Sea. The daily fluctuations are sizable even when compared to the amplitude of the well defined annual cycle. The Southern Ocean will also be of great interest because of the plans for Joint Global Ocean Flux Study (JGOFS) field studies (Anderson 1992) and because of concern about the impact of increased ultraviolet (UV) radiation on phytoplankton in the polar regions (Smith et al. 1992).

Fig. 12 is an eight-year time series of ozone concentrations over the Weddell Sea. The data from the Weddell Sea does not exhibit as strong an annual cycle as does the Bering Sea data, but it does indicate a downward trend with time. Certainly, studies of the impact of the ozone hole on primary production will require accurate estimates of zone concentration.

2.3 CONCLUSIONS

From the analyses presented, the temporal and spatial variability of total ozone is sufficiently great to require a pixel-by-pixel correction of SeaWiFS data if the chloro-phyll accuracy goals of the mission are to be met. Obviously, daily global ozone data will not be available at 4 km resolution. However, as demonstrated in Fig. 7, the spatial variability on scales of the order of a swath width is great enough to introduce chlorophyll concentration errors which exceed the $\pm 35\%$ mission objective. Thus, there would be no margin for error due to other error sources such as those introduced by deficiencies in the bio-optical and aerosol correction algorithms. The present operational TOMS grid has variable spatial resolution. It is recommended that ozone data with the finest spatial resolution available, e.g., $5°$, be used in the generation of all archived SeaWiFS products. To implement a pixel-by-pixel correction, an interpolation will be necessary. For quick-look processing in near-real time, climatological ozone values are perfectly adequate. However, observed values must be used for subsequent processings, the first of which will be approximately one month after data capture.

A major concern to the SeaWiFS Project is the availability of high quality daily ozone data: the NIMBUS-7 TOMS is no longer operational, the Pegasus TOMS launch has been cancelled, the Meteor TOMS is on an unstable platform, and the Upper Atmosphere Research Satellite (UARS) ozone products may not be of sufficient quality to meet the needs of the Project.

Chapter 3

SeaWiFS Pressure and Oxygen Absorption Study

CHARLES R. MCCLAIN
ROBERT S. FRASER
NASA Goddard Space Flight Center, Greenbelt, Maryland

EUENG-NAN YEH
General Sciences Corporation, Laurel, Maryland

ABSTRACT

Rayleigh scattering is a key factor in the atmospheric correction of ocean color data because visible radiation is differentially scattered as it passes into and out of the atmosphere. Sensitivity analyses are performed on CZCS imagery to simulate the impact of erroneous estimates of Rayleigh optical thickness on the derived water-leaving radiances and pigment concentrations. Time series of sea level pressure from the NMC provide an indication of the spatial and temporal variability within a CZCS scene. It is concluded that the use of climatologies, e.g., standard atmospheric surface pressure, P_0, would seriously compromise the primary objective of the SeaWiFS mission, i.e., estimation of surface oceanic chlorophyll to within 35%.

3.1 INTRODUCTION

The removal of the Rayleigh radiance from satellite observations of ocean color has always been a critical issue due to the strong wavelength dependence of the molecular scattering. Early studies (Curran 1972) indicated the feasibility of estimating ocean pigment concentrations from satellite measurements. Initially, the CZCS atmospheric correction algorithm was based on a single scattering Rayleigh model and a constant surface pressure, i.e., constant Rayleigh optical thicknesses (Gordon 1978, Sørensen 1981, Sturm 1981, Gordon et al. 1983, and Williams et al. 1985). Subsequent studies investigated and provided correction schemes for multiple Rayleigh scattering effects (Gordon and Castaño 1987 and Gordon et al. 1988). In the standard CZCS atmospheric correction method (Gordon et al. 1988), the total radiance is given by (1).

The Rayleigh radiance, which accounts for 80–90% of sensor received total radiance, depends upon air molecular number density and the orientation between the sun, Earth, and satellite and, therefore, is a function of surface pressure. Also, for this analysis, $L_W(670)$ is assumed to be zero. $L_a(\lambda_i)$ is related to $L_a(670)$ through the expression given in (30).

In the expressions for t, $L_a(\lambda_i)$, and $L_r(\lambda_i)$, Rayleigh optical thickness, τ_r, appears explicitly. The optical thickness is a physical quantity measuring the attenuation power of air molecules with respect to a specific wavelength of the incident light. The values of τ_{r0}, Rayleigh optical thickness at the standard atmospheric surface pressure, P_0, of

1,013.25 mb, used in CZCS atmospheric correction computations were 0.237 at 443 nm, 0.123 at 520 nm, 0.098 at 550 nm, 0.044 at 670 nm, and 0.0255 at 750 nm (Gordon et al. 1988). At any other surface pressure,

$$\tau_r = \tau_{r0}\left[1 + \frac{\Delta P}{P_0}\right], \qquad (12)$$

$$L_r = \frac{1 - \exp\left(-\tau_r/\mu\right)}{1 - \exp\left(-\tau_{r0}/\mu\right)}L_{r0}, \qquad (13)$$

where ΔP is the pressure deviation and μ is the cosine of the satellite zenith angle. Errors in the estimation of surface pressure propagate throughout all components of the correction in a nonlinear manner.

During the global CZCS processing (Esaias et al. 1986 and Feldman et al. 1989), each scene was processed using a single set of Rayleigh optical thickness values which were derived using the standard atmospheric surface pressure, P_0. A two-minute CZCS scene covered an area of approximately 1,600 km (along scan) by 800 km (along track). While it was known that errors due to variations in the surface pressure were significant, André and Morel (1989) were the first to publish sensitivity studies which quantified the magnitude of the errors. They found that errors in atmospheric pressure within the range of variability (± 15 mb) could result in errors in the estimated pigment concentration of at least 10% at low concentrations and exceed 100% at concentrations above 10 mg m^{-3}. The SeaWiFS Project objectives are to quantify chlorophyll

a concentrations to within 35% over the range of 0.05–50 mg m^{-3} (Hooker et al. 1992).

The work of André and Morel (1989) is strictly theoretical. The purpose of this report is to use the operational CZCS algorithm on a sample scene to actually show the effects on level-2 products. It must be noted that SeaWiFS will use algorithms very similar to those developed for the CZCS, but the instrument will quantify radiances much more precisely due to its 10-bit quantitization (CZCS was 8-bit) and higher signal-to-noise ratios (greater by approximately a factor of two).

3.2 DATA ANALYSIS

The sample scene used was one from the Icelandic waters (orbit 9,235, 22 August 1980, sequential day 235), which includes coastal and open ocean water masses providing a wide range of surface pigment concentrations (approximately 0.1–10 mg m^{-3}). The scene was processed using the atmospheric correction algorithm of Gordon et al. (1988), the calibration of Evans (unpub.) used in the global CZCS processing, and three different surface pressures (993, 1,013.25, and 1,033.5 mb). The $n(\lambda_i)$ exponents used (0.12, 0.00, and 0.00 for 443, 520, and 550 nm, respectively) were those applied to all scenes processed during the global CZCS processing. The CZCS algorithm requires that a fixed set of Ångström exponents be used for all pixels within a scene. Plate 6 provides the pigment products from the three analyses and the frequency distributions of log[pigment].

The 1,013.25 mb value corresponds to the standard atmospheric surface pressure used during the global CZCS processing. The other two values are 98% and 102% of the standard pressure, respectively. To examine the temporal variability at this location, Fig. 13 provides a one-year time series at a location within the scene. As can be seen, the daily fluctuations can be as large as 50 mb and the annual range is about 80 mb.

To better understand how the terms in (1) vary as surface pressure is varied, given constant total radiances, two locations within the scene are used, one *low* concentration site and one *high* concentration site. Fig. 14 presents the low concentration example. Values for 443 and 550 nm are shown because these two wavelengths are used in the pigment concentration algorithm at concentrations below 1.5 mg m^{-3} (Gordon et al. 1983). Note that the pigment concentrations are multiplied by 10 in order to display the values in the graph. Fig. 15 presents the high concentration site values for 520 and 550 nm wavelengths because these wavelengths are used for concentrations above 1.5 mg m^{-3}. Note that the high concentration value of approximately 4.0 mg m^{-3} is still low compared to the range of values over which SeaWiFS is expected to perform accurately.

These examples indicate how small perturbations in surface pressure affect the Rayleigh and aerosol radiances resulting in sizable changes in the derived water-leaving radiances and pigment concentrations. Note that in Fig. 15,

the pigment concentration for the 993 mb case was computed using the 443 nm water-leaving radiance because of algorithm switching. Had 520 nm been selected, the concentration would have been 3.72 mg m^{-3}. This points out that large errors in the derived pigment can result from a combination of surface pressure variability and algorithm switching effects. Fig. 16 provides the diffuse transmittances for the low pigment concentration case and the values of the terms in (1) for 670 nm (assuming $L_W(670)$ is zero) for both low and high pigment concentration cases.

3.3 OXYGEN ABSORPTION BAND

Oxygen in the Earth's atmosphere moderately absorbs radiant energy in a narrow band at 761 nm. Its absorption depends on the total optical path length, as determined by the solar zenith angle and direction of observation, that the solar radiation travels through the atmosphere and on the total amount of oxygen, with a 2σ variation of 2.5% in amount of oxygen.

The oxygen absorption band contains 61 absorption lines. The transmittance of the band, when computed for a narrow band of 6 cm^{-1} wave numbers or 0.35 nm, is shown in Fig. 17. The amount of air that the radiation travels through is two air masses, which is equivalent to the sun being at the zenith, traveling to the surface at a mean pressure of 1,013 mb, (shown in the bottom band) and then back up through the atmosphere towards the zenith. The minimum transmittance is 5% at 760 nm, and a secondary minimum of 30% at 763 nm. The band extends from 758–770 nm.

A convenient way of taking the transmittance of the oxygen into account for instrument design is to calculate the width of an equivalent band that would give complete absorption and compare that width with the bandwidth of a radiometer. The absorption, A, is given by

$$A(k) \;=\; 1 - t(k), \tag{14}$$

where $t(k)$ is the spectral transmission as a function of wave number k (cm^{-1}). The equivalent bandwidth, Δk, is computed by

$$\Delta k \;=\; \int_{k_1}^{k_2} A(k)\,dk, \tag{15}$$

where the integration is over the complete wavenumber band from $k_1 = 12{,}970$ cm^{-1} to $k_2 = 13{,}190$ cm^{-1}. Table 3 gives the equivalent widths for air masses 2 and 3 with a surface pressure of 1,013 mb.

Table 3. Equivalent widths for air masses 2 and 3 with a surface pressure of 1,013 mb.

Air Mass	$k \; [cm^{-1}]$	Width [nm]
2	80	4.6
3	89	5.2

C. McClain, J. Comiso, R. Fraser, J. Firestone, B. Schieber, E. Yeh, K. Arrigo, and C. Sullivan
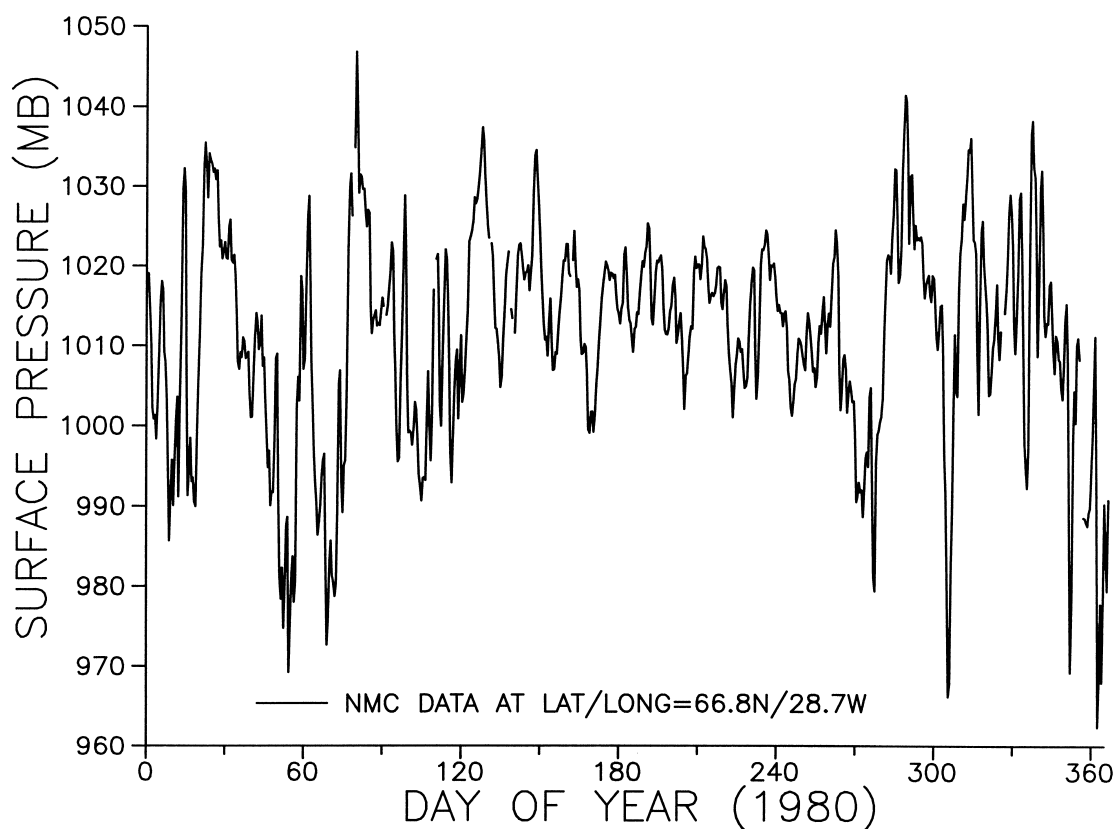
Fig. 13. 1980 time series of daily values of NMC surface pressure at a point within the CZCS scene.

		Lt(443)	Lr(443)	La(443)	Lw(443)	Lt(550)	Lr(550)	La(550)	Lw(550)	Pigx10
993 mb		5.262	4.549	0.214	0.575	2.204	1.782	0.177	0.241	2.560
1013 mb		5.262	4.629	0.197	0.504	2.204	1.816	0.188	0.221	2.770
1033 mb		5.262	4.709	0.181	0.432	2.204	1.850	0.172	0.201	3.060
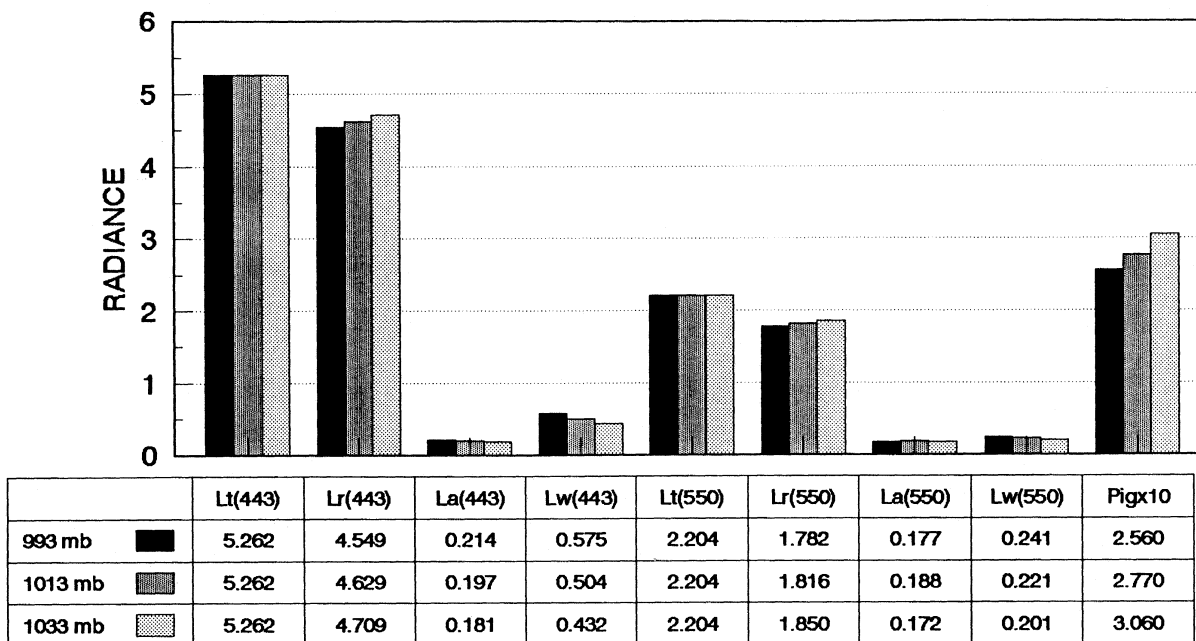
"n" exponents = (0.12,0,0)
for 443, 520 and 550 nm, respectively

Fig. 14. Comparison of values of terms in (1) at a low pigment concentration pixel for the three surface pressures. The data was obtained from orbit 9235 on 22 August 1980.

		Lt(520)	Lr(520)	La(520)	Lw(520)	Lt(550)	Lr(550)	La(550)	Lw(550)	Pig *
993 mb		2.886	2.297	0.214	0.405	2.352	1.757	0.205	0.424	1.196
1013 mb		2.886	2.341	0.198	0.376	2.352	1.791	0.190	0.405	3.983
1033 mb		2.886	2.385	0.182	0.347	2.352	1.825	0.174	0.385	4.302

"n" exponents = (0.12,0,0) for 443, 520 &
550 nm, respectively. * uses Lw(443) @ 993 mb.

Fig. 15. Comparison of values of terms in (1) at a high pigment concentration pixel for the three surface pressures. The data was obtained from orbit 9235 on 22 August 1980.

		t(443)*	t(520)*	t(550)*	t(670)*	Lt(lc)	Lr(lc)	La(lc)	Lt(hc)	Lr(hc)	La(hc)
993 mb		0.867	0.910	0.906	0.957	0.870	0.694	0.177	0.859	0.682	0.177
1013 mb		0.864	0.909	0.909	0.956	0.870	0.707	0.163	0.859	0.695	0.163
1033 mb		0.862	0.907	0.907	0.956	0.870	0.721	0.149	0.859	0.709	0.150

*low concentration case
lc=low concentration, hc=high concentration
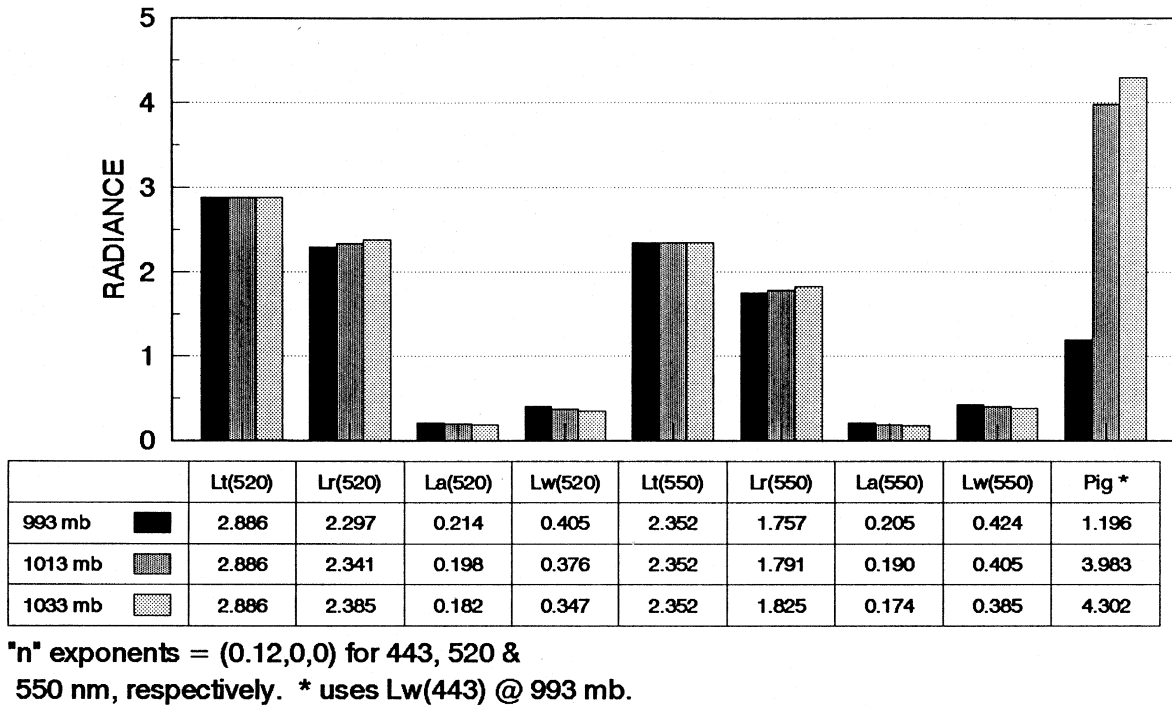
Fig. 16. Comparison of the diffuse transmittance values (1) for the low pigment concentration case and the values of the 670 nm terms in (1) for both the low and high pigment concentration cases. Water-leaving radiance is assumed to be zero at 670 nm. The data was obtained from orbit 9235 on 22 August 1980.

C. McClain, J. Comiso, R. Fraser, J. Firestone, B. Schieber, E. Yeh, K. Arrigo, and C. Sullivan

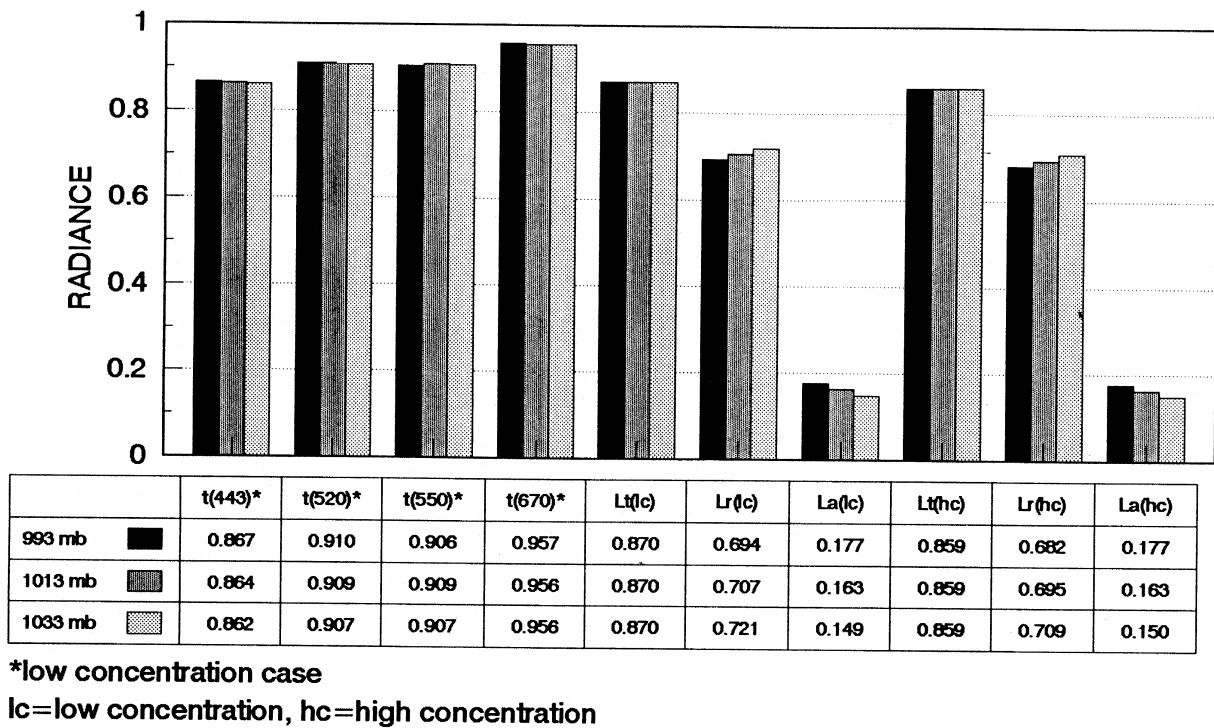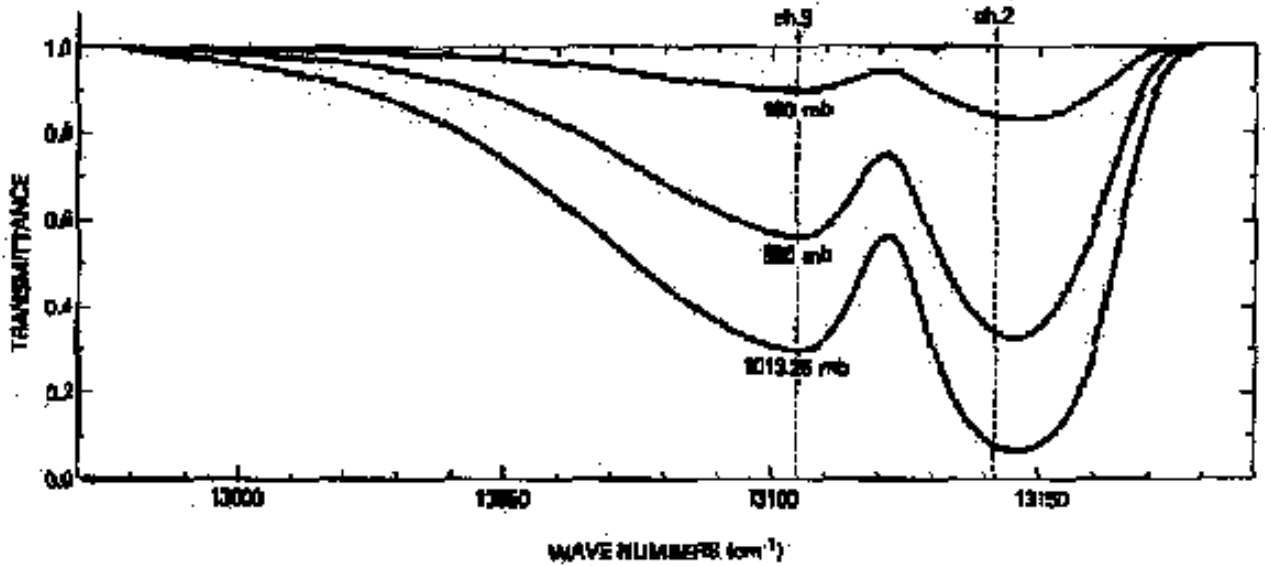**Fig. 17.** Oxygen absorption band transmittance for an air mass equal to 2 assuming a resolution of $6\,\mathrm{cm}^{-1}$ at 1013.25 mb (bottom curve).

As an example, consider the radiant energy absorbed by oxygen in the SeaWiFS band that extends from 745–785 nm. Assuming an air mass of 3, which would occur if the zenith angles of the sun and line-of-sight were 48°, and a surface pressure of 1,013 mb, Table 3 indicates a completely absorbing band 5.2 nm wide would absorb the same amount of radiant energy as the entire band. The percentage of energy removed from the band, E_{rem}, is

$$E_{\mathrm{rem}} = \frac{5.2}{785 - 745}100\% \tag{16}$$
$$= 13\%.$$

Since the limits of surface pressure for SeaWiFS observations range from about 985–1,035 mb, the absorption for air mass 3 would change only slightly by $(1\pm0.025)\,13\%$. If the SeaWiFS zenith angles of sun and line-of-sight increased from 0° to 60°, the equivalent bandwidth would increase from 4.6 to 5.8.

A precise computation of the oxygen absorption for a SeaWiFS band can be done easily with detailed line-by-line oxygen absorption spectra.

3.4 ABSORPTION CORRECTION

It is found that molecular oxygen has weak absorption bands in the red region of the solar spectrum. Comparing the equivalent oxygen transmittance bandwidth with the radiometer bandwidth, the oxygen optical thickness τ_{ox} at 750 nm can be estimated using concepts from Section 3.3. For a plane-parallel, homogeneous absorbing (oxygen at 750 nm) atmosphere, Beer's Law states the decrease in the radiant intensity is modeled by a simple exponential function:

$$I_1 = I_0 \exp\left[\frac{-\tau_{\mathrm{ox}}}{\mu_0}\right], \tag{17}$$

where I_0 is the incident radiant intensity, I_1 is the intensity after traversing through the absorbing medium, τ_{ox} is the oxygen optical thickness at 750 nm, and μ_0 is the cosine of the solar zenith angle.

Similarly, assuming a totally reflecting surface, the reflected radiant energy received by the satellite sensor, I_2 is

$$I_2 = I_1 \exp\left[\frac{-\tau_{\mathrm{ox}}}{\mu}\right], \tag{18}$$

where μ is the cosine of the satellite zenith angle. The absorptivity, defined as the fractional part of the incident radiation absorbed by the medium, is given by

$$A = \frac{I_0 - I_2}{I_0}, \tag{19}$$
$$= 1 - \exp\left[\frac{-\tau_{\mathrm{ox}}}{\mu_0 + \mu}\right].$$

The bandwidth of CZCS band 5, 750 nm, is 100 nm. Following the equivalent bandwidth concept developed in Section 3.3, the absorptivities for 2 and 3 air masses are

$$\frac{4.6}{100} = 1 - e^{-2\tau_{\mathrm{ox}}}, \tag{20}$$

and

$$\frac{5.2}{100} = 1 - e^{-3\tau_{\mathrm{ox}}}, \tag{21}$$

respectively. Solving (20) and (21) for τ_{ox} gives an average value of 0.02.

The CZCS atmospheric correction processing uses data from the first four bands to derive level-2 products. Band 5, 750 nm, is used for land and cloud screening only. The band 5 radiances were converted to percent albedo, α (Eckstein and Simpson 1991),

$$\alpha = \frac{L_t(750)}{t(\theta)t(\theta_0)F_0(750)}100\%, \tag{22}$$

19

$$t(\theta) \;=\; \exp\left[-\frac{0.5\tau_r + \tau_{\text{oz}} + \tau_{\text{ox}}}{\cos\theta}\right], \qquad (23)$$

where $F_0(750)$ is the incident solar irradiance at 750 nm, θ and θ_0 are satellite zenith and solar zenith angles, respectively, and $t(\theta)$ is the diffuse transmittance (1). All pixels with band 5 albedo values exceeding a given threshold are flagged as land or cloud pixels. Taking the oxygen absorption effect into account, the band 5 albedo value will increase and more pixels will be identified as land or cloud pixels. Results from CZCS Icelandic water scenes show

that the number of land or cloud pixels flagged increased 1.1% from 165,566 to 167,352.

3.5 CONCLUSIONS

From the analyses presented, the temporal and spatial variability of surface pressure is sufficiently great to require a pixel-by-pixel correction of SeaWiFS data if the chlorophyll accuracy goals of the mission are to be met. Also, the oxygen absorption correction is necessary for SeaWiFS as the 765 nm band straddles the oxygen absorption band and will be used for aerosol corrections.

C. McClain, J. Comiso, R. Fraser, J. Firestone, B. Schieber, E. Yeh, K. Arrigo, and C. Sullivan

Chapter 4

Pixel-by-Pixel Pressure and Ozone Correction Study for Ocean Color Imagery

Charles R. McClain
NASA Goddard Space Flight Center, Greenbelt, Maryland

Eueng-nan Yeh
General Sciences Corporation, Laurel, Maryland

Abstract

The global CZCS processing (Feldman et al. 1989) applied constant surface pressure and ozone values to all pixels of each two-minute scene. Sensitivity analyses are performed on CZCS imagery to estimate the impact of erroneous estimates of Rayleigh and ozone optical thicknesses on the derived pigment concentrations. It is concluded that the use of climatologies, i.e., standard atmospheric surface pressure, P_0, and fixed ozone values would seriously compromise the primary objective of the SeaWiFS mission, i.e., estimation of surface oceanic chlorophyll a and pigment concentrations to within $\pm 35\%$.

4.1 INTRODUCTION

The retrieval of accurate water-leaving radiances from satellite observations requires the computation of ozone absorption and Rayleigh scattering effects from two passes for both incoming and outgoing light. Previous algorithms for the processing of CZCS imagery such as those used in the global processing (Esaias et al. 1986; Feldman et al. 1989) made several assumptions about the atmosphere. One approximation was to use a standard atmospheric surface pressure, $P_0=1,013.25$ mb, to derive the Rayleigh optical thickness τ_{r0}. These constants (0.237, 0.123, 0.098, 0.044, and 0.0255 for 443, 520, 550, 670, and 750 nm, respectively) were applied to all pixels for all CZCS scenes regardless of the spatial and temporal variability in surface pressure. Each scene was also processed using a single ozone concentration value which was taken from the gridded observed data for the same day.

The ozone value used was the TOMS value located nearest to the center pixel in the scene. The $n(\lambda_i)$ exponents used (0.12, 0.00, and 0.00 for 443, 520, and 550 nm, respectively) were also assumed to be constant for scenes and are typical of marine haze aerosols. Note that these exponents are the negative of the n exponents defined in Gordon et al. (1983 and 1988). Results from the theoretical study made by André and Morel (1989) indicated errors due to natural variations in the surface pressure and total ozone are significant, i.e., at least 10% at low concentrations to more than 100% at concentrations above 8 mg m^{-3}.

This study extends the pressure and ozone variability analyses presented earlier (see Chapters 2 and 3) to include pixel-by-pixel corrections.

4.2 DATA PROCESSING

Three consecutive scenes in the vicinity of the Greenland and Norwegian Seas taken from orbit 9,235 on 22 August 1980 (or sequential day 235) were used for the comparison. The scenes include coastal and open ocean water masses providing a wide range of surface pigment concentrations (approximately 0.1–10 mg m^{-3}). Plate 7 illustrates the pigment products from these three (two-minute) CZCS scenes (identified on the left of the image) as derived using the standard global processing algorithms as implemented in SEAPAK (McClain et al. 1991a and 1991b). The center ozone values for scenes A, B, and C were 315, 369, and 361 DU, respectively.

4.2.1 Pixel-by-Pixel Pressure Corrections

The surface pressure fields used for this study were derived from Fleet Numerical Oceanography Center (FNOC) gridded data. The FNOC products used are available twice per day (0000 and 1200 GMT) and have a 2.5° resolution. The data were received from the GSFC Distributed Active Archive Center (DAAC), as described by Olsen and McClain (1992), in the NASA common data format (CDF). Because of the coarse spatial resolution and the fact that the observations are made at local noon, both temporal

and spatial interpolations are required. Section 4.3 describes the interpolation algorithms. The temporal interpolation was performed first, then the resultant pressures were spatially interpolated to the SEAPAK control point grid, a 26×26 point navigation array, where the Rayleigh radiance values are computed. The Rayleigh radiance values at pixels located between the control points are subsequently determined by linear interpolation of control point Rayleigh radiance values. Using interpolated Rayleigh radiance values is possible because the radiances are smoothly varying.

The control point surface pressure data for scenes A, B, and C are listed in Tables 4, 5, and 6, respectively. The pressure fields over these three scenes varied from 1,008 mb at the right-most edge of scenes A and B to 1,029 mb at the bottom left portion of scene A. The overall average of 1,020 mb is higher than the global CZCS processing value, 1,013.25 mb. The derived pigment image using the pixel-by-pixel pressure corrections is shown in Plate 8. In this analysis, a constant ozone value was used for each scene. Plate 9 is the difference between the pixel-by-pixel and the constant pressure analyses, i.e., Plate 8 minus Plate 7. Plate 9 shows the variations in surface pressure within a scene can result in a significant change of pigment concentrations.

4.2.2 Pixel-by-Pixel Ozone Corrections

The effect of applying a pixel-by-pixel ozone correction while assuming a constant pressure was also examined. The control point ozone values for scenes A, B, and C are listed in Tables 7, 8, and 9, respectively. The ozone distributions are quite different from scene to scene. The ozone range of scene A was 305–388 DU with values lower than the scene center value (315 DU) being located in the lower left quadrant of the scene. For scene B, which has an ozone range of 302–392 DU, values lower than the scene center value (369 DU) dominate the right half of the scene. For scene C, which has a range of 321–382 DU, the lower left quadrant is occupied by relatively high values (approximately 361 DU).

The pigment concentrations resulting from the pixel-by-pixel ozone corrections are shown in Plate 10. Plate 11 presents the pigment difference image computed by subtracting the constant ozone analysis from the pixel-by-pixel analysis (Plate 10 minus Plate 7). Effects of the variability of ozone values within a scene are clearly evident.

4.2.3 Pressure and Ozone Corrections

The pigment values obtained using the combination of pixel-by-pixel pressure and ozone corrections are shown in Plate 12. Pigment differences resulting from these corrections and the global CZCS processing corrections (Plate 12 minus Plate 7) are shown in Plate 13. Examination of the difference image indicates that at $11.14°$ W,$61.5°$ N (scene A, south of Iceland), for instance, the pigment value increased 39% from $1.66\,\mathrm{mg\,m^{-3}}$ (Plate 7) to $2.31\,\mathrm{mg\,m^{-3}}$ (Plate 12). In other locations, the pigment value decreased, e.g., 28% from $0.614\,\mathrm{mg\,m^{-3}}$ (Plate 7) to $0.441\,\mathrm{mg\,m^{-3}}$ (Plate 12) at $10.32°$ W,$70.35°$ N (scene B, east of Iceland). The pigment concentration frequency distributions corresponding to Plates 7 and 12 are shown in Fig. 18 and the frequency distribution of the pigment difference field in Plate 13 is shown in Fig. 19.

4.3 DATA INTERPOLATION

Values for a desired location and time rarely exist from observed or simulated data fields. Therefore, an interpolation algorithm can be used to estimate the quantities required from surrounding values. In the present case, both the pressure and ozone are available at predefined time and space intervals.

Assume there are N points surrounding a desired location, and time t is a desired time which is between two observation times, t_1 and t_2. The interpolation scheme uses an inverse distance and time weighting algorithm. For distance,

$$[V(t_1)] = \sum_{i=1}^{N} \omega_i V_i(t_1), \tag{24}$$

and

$$[V(t_2)] = \sum_{i=1}^{N} \omega_i V_i(t_2), \tag{25}$$

where

$$\omega_i = \frac{1}{d_i} \left[\sum_{j=1}^{N} \frac{1}{d_j} \right]^{-1}, \tag{26}$$

d is the distance from the observation point to the point of interest, i is the index of the surrounding point, and by definition $\sum \omega_i = 1$.

In the case of time,

$$\nu_1 = \frac{t_2 - t}{t_2 - t_1}, \tag{27}$$

$$\nu_2 = \frac{t - t_1}{t_2 - t_1}, \tag{28}$$

and

$$\langle [V(t)] \rangle = \nu_1 [V(t_1)] + \nu_2 [V(t_2)], \tag{29}$$

where the ν terms are the temporal weighting factors and $\nu_1 + \nu_2 = 1$. Substituting (24) and (25) into (29),

$$\langle [V(t)] \rangle = \sum \omega_i \big(\nu_1 V_i(t_1) + \nu_2 V_i(t_2) \big)$$
$$= [\langle V(t) \rangle]. \tag{30}$$

This equation states that the order in which the temporal and spatial interpolations are performed does not affect the result.

C. McClain, J. Comiso, R. Fraser, J. Firestone, B. Schieber, E. Yeh, K. Arrigo, and C. Sullivan

Table 4. Deviation of control point surface pressure values from 1,013.25 mb for scene A. Add 1,013.25 mb to the table value to compute the actual pressure.

10	10	10	11	12	12	13	13	13	13	13	13	12	12	12	12	12	11	11	11	9	8	6	4	1	-3
10	11	11	11	12	12	13	13	13	13	13	13	12	12	12	12	12	12	11	11	10	8	6	4	1	-3
10	11	11	11	12	12	13	13	13	13	13	13	12	12	12	12	12	11	11	10	8	7	4	1	-3	
10	11	12	12	12	13	13	13	13	13	13	13	13	12	12	12	12	12	11	10	8	7	5	1	-4	
11	11	12	12	12	13	13	13	13	13	13	13	13	12	12	12	12	12	12	11	9	8	5	1	-4	
11	11	12	12	12	13	13	13	13	13	13	13	13	12	12	12	12	12	12	11	9	6	5	2	-5	
12	11	12	13	12	13	13	13	13	13	13	13	13	13	13	12	13	12	11	11	9	6	6	2	-5	
12	12	12	13	13	13	13	13	13	13	13	13	13	13	13	13	13	13	12	11	9	6	6	2	-5	
12	13	12	13	13	13	13	13	13	13	13	13	13	13	13	13	13	13	12	12	10	7	6	3	-5	
13	13	13	13	13	13	13	13	13	13	13	13	13	13	13	13	13	13	12	12	10	7	4	3	-5	
13	13	14	13	13	13	13	13	13	13	13	13	13	13	13	14	14	13	12	10	8	4	3	-4		
13	13	14	14	14	13	13	13	13	13	13	13	13	13	13	14	14	13	13	11	8	5	3	-4		
13	14	14	14	14	14	14	13	14	13	13	13	13	14	14	14	14	14	13	13	11	8	5	2	-3	
13	14	14	14	14	14	14	14	14	14	14	13	13	13	14	14	14	14	14	13	11	11	8	5	1	-3
14	14	15	14	14	14	14	14	14	14	14	14	14	14	14	14	14	13	13	11	11	8	5	1	-3	
14	14	15	14	14	14	14	14	14	14	14	14	14	14	14	14	14	14	13	12	11	8	5	1	-4	
14	15	15	15	15	14	14	14	14	14	14	14	14	14	14	14	14	14	13	12	11	9	5	1	-4	
15	15	15	15	15	14	14	14	14	14	14	14	14	14	14	14	14	14	13	12	11	9	5	1	-3	
15	15	15	15	15	15	14	14	14	14	14	14	14	14	14	14	14	14	13	12	11	9	5	1	-3	
15	15	15	15	15	15	15	14	15	14	14	14	14	14	14	14	14	14	14	12	11	9	6	2	-3	
15	15	16	15	15	15	15	15	15	15	15	15	15	15	15	15	14	14	14	12	11	9	6	2	-3	
15	16	16	15	15	15	15	15	15	15	15	15	15	15	15	15	15	14	14	12	10	9	6	2	-3	
15	16	16	16	15	15	15	15	15	15	15	15	15	15	15	15	15	14	14	12	10	9	6	3	-2	
15	16	16	16	16	16	15	15	15	15	15	15	15	15	15	15	15	14	14	14	12	10	9	6	3	-2
15	16	16	16	16	16	16	16	16	15	16	16	15	15	15	15	15	14	14	13	12	10	10	6	3	-2
15	15	16	16	16	16	16	16	16	16	16	16	15	16	15	15	15	14	14	13	12	10	10	6	3	-2

Table 5. Deviation of control point surface pressure values from 1,013.25 mb for scene B. Add 1,013.25 mb to the table value to compute the actual pressure.

5	5	5	5	5	5	5	6	6	7	7	7	8	8	9	9	9	9	9	9	8	8	7	5	3	0
5	5	5	5	5	5	5	6	6	7	7	8	8	8	9	9	9	9	9	9	8	8	7	5	3	-1
5	5	5	5	5	6	6	6	7	7	8	8	8	8	9	9	9	9	9	9	8	8	6	5	3	-1
6	5	5	5	5	6	6	6	7	7	8	8	8	8	9	9	9	9	9	9	8	7	6	5	3	-1
6	5	5	5	6	6	7	7	7	7	8	8	9	9	9	10	10	9	9	9	8	7	6	5	3	-2
6	5	5	5	6	6	7	7	7	8	8	9	9	9	9	10	10	10	9	9	8	7	6	5	1	-2
6	6	6	6	6	6	7	8	8	8	8	9	9	9	9	10	10	10	9	9	8	7	6	5	0	-2
6	6	6	6	7	8	7	8	8	9	8	9	9	10	10	10	10	10	9	9	8	7	6	4	0	-2
6	6	6	7	7	8	8	8	8	9	9	9	10	10	10	10	10	10	9	9	8	7	6	4	0	-3
6	6	6	7	7	8	9	9	9	9	9	10	10	10	10	10	10	9	9	9	7	7	6	3	0	-3
6	6	7	7	8	8	9	9	10	9	10	10	10	10	10	10	10	10	9	9	7	6	6	3	0	-4
7	7	7	8	9	9	9	9	10	10	10	10	10	10	10	10	10	10	9	9	7	6	4	2	0	-4
7	7	7	8	9	10	10	10	10	10	10	11	11	11	11	10	10	10	10	9	7	6	4	2	0	-3
7	7	8	8	9	10	10	11	10	11	11	11	11	11	11	11	10	10	9	9	8	6	4	2	0	-3
7	8	8	9	9	11	11	11	11	11	11	11	11	11	11	11	10	10	9	9	8	6	4	2	0	-3
7	8	8	10	10	11	11	11	11	11	11	11	11	11	11	11	10	10	9	8	7	6	4	2	0	-3
8	8	8	10	10	11	11	11	12	11	12	11	12	11	11	11	10	10	9	9	7	6	5	2	0	-4
8	9	9	10	11	11	12	12	12	12	12	12	12	12	11	11	10	10	9	8	8	7	5	2	0	-4
8	9	9	10	11	11	12	12	12	12	12	12	12	12	11	11	11	10	10	9	8	7	5	3	0	-4
8	9	10	10	11	11	12	12	12	12	12	12	12	12	11	11	11	10	10	9	8	7	5	3	0	-5
8	9	10	11	11	12	12	12	12	12	12	12	12	12	12	11	11	10	10	9	9	7	5	3	0	-4
9	9	10	11	12	12	12	12	12	12	12	12	12	12	12	11	11	10	10	9	8	7	6	3	0	-4
9	9	10	11	12	12	12	12	12	12	12	12	12	12	12	12	11	10	10	9	8	8	6	3	0	-3
9	9	10	11	12	12	12	12	12	13	12	13	12	12	12	12	11	11	10	10	8	8	6	4	0	-3
10	10	10	11	12	12	13	12	13	13	13	13	12	12	12	12	11	11	10	9	8	6	4	1	-3	
10	10	10	11	12	12	13	13	13	13	13	13	12	12	12	12	12	11	11	11	9	8	6	4	1	-3

Table 6. Deviation of control point surface pressure values from 1,013.25 mb for scene C. Add 1,013.25 mb to the table value to compute the actual pressure.

13	12	11	11	10	10	10	10	11	11	11	11	11	11	11	10	10	9	8	7	7	6	5	5	5	5
12	12	11	10	10	9	9	10	10	10	10	11	11	10	10	10	10	9	8	7	7	5	5	5	5	4
12	12	11	10	9	9	9	10	10	10	10	10	10	10	10	9	9	9	8	7	7	6	5	5	5	4
12	11	11	10	9	9	9	9	9	9	10	10	10	10	10	9	9	8	8	7	6	6	5	5	5	4
12	11	10	10	9	8	8	9	9	9	9	10	9	10	10	9	9	8	8	7	6	6	5	5	5	4
12	11	10	9	9	8	8	8	9	9	9	9	9	9	9	9	9	8	8	7	6	6	5	5	5	4
11	11	10	9	8	8	8	8	8	8	9	9	9	9	9	9	9	8	8	7	7	6	5	5	5	4
11	10	10	8	8	7	8	7	8	8	8	9	9	9	9	9	8	8	8	7	7	6	6	5	5	4
10	10	8	8	8	7	7	7	7	8	8	8	8	8	9	8	8	8	8	7	7	6	6	5	5	4
10	10	8	7	7	7	7	7	7	8	8	8	8	8	8	8	8	8	8	7	7	6	6	5	5	4
9	9	8	7	7	7	7	7	7	7	8	8	8	8	8	8	8	8	8	7	7	7	6	6	5	3
9	8	8	7	6	7	6	6	7	7	7	8	8	8	8	8	8	8	8	7	7	7	6	6	5	3
9	8	7	7	6	6	6	6	6	7	7	7	8	8	8	8	8	8	8	8	7	7	6	6	5	3
9	8	7	6	6	6	6	6	6	6	7	7	8	8	8	8	8	8	8	8	8	7	6	6	5	3
8	8	7	6	5	5	5	6	6	6	7	7	7	8	8	8	8	8	8	8	8	7	7	6	5	3
8	7	7	6	5	5	5	5	6	6	6	7	7	8	8	8	8	8	8	8	8	7	7	6	5	3
7	7	6	6	5	5	5	5	6	6	7	7	7	8	8	8	8	8	8	8	8	7	7	6	5	2
7	6	6	5	5	5	5	5	6	6	6	7	7	8	8	8	9	9	9	8	8	8	7	6	4	2
7	6	5	5	5	5	5	5	5	6	6	7	7	8	8	8	9	9	9	9	8	8	7	6	4	2
6	6	5	5	5	5	5	5	5	6	6	7	7	8	8	8	9	9	9	9	8	8	7	6	4	1
6	5	5	5	5	5	5	5	5	6	6	7	8	8	8	8	9	9	9	9	8	8	7	6	4	1
6	5	5	5	4	5	5	5	5	6	6	7	7	8	8	9	9	9	9	9	9	8	7	5	4	1
6	5	5	4	4	5	5	5	6	6	6	7	7	8	8	9	9	9	9	9	9	8	7	5	4	0
5	5	5	5	4	5	5	5	6	6	6	7	7	8	8	9	9	9	9	9	9	8	7	5	4	0
5	5	5	5	5	5	5	5	6	7	7	7	8	8	8	9	9	9	9	9	8	8	7	5	3	0
5	5	5	5	5	5	5	6	6	7	7	7	8	8	9	9	9	9	9	9	8	8	7	5	3	0

Table 7. Deviation of control point ozone value from the value at the center of scene A. Add 315 DU to the table value to compute the actual ozone value.

73	65	60	53	47	46	40	37	32	30	24	21	24	28	33	36	42	36	32	38	42	40	30	14	2	-8
73	65	57	52	45	44	38	36	27	27	21	20	17	25	26	34	35	31	29	39	42	37	32	18	3	-7
73	64	54	51	44	42	37	34	26	22	20	18	14	14	16	32	32	30	31	37	42	39	34	20	4	-6
73	61	52	49	43	35	32	27	24	16	14	14	13	13	15	21	31	29	31	36	43	41	35	21	5	-8
69	58	51	41	42	33	30	23	22	15	13	9	12	10	14	18	24	25	31	35	43	40	35	21	4	-7
68	55	42	38	36	32	29	20	17	14	12	7	7	6	13	15	22	24	30	36	44	39	27	23	7	-4
55	50	41	37	34	25	25	19	16	10	10	6	6	5	6	14	21	23	30	39	44	40	24	23	9	-4
52	39	39	30	32	23	19	18	15	9	6	6	5	5	6	11	21	27	31	40	44	38	22	22	11	-4
49	35	36	28	24	21	14	11	9	8	6	3	4	4	5	11	16	25	31	39	44	37	21	21	11	-3
36	32	31	27	18	19	12	10	6	7	3	3	3	2	4	10	16	26	29	39	45	36	21	17	12	-1
33	31	25	25	16	11	11	9	4	3	2	2	1	1	1	10	16	25	29	38	46	35	21	16	12	-2
31	30	23	19	14	11	5	7	3	2	0	2	1	1	1	8	15	25	28	38	43	36	23	16	11	-1
28	23	22	19	12	4	4	4	2	1	-1	-1	1	1	5	9	14	22	29	38	43	36	24	16	9	-1
23	22	20	10	5	2	3	0	-2	-1	-2	-2	-2	-1	3	10	13	22	26	35	43	36	25	15	5	-1
17	21	14	8	4	-1	2	-1	-3	-5	-3	-3	-2	-1	2	11	19	22	31	35	42	36	26	16	4	-1
14	19	13	7	3	-2	-2	-2	-3	-6	-7	-5	-3	-2	2	6	15	22	29	35	40	37	30	17	4	-1
13	14	11	3	-1	-2	-2	-4	-5	-7	-7	-6	-6	-2	2	5	13	16	24	35	39	37	29	18	4	-2
12	11	9	2	-4	-3	-4	-5	-7	-7	-8	-7	-6	-3	2	3	11	15	25	31	39	37	30	17	4	-1
6	10	6	1	-5	-5	-4	-5	-6	-9	-8	-7	-6	-3	-3	-1	9	15	25	30	37	36	30	18	3	0
6	9	3	0	-5	-5	-5	-5	-8	-9	-9	-8	-7	-4	-3	-2	6	15	24	29	37	37	33	20	4	0
6	6	2	-1	-5	-5	-5	-6	-7	-9	-9	-9	-9	-5	-3	4	7	12	20	29	36	38	34	20	5	0
5	5	2	-1	-4	-5	-5	-6	-7	-9	-10	-9	-9	-6	-2	3	7	11	21	26	35	40	34	20	5	0
3	5	3	0	-4	-6	-6	-6	-8	-9	-10	-9	-9	-6	-4	2	8	12	21	24	35	42	35	20	5	-1
4	5	3	-1	-4	-5	-5	-6	-8	-9	-10	-9	-8	-6	-4	4	8	16	21	23	36	41	36	21	6	-1
4	6	3	0	-3	-4	-5	-6	-8	-9	-10	-10	-9	-6	-4	4	8	17	20	25	36	41	36	20	6	-2
4	6	3	0	-2	-4	-5	-6	-7	-9	-10	-10	-8	-7	-4	4	9	17	20	28	36	42	35	19	6	-3

Table 8. Deviation of control point ozone value from the value at the center of scene B. Add 369 DU to the table value to compute the actual ozone value.

```
 7 10  7   9 13 13  12  13  10   8   6   0  -2  -4  -5 -12 -13 -12 -13 -20 -24 -24 -21 -38 -43 -47
 9  9  9  11 15 16  12  14  13   9   7   3  -3  -3  -5  -9 -12 -11 -11 -19 -25 -27 -21 -36 -49 -55
10  9 10  17 16 18  13  15  14   9   6   3   0  -1  -4  -7  -7 -10  -8 -19 -27 -34 -20 -34 -47 -55
12  9 14  18 21 18  17  16  15  13   7   4   2   2  -4  -6  -6  -2  -4 -19 -28 -34 -29 -32 -48 -55
16 10 15  19 22 19  19  20  16  13  10   5   3   2  -1  -6  -6  -1  -5 -12 -30 -35 -32 -37 -52 -55
16 14 17  20 23 22  20  20  16  11  10   6   4   2   0  -3  -5   1  -6 -13 -31 -36 -36 -40 -53 -56
19 16 23  23 23 22  20  20  18  12  10   7   6   2   1  -3  -1   3  -5 -21 -28 -38 -41 -42 -54 -56
19 18 23  23 23 20  20  20  19  14  11   7   6   5   1  -2   1   6  -6 -20 -26 -38 -44 -44 -54 -57
19 18 20  22 21 20  19  17  20  13   9   7   5   5   3  -1   2   5  -5 -20 -31 -38 -41 -46 -54 -58
19 18 18  22 20 19  15  16  18  13   6   5   6   5   4   2   2   1  -6 -21 -29 -39 -37 -45 -54 -60
18 15 16  14 13 12  14  14  12  11   5   4   3   6   4   3   5   2  -9 -21 -31 -39 -32 -48 -54 -60
15  8 12  11 12 11   5  11   8   7   4   2   3   5   5   6   7   0 -12 -21 -31 -38 -37 -47 -54 -61
13  5  3   8  4  8   3   3   6   0  -3  -2   2   4   5   7   8  -1  -8 -22 -31 -38 -40 -49 -55 -62
12  4  2   5  1  0   1  -2   3  -3  -4  -7   1   3   4   6  11  -1 -19 -22 -31 -39 -41 -49 -56 -62
13  4  1  -3  0 -4  -1  -4  -4  -4  -6  -7  -3   2   3   5   8  -3 -18 -22 -32 -38 -42 -49 -56 -62
14  4  1  -2 -2 -4  -5  -5  -5  -9  -9  -8  -6  -3   1   4   0  -4 -17 -25 -32 -38 -42 -49 -56 -62
15  6  2  -1 -4 -5  -7  -6  -9 -10 -13  -9  -6  -4  -2   3  -1  -4 -17 -22 -33 -37 -41 -50 -56 -63
15  7  6   0 -4 -5  -7  -8 -10 -11 -14 -14  -8  -5  -3  -3  -5  -5 -16 -25 -29 -33 -41 -50 -56 -63
15  8  6   0 -3 -3  -7  -8 -11 -12 -15 -15 -13  -5  -4  -4  -7  -8 -15 -23 -27 -32 -39 -49 -55 -63
15 10  6   3 -2 -3  -7  -8 -12 -14 -15 -16 -14  -9  -4  -5  -8 -12 -14 -21 -25 -31 -38 -47 -53 -65
16 10  6   3 -2 -5  -6 -10 -12 -16 -19 -18 -14  -9  -9  -8  -9 -13 -14 -17 -22 -30 -38 -46 -53 -65
16 10  7  -1 -2 -4  -6 -11 -13 -18 -19 -22 -15 -11  -9  -9 -11 -14 -15 -17 -21 -24 -38 -45 -53 -64
17 10  6  -1 -2 -5  -7 -12 -15 -18 -20 -23 -21 -13  -9  -9 -10 -15 -15 -16 -19 -22 -32 -41 -53 -65
16  9  6  -1 -2 -6  -8 -13 -15 -22 -22 -24 -23 -21  -9  -9 -10 -16 -17 -16 -16 -20 -31 -41 -52 -67
17 10  6  -1 -6 -7 -12 -14 -21 -23 -26 -25 -26 -23 -18 -16  -9 -16 -19 -16 -13 -18 -30 -40 -52 -64
19 10  6  -1 -7 -8 -14 -17 -22 -24 -30 -32 -30 -26 -21 -18 -12 -17 -22 -16 -12 -15 -24 -40 -52 -63
```

Table 9. Deviation of control point ozone value from the value at the center of scene C. Add 361 DU to the table value to compute the actual ozone value.

```
-34 -26 -24 -20 -19 -16 -17 -17 -21 -20 -23 -22 -21 -20 -20 -19 -18 -15 -16 -12 -11 -11 -10 -13 -18 -27
-31 -22 -22 -19 -18 -14 -16 -17 -19 -19 -22 -18 -18 -19 -16 -16 -16 -14 -13 -12 -11 -10 -10 -13 -18 -28
-26 -21 -21 -18 -16 -14 -16 -16 -19 -19 -19 -18 -17 -17 -16 -15 -13 -13 -13 -11 -10 -10 -11 -13 -17 -27
-25 -19 -20 -17 -13 -13 -12 -14 -15 -18 -18 -18 -17 -16 -15 -14 -11 -13 -12 -11  -9 -11 -12 -13 -17 -27
-24 -19 -19 -14 -11 -12 -12 -13 -14 -17 -15 -15 -16 -13 -12 -12 -10 -10 -10 -10 -10 -11 -12 -14 -19 -27
-24 -19 -18 -11 -10 -11  -9 -13 -13 -14 -15 -14 -13 -12 -11  -9 -10 -10  -9 -10 -10 -12 -12 -14 -19 -27
-20 -19 -16  -9  -9  -8  -9  -9 -13 -12 -14 -13 -11 -12 -10  -8  -9  -9  -9  -9 -11 -11 -14 -15 -20 -27
-19 -16 -14  -8  -8  -5  -8  -9 -11 -11 -11 -12 -10  -9  -9  -7  -7  -8  -8  -9 -10 -12 -14 -18 -23 -27
-17 -10  -7  -6  -6  -5  -8  -8  -9 -11 -11 -10  -9  -9  -7  -7  -7  -7  -8  -8 -10 -12 -15 -18 -23 -29
-16  -9  -6  -3  -4  -4  -5  -8  -8 -11 -10  -8  -9  -8  -6  -7  -6  -6  -6  -8 -10 -13 -16 -19 -24 -29
 -9  -8  -5  -3  -2  -4  -5  -6  -7  -7 -10  -7  -6  -7  -5  -5  -5  -6  -6  -8 -10 -14 -16 -22 -24 -30
 -7  -3  -3  -1  -2  -2  -4  -4  -7  -7  -9  -7  -6  -5  -5  -5  -4  -6  -7  -8 -10 -14 -16 -23 -27 -30
 -5  -2  -1  -1  -1  -1  -3  -3  -6  -6  -5  -6  -5  -3  -5  -5  -5  -6  -7  -9 -10 -16 -21 -23 -27 -27
 -3  -3   1   2  -1  -1  -2  -2  -2  -5  -3  -1  -3  -3  -3  -4  -6  -7  -8  -9 -11 -17 -22 -25 -28 -24
  0  -2   2   2   1   0   0  -2  -1  -1  -2   0   0  -2  -3  -3  -6  -7 -10 -11 -12 -17 -24 -27 -28 -21
  0   0   3   3   2   0   1  -1   0   2  -1   1   1   1  -3  -5  -6  -8 -11 -12 -15 -18 -25 -26 -28 -23
  1   1   6   6   3   3   2   4   2   4   5   3   2   1  -2  -5  -6  -9 -11 -12 -16 -19 -25 -27 -27 -27
  1   2   7   8   4   5   3   4   6   5   6   8   3   1  -1  -5  -7  -9 -12 -13 -17 -19 -24 -28 -26 -33
  2   4   9   9   5   6   7   5   8   6   7   7   2   0  -1  -5  -7  -9 -12 -13 -17 -19 -24 -23 -16 -38
  3   6  10   9   9   7   9   6  10  12   9   7   5   0  -4  -5  -7 -11 -12 -13 -14 -19 -23 -17 -12 -40
  6  10  11  10  11  10  10  11  11  12  12   7   4   1  -4  -6  -7 -10 -12 -13 -14 -16 -23 -14  -5 -37
  7  12  14  13  12  14  11  14  14  13  12   7   4   2  -3  -6  -8 -10 -10 -13 -14 -14 -15  -8   4 -37
  8  13  14  15  13  16  14  15  17  14  12  10   4   2  -3  -4  -8 -10 -10 -13 -13 -12 -14 -10   8 -38
  9  14  15  15  15  17  18  16  17  16  12   8   6   0  -3  -4  -7 -10 -10 -12 -14  -9 -13 -12  -5 -39
 13  18  15  16  19  19  19  18  18  16  11   8   6   3  -3  -4  -6  -5  -9 -12 -14 -13 -13 -15 -21 -38
 15  18  15  17  21  21  20  21  18  16  14   8   6   4   3  -4  -5  -4  -5 -12 -16 -16 -13 -30 -35 -39
```
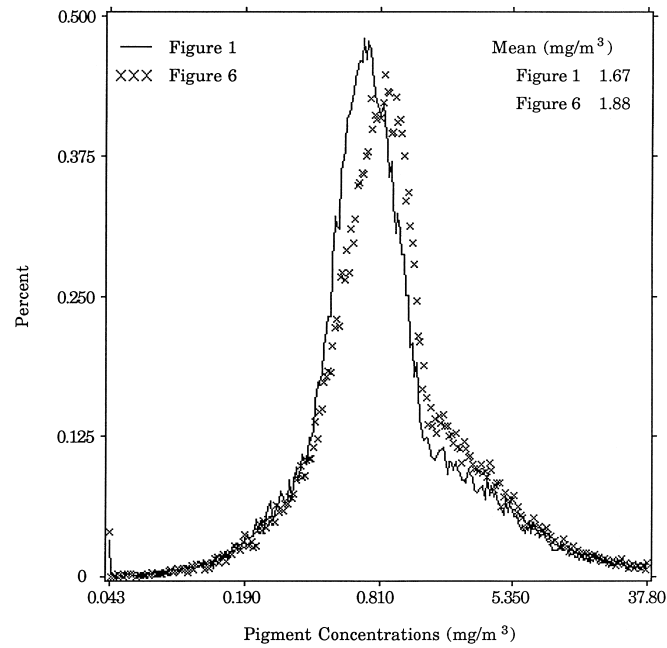
Fig. 18. Pigment concentration frequency distributions obtained from the global CZCS and the pixel-by-pixel ozone and pressure correction processing schemes shown in Plate 7 (solid line with a mean of $1.67\,\mathrm{mg\,m^{-3}}$) and Plate 12 ($\times$ with a mean of $1.88\,\mathrm{mg\,m^{-3}}$), respectively. The x-axis is logarithmic.
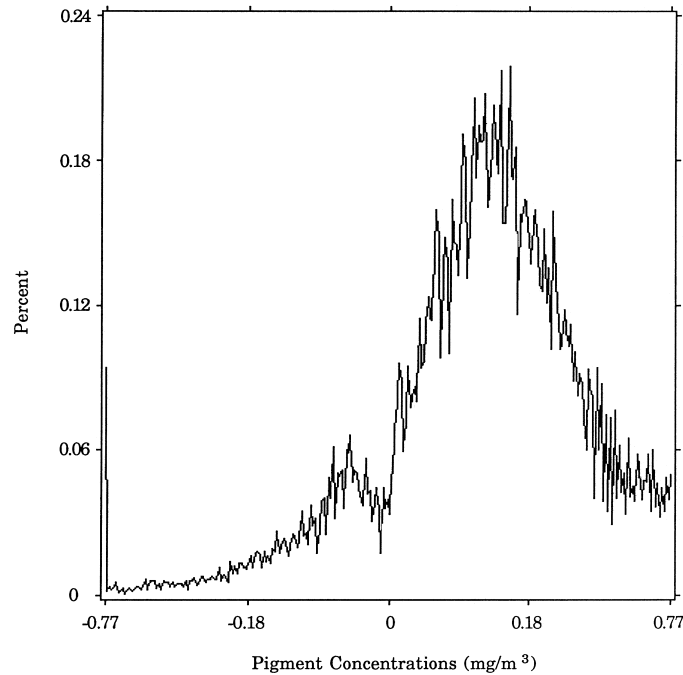
Fig. 19. The pigment difference frequency distribution for Plate 13. The x-axis has a logarithmic scaling.

4.4 CONCLUSIONS

From the analyses presented, the variability of surface pressure and total ozone is large enough to produce a relative deviation in concentration that can exceed the $\pm 35\%$ accuracy goal of SeaWiFS, leaving no margin for error from other sources. Climatologies and fixed ozone values are, therefore, inadequate, and it is necessary to have pixel-by-pixel corrections for these two effects using the highest resolution (both in time and space) products available.

C. McClain, J. Comiso, R. Fraser, J. Firestone, B. Schieber, E. Yeh, K. Arrigo, and C. Sullivan

Chapter 5

CZCS Overlapping Scenes Study

Charles R. McClain
NASA Goddard Space Flight Center, Greenbelt, Maryland

Eueng-nan Yeh
General Sciences Corporation, Laurel, Maryland

Abstract

Two coincident scenes from consecutive CZCS orbits are analyzed to investigate the consistency of the derived products under differing satellite and solar azimuth and zenith angles. General agreement for pigment retrievals to within the 35% SeaWiFS accuracy goal was found. Also, the Miami DSP CZCS edge mask algorithm was found to work very well and is described.

5.1 INTRODUCTION

At high latitudes, swath overlap will provide multiple views of cloud free subscenes from consecutive orbits allowing for greater numbers of samples in the level-3 bins for a given data day. In these situations, the products will be derived under widely varying solar and spacecraft azimuth and zenith angles. The present study is designed to examine the consistency of the derived products using the current CZCS atmospheric correction algorithm (Gordon et al. 1988).

5.2 DATA ANALYSIS

Two CZCS scenes with large cloud free subscenes covering the Denmark Strait area were used. Within both swaths, two clear subscenes were identified. The two orbits are 9,193 (19 August 1980, sequential day 232, 11:05:53.6–11:07:53.3) and 9,194 (12:49:23.6–12:51:23.6). The first subscene was centered at $17.1°$ W,$71.0°$ N near Scoresbysund, Greenland, and the second subscene is centered at $35.3°$ W, $65.6°$ N near Kap Dan, Greenland. From Plate 14, the first subscene is near nadir in the 9,193 swath and on the right limb of the 9,194 swath. The second subscene is on the left limb of the 9,193 swath and near nadir of the 9,194 swath. Thus, comparisons of data from both limbs of the scan can be compared to retrievals near nadir. In order to process the scenes using SEAPAK (McClain et al. 1991a and 1991b) the original images were subsampled using subsampling factors of 3 and 2 for pixel and line directions, respectively, to form 512×512 image files.

The two scenes were processed using the atmospheric correction and bio-optical algorithms of Gordon et al. (1983 and 1988) and the calibration of Evans and Gordon (1993)

used in the global CZCS processing. The $n(\lambda_i)$ exponents used (0.12, 0.00, and 0.00 for 443, 520, and 550 nm, respectively) were those that were applied to all scenes processed during the global CZCS processing. Note that these exponents are the negative of the n exponents defined in Gordon et al. (1983 and 1988). Ozone values derived from the scene center location were applied to all pixels within a scene. The ozone values used for orbits 9,193 and 9,194 were 350 and 368 DU, respectively. This difference would not produce significant differences in the pigment retrievals.

In the pigment products shown in Plate 14, a sensor ringing mask has been applied using the method developed by R. Evans for the CZCS global processing. Also, the right-most 41 pixels of each scan line of orbit 9,194 (hatched area of Plate 14, upper right panel) were also excluded from further analysis as this area failed the edge mask flag, also developed by R. Evans for the global CZCS processing (see Section 5.3). The pigment images were remapped to a common universal transverse mercator (UTM) projection so pixel-to-pixel comparisons between two orbits could be made. Finally, the lower two panels of Plate 14 show the remapped images with the ringing and edge masks applied.

Fig. 20 shows the chlorophyll scatterplot (top) and the frequency distributions of log[pigment] (bottom) for the two scenes. Data values used for Fig. 20 are from only unmasked portions of the common areas of the two scenes. The bimodal chlorophyll distributions are a result of the switching mechanism in the bio-optical algorithm (Muller-Karger et al. 1990).

In the standard CZCS atmospheric correction method, the total radiance received by the CZCS is described by (1). Nine-pixel average values of terms in (1) and the derived

$$(r^2 = 0.13)$$
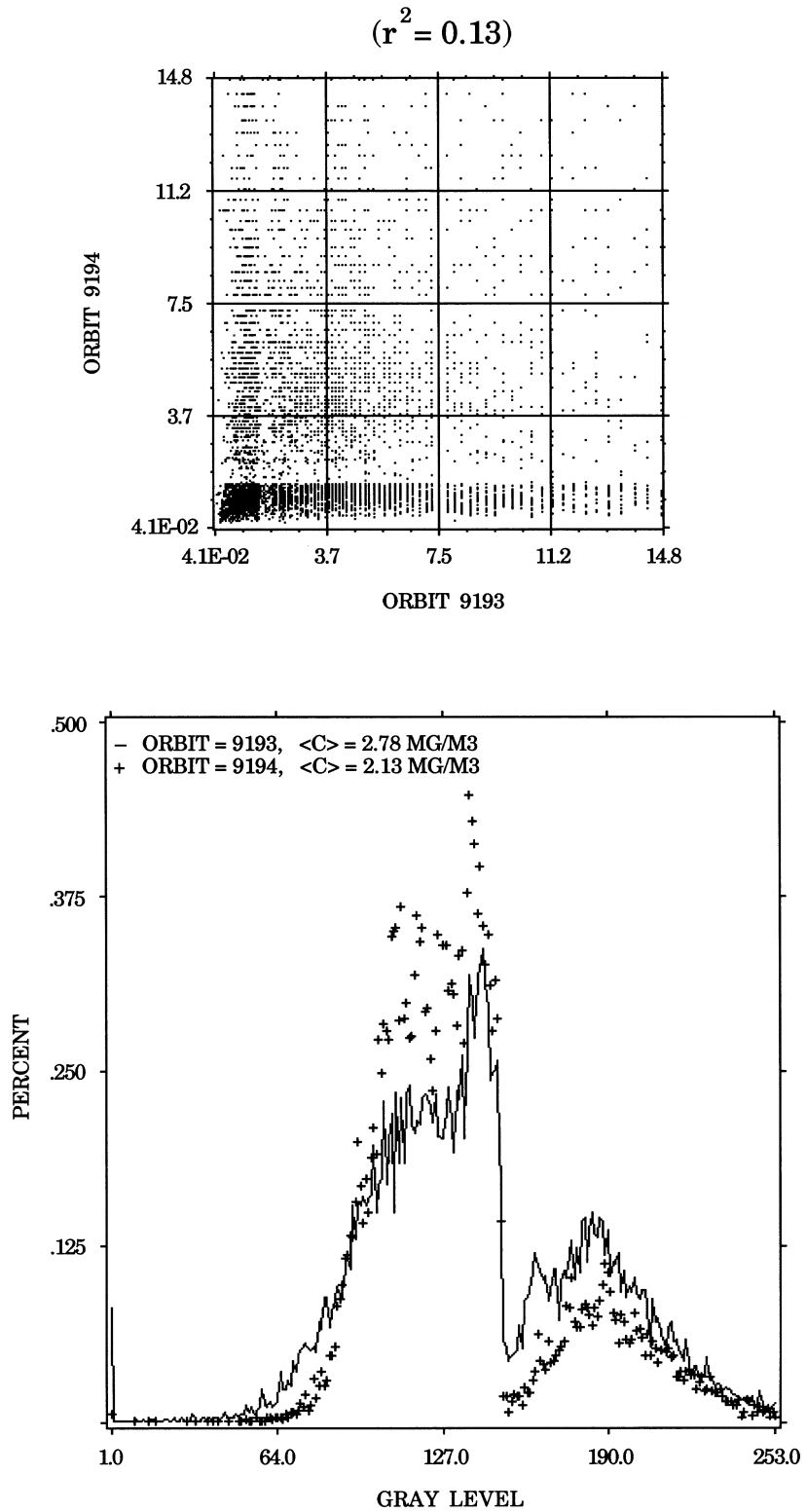
Fig. 20. Chlorophyll scatterplot (top) and frequency distributions of log[pigment] (bottom) for unmasked common pixels of the two pigment scenes. For the latter, orbit 9,193 (solid line) has a mean pigment concentration of 2.78 mg m^{-3} and orbit 9,194 (+) has a mean pigment concentration of 2.13 mg m^{-3}.

pigment concentrations are listed in Table 10. A summary of the spacecraft and solar azimuth and zenith angles is provided in Table 11.

Table 10. Nine-pixel average values of the terms in (1) and pigment concentration.

Parameter		Value			
Orbit		9,193	9,194	9,193	9,194
Latitude [° N]		71.0	71.0	65.6	65.7
Longitude [° W]		17.1	17.1	35.3	35.3
Term	Band	Average Values			
$\langle L_t \rangle$	1	4.875	6.192	6.727	5.448
	2	2.691	3.432	3.725	2.967
	3	2.102	2.682	2.888	2.319
	4	0.854	1.113	1.232	0.928
$\langle L_r \rangle$	1	4.605	5.732	6.313	4.945
	2	2.418	2.967	3.339	2.556
	3	1.854	2.251	2.543	1.956
	4	0.731	0.888	1.019	0.761
$\langle L_a \rangle$	1	0.149	0.274	0.260	0.201
	2	0.149	0.273	0.258	0.202
	3	0.142	0.258	0.243	0.193
	4	0.123	0.225	0.213	0.167
$\langle L_W \rangle$	1	0.137	0.226	0.189	0.344
	2	0.135	0.218	0.146	0.227
	3	0.115	0.198	0.116	0.185
	4	0.000	0.000	0.000	0.000
$\langle t \rangle$	1	0.878	0.822	0.821	0.878
	2	0.919	0.880	0.880	0.918
	3	0.917	0.875	0.876	0.915
	4	0.962	0.942	0.942	0.961
$\langle$Chl.$\rangle$		0.895	0.940	0.519	0.397

Table 11. Solar and spacecraft azimuth and zenith angles and scan pixel numbers (a full swath has 1,968 pixels) for the analysis areas of Table 10.

Parameter	Value			
Orbit	9,193	9,194	9,193	9,194
Latitude [° N]	71.0	71.0	65.6	65.7
Longitude [° W]	17.1	17.1	35.3	35.3
Pixel Number	976	1,818	114	966
Angle	Angular Values [°]			
Solar Zenith	61.50	58.56	62.63	55.60
Satellite Zenith	23.17	52.32	52.75	23.23
Solar Azimuth	125.15	96.16	146.58	118.46
Satellite Azimuth	297.72	207.74	19.43	287.84

5.3 MIAMI EDGE MASK

In certain situations, the CZCS derived products are questionable along the edges of a scan line. R. Evans evaluated the circumstances where pigment retrievals in particular are unreasonably high. He found that the poor retrievals were a function of tilt angle and developed an algorithm to compute a mask for identifying the affected area within a scene. Separate algorithms are used for the left and right limbs of the scan.

The EDGEMASK program generates a mask for both sides of the scan. For the left limb, a positive integer defines the ending pixel number of the left limb mask (the starting pixel is always pixel number one) and must be supplied by the user. A zero value for the left limb mask indicates no mask is applied. Similarly, a positive value can define the starting pixel of the right limb. However, when a zero value is input for the right limb mask starting pixel, an automated algorithm will be used which is based on the tilt angle, α. Each CZCS scan line contains 1,968 pixels, but the global CZCS processing subsampled the data by a factor of four resulting in only 492 pixels. The program computes the right edge starting pixel (the ending pixel is 492) as follows:

$$
\begin{cases}
492, & \text{if } \alpha < 14°; \\
492 - \left[3.75(\alpha - 14°)\right] & \text{if } 14° < \alpha < 18°; \\
492 - \left[7.5(\alpha - 18°) + 15\right], & \text{if } 18° < \alpha < 20°; \\
462, & \text{if } 20° < \alpha.
\end{cases}
\tag{31}
$$

Note, no mask is required for negative tilts. The tilt angles for the 9,193 and 9,194 scenes were both $+20°$.

5.4 CONCLUSIONS

Despite large differences in the atmospheric path length of the subscenes compared, the pigment products were reasonably similar, thus, the atmospheric correction algorithms are sufficiently accurate to allow the accumulation of data into level-3 bins from different orbits. This result indicates no selection criterion is necessary for determining the *best* orbit for a particular level-3 bin. Also, the Miami edge mask algorithm accurately determined the width of the area of questionably high pigment values on the right limb of the 9,194 scene.

Chapter 6

A Comparison of CZCS and *In Situ* Pigment Concentrations in the Southern Ocean

Kevin R. Arrigo
Oak Ridge Institute for Science and Education, Oak Ridge, Tennessee

Charles R. McClain
NASA Goddard Space Flight Center, Greenbelt, Maryland

James K. Firestone
General Sciences Corporation, Laurel, Maryland

Cornelius W. Sullivan
University of Southern California, Los Angeles, California

Josefino C. Comiso
NASA Goddard Space Flight Center, Greenbelt, Maryland

Abstract

The large-scale distribution of pigments in the Southern Ocean, as viewed from the CZCS, shows extensive blooms and enhanced pigments which are distributed asymmetrically about the Antarctic continent. Comparative analysis with an extensive database of historical *in situ* data reveals that the magnitude of these enhanced pigments may actually be 1.8 times higher than previously reported. Pigment concentrations computed using a new Southern Ocean CZCS algorithm adjusted to reflect regional differences in bio-optical properties of the water column agree to within 5% of estimates made using an extensive database of *in situ* pigment data. This result is encouraging and indicates that the unique features of the large-scale data, including the asymmetrical distribution around the continent, are real.

6.1 INTRODUCTION

Knowledge of global-scale features of phytoplankton biomass and productivity is crucial to obtaining a more complete understanding of the role of the Southern Ocean in the contemporary global carbon cycle of matter (Fasham et al. 1990) and the relationship between the distributions of primary producers and higher trophic level consumers at the basin scale. As the major agents in the sea responsible for the transformation of approximately 50×10^{15} grams of carbon dioxide into fixed organic carbon (in the form of phytoplankton biomass), phytoplankton are central to studying and understanding both problems. These single celled plants represent a major potential sink for atmospheric carbon dioxide in the sea (Platt and Sathyendranath 1988) as well as the major food of planktonic grazers (Frost 1991).

Accurate assessments of the large-scale distribution, abundance, productivity, and sedimentation rates of phytoplankton are difficult to obtain by conventional ship-based studies with their characteristic low spatial resolution. This is especially true for the Southern Ocean where severe weather and seasonal coverage by sea ice greatly restricts access by ships (Sullivan et al. 1988, Comiso et al. 1990, and Comiso et al. 1993). However, CZCS pigment data has been shown to be useful for characterizing surface features of the Southern Ocean (McClain et al. 1991c and Comiso et al. 1993).

Satellite data are a very important source of large-scale pigment distributions and standing crops at high latitudes, but adequate validation is necessary because of the uncertainties associated with low sun angle, multiple scattering effects, and unknown bio-optical characteristics of surface waters. Previous quantitative comparisons of *in situ* pigments (chlorophyll *a* plus phaeopigment) with CZCS data have been encouraging. Unfortunately, these studies either focused on the Northern Hemisphere (Balch et al. 1992) or utilized small Southern Ocean data sets which were spatially restricted (Sullivan et al. 1988, Comiso et al. 1990, and Comiso et al. 1993).

This study is concerned with comparing mean summer *in situ* pigment values south of 30° S latitude with CZCS

climatologies averaged over identical temporal and spatial scales. The objective of the study is to assess the applicability of existing pigment algorithms to Southern Ocean waters.

6.2 CZCS METHODS

An austral summer Southern Ocean (south of $30°$ S) CZCS image was created by averaging monthly (October-March) pigment climatologies from 1978 to 1986. All images were processed using the standard NASA global processing (GP) algorithm (Gordon et al. 1983) in conjunction with the SEAPAK image processing package (McClain et al. 1991a and 1991b). Pigment concentrations in excess of $10\,\mathrm{mg\,m^{-3}}$ (less than 1% of all samples) were excluded from further analyses due to suspected unreliability. Output of a regional Southern Ocean (SO) algorithm (Mitchell and Holm-Hansen 1991) was also approximated by applying the appropriate conversion factor to specific pigment intervals from the GP algorithm.

The basic equations for both the GP and the SO algorithms are:

$$\log[C + P] \;=\; a + b \log\left[\frac{L_u(441)}{L_u(550)}\right], \text{ for } C < 1.5 \quad (32)$$

$$\log[C + P] \;=\; a + b \log\left[\frac{L_u(520)}{L_u(550)}\right], \text{ for } C > 1.5 \quad (33)$$

where $[C+P]$ is mg chlorophyll a plus phaeopigments $\mathrm{m^{-3}}$ (the former being C and the latter P), and the coefficients a and b differ for the GP and SO algorithms as shown in Table 12. Note that there is no statistical difference between the GP and the SO $L_u(520)/L_u(550)$ algorithms.

Table 12. Coefficients for the GP and SO CZCS pigment algorithms. The coefficients for the GP algorithm are from Gordon et al. (1983) and the coefficients for the SO algorithm are from Mitchell and Holm-Hansen (1991).

CZCS Band Ratio and Algorithm Coefficients		Algorithm	
		GP	SO
$L_u(441)/L_u(550)$	a	0.14	0.53
	b	-1.55	-1.63
$L_u(520)/L_u(550)$	a	0.63	0.48
	b	-4.72	-3.32

Pigment concentrations were averaged for each image a) over the entire region south of $30°$ S, and b) for each $1°$ of latitude between $30°$ S and $65°$ S using the program GRDMEAN from the SEAPAK image processing package (McClain et al. 1991a and 1991b). The factors used to convert GP algorithm output to SO algorithm output are given in Table 13. The conversion process requires the GP value be multiplied by the listed factor.

Table 13. $L_u(440)/L_u(560)$ as seen by the CZCS, pigment concentrations are in mg chlorophyll a plus phaeopigments $\mathrm{m^{-3}}$, $[C + P]$, of the GP and SO algorithms (see Table 12), and the factor used to convert GP pigment to SO pigment.

$L_u(440)/L_u(560)$	SO	GP	Factor
1.00	3.388	1.380	2.455
1.25	2.355	0.977	2.411
1.50	1.750	0.736	2.376
1.75	1.361	0.580	2.347
2.00	1.095	0.471	2.322
2.25	0.904	0.393	2.301
2.50	0.761	0.334	2.281
2.75	0.651	0.288	2.264
3.00	0.565	0.251	2.248
3.25	0.496	0.222	2.234
3.50	0.440	0.198	2.221
3.75	0.393	0.178	2.208
4.00	0.354	0.161	2.197
4.25	0.320	0.147	2.186
4.50	0.292	0.134	2.176
4.75	0.267	0.123	2.167
5.00	0.246	0.114	2.158
5.25	0.227	0.106	2.150
5.50	0.210	0.098	2.142
5.75	0.196	0.092	2.134
6.00	0.183	0.086	2.127
6.25	0.171	0.081	2.120
6.50	0.160	0.076	2.113
6.75	0.151	0.072	2.107
7.00	0.142	0.068	2.101

6.3 *IN SITU* METHODS

Surface (less than $10\,\mathrm{m}$ depth) *in situ* pigment (chlorophyll a plus phaeopigments) data for the Southern Ocean (6,183 samples) were extracted from a pigment database compiled at GSFC. This *in situ* database is the most comprehensive set of surface pigment that has thus far been assembled for the Southern Ocean. The locations of the data stations are shown in Fig. 21. Data were transferred to a spreadsheet program and sorted by latitude. Chlorophyll a concentrations were averaged 1) over the entire region south of $30°$ S, and 2) for each $1°$ of latitude between $30°$ S and $65°$ S. Because many stations did not include concurrent phaeopigment concentrations, a chlorophyll a to phaeopigment ratio (C/P) of 2.57 ± 1.51 ($N=1{,}070$) were applied to each computed mean to approximate total pigment concentrations. To maintain consistency with CZCS data screening procedures, all *in situ* pigment concentrations in excess of $10\,\mathrm{mg\,m^{-3}}$ (10 out of 6,183 samples) were excluded from further analyses.

Relative frequency distributions for CZCS (as estimated by both the GP and the SO algorithms) and *in situ* pigments were determined using the program HIST in the SEAPAK image processing package (McClain et al. 1991a
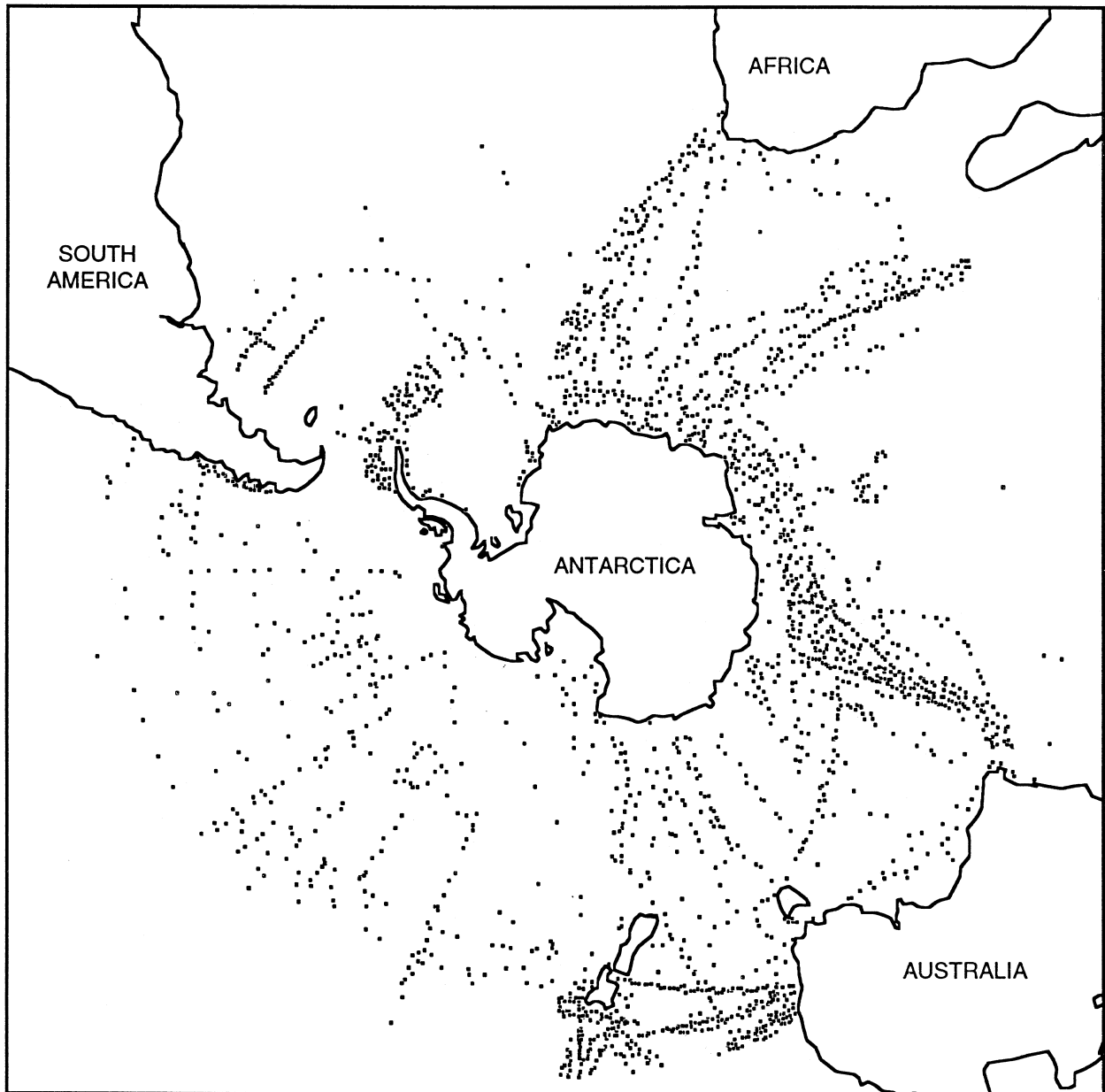
Fig. 21. Stations where *in situ* pigment samples were collected.

C. McClain, J. Comiso, R. Fraser, J. Firestone, B. Schieber, E. Yeh, K. Arrigo, and C. Sullivan
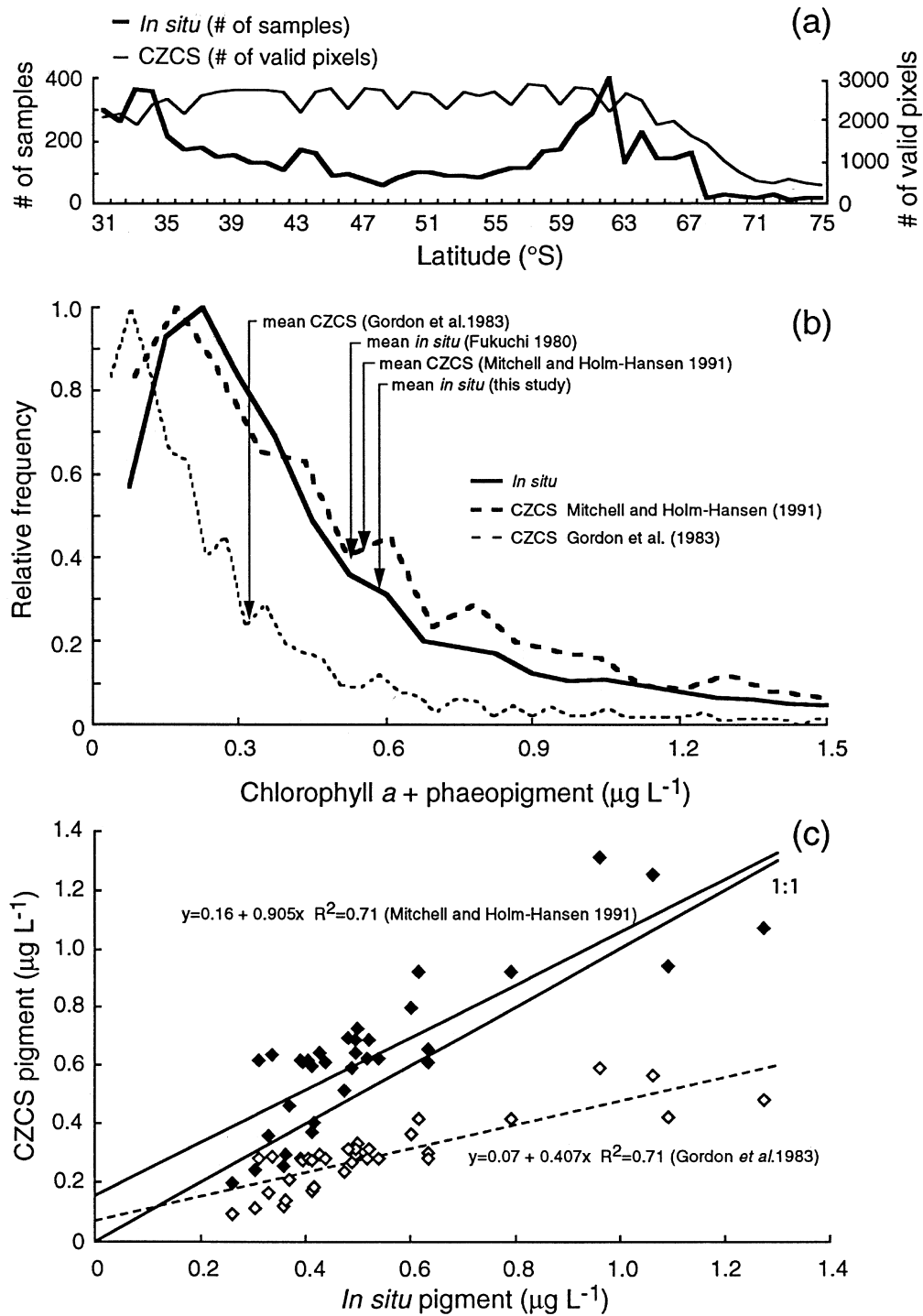
Fig. 22. a) The total number of data points for CZCS and *in situ* pigments for each 1° of latitude between 30°S and 65°S. **b)** Relative frequency distribution of chlorophyll *a* plus phaeopigment for the *in situ* data set (*N*=6,173) and for the CZCS data processed using the SO (Mitchell and Holm-Hansen 1991) algorithm and the GP (Gordon et al. 1983) algorithm. Mean *in situ* and CZCS values are also shown. **c)** CZCS pigment (chlorophyll *a* plus phaeopigments) concentration, estimated using the GP and the SO algorithms, versus *in situ* pigment concentration. *In situ* and CZCS pigment data points were calculated as circumglobal means for each 1° of latitude between 30°S and 65°S. The line labeled 1:1 is the line of perfect agreement between the CZCS and *in situ* data.

and 1991b). *In situ* pigments were regressed against CZCS pigment concentrations as estimated by both the GP and the SO algorithms. The region south of $65°$ S was excluded from this analysis due to a scarcity of both CZCS and *in situ* pigment data (Fig. 22a).

6.4 RESULTS AND DISCUSSION

South of $30°$ S, *in situ* pigment concentrations averaged $0.58\,[C+P]$ (N=6,173). A similar study (Fukuchi 1980) reported a mean *in situ* pigment concentration for waters between $35°$ S and $63°$ S of $0.38\,\mathrm{mg\ m^{-3}}$ for chlorophyll *a* alone, or correcting for the presence of phaeopigments (C/P=2.57±1.51 in the Southern Ocean, N=1,070), $0.53\,[C+P]$, within 10% of this study's *in situ* estimate. The mean CZCS pigment concentration computed using the GP algorithm currently in wide use (Gordon et al. 1983) was $0.32\,[C+P]$, suggesting CZCS pigment concentrations previously reported for the Southern Ocean are underestimated by approximately 45%. This is a remarkable result because it was previously suspected by some that high pigment values in the polar regions may be associated with retrieval errors due to low solar angles and multiple scattering effects.

The large discrepancy may be attributed to uncharacteristically low pigment-specific absorption and low detrital concentrations of Southern Ocean waters (Mitchell and Holm-Hansen 1991). A recently developed SO pigment algorithm (Mitchell and Holm-Hansen 1991), which reflects these water characteristics, in fact shows considerable improvement. The SO algorithm, which utilizes water leaving radiances (L_u) at 441 and 560 nm yields pigment concentrations that are 2.1–2.5 times greater (Table 13) than the GP algorithm for $L_u(441)/L_u(560)$ ratios greater than 1, i.e., GP $[C+P]$ less than 1.5. The mean summertime pigment concentration computed using the SO algorithm is $0.55\,[C+P]$, within 5% and 4%, respectively, of the *in situ* means reported here and by Japanese investigators (Fukuchi 1980).

The relative frequency distribution of chlorophyll *a* plus phaeopigments (Fig. 22b) for this study's *in situ* data set also exhibits substantially better agreement with satellite observations when the CZCS data are adjusted to fit the SO algorithm than when it is processed using the GP algorithm. The log-normal pigment distribution and the presence of some high pigment values (the data set includes 162 samples, or 2.6%, with $[C+P]$ greater than 2 results in *in situ* and CZCS derived mean pigment concentrations that are substantially higher than mode concentrations. Fukuchi (1980) reported a similar percentage of *in situ* pigment concentrations (2%) greater than $2\,\mathrm{mg\ m^{-3}}$. These high pigments were found in the southern-most waters south of $63°$ S, generally consistent with our observations from CZCS.

To further compare the applicability of the new SO algorithm and the earlier GP algorithm to Southern Ocean waters, summer CZCS pigment concentrations derived using each algorithm were regressed against similarly computed mean *in situ* pigment concentrations (Fig. 22c). Both the SO and GP algorithms were able to explain 71% of the variability in the data (the regression coefficients are the same because the analyses were performed on the same data set). This is encouraging and indicates ocean color information obtained from satellites is useful for characterizing pigment concentrations at high latitudes. Moreover, the best fit slope of 0.91 obtained with the SO algorithm indicates it was a better approximation of the *in situ* pigment data, than was the standard GP algorithm (0.41 slope), which was developed from a limited number (49) of bio-optical stations in waters around the US. The results presented here emphasize the need to develop regional algorithms in the processing of ocean color data, particularly because the next ocean color mission, SeaWiFS, is scheduled for launch in 1994.

C. McClain, J. Comiso, R. Fraser, J. Firestone, B. Schieber, E. Yeh, K. Arrigo, and C. Sullivan

Chapter 7

The Generation of Ancillary Data Climatologies

James K. Firestone
Brian D. Schieber
General Sciences Corporation, Laurel, Maryland

ABSTRACT

The SeaWiFS Data Processing System (SDPS) requires climatologies, in the form of monthly averages computed on a global basis of total ozone, wind speed, atmospheric pressure, and relative humidity at the ocean surface. These data are used during the generation of performance assessment, or *quick-look*, products within the level-2 processing stream. The calibration and validation element has computed the climatologies, and placed the results in a separate file in the NCSA HDF for each of the ancillary parameters. This chapter describes the method used for the generation of the climatologies.

7.1 INTRODUCTION

The processing of SeaWiFS data from level-1 (calibrated radiances) to level-2 (derived products) requires four ancillary fields: total ozone, surface values of wind speed, atmospheric pressure, and relative humidity, all of which are incorporated in the atmospheric correction algorithm (H. Gordon, personal communication). The SeaWiFS refined products are generated with a 3-week delay, using ancillary fields subjected to quality control (QC) procedures and originally collected in near-real time. However, the performance assessment product, since it is generated within 24 hours of data collection to provide a quick look at the ocean color field, will not have the benefit of QC ancillary data and will, therefore, use climatological fields (Fig. 23).

The basic requirements for the data sets used in generating the climatologies are that they be available globally, at the finest spatial resolution possible, for the longest time period possible, and ideally, that related parameters (such as the meteorological fields) be found from the same data source. This last requirement, if met, would eliminate the need for creating a hybrid output where intercomparisons between parameters would be made more difficult.

7.2 METEOROLOGICAL DATA SETS

In order to choose an appropriate data source for the meteorological climatologies, the data archive of the Ocean Color Group in the Laboratory for Hydrospheric Processes at GSFC was searched. This data archive consists of a large group of files in the NASA CDF format (NSSDC 1991), representing various types of model outputs, climatologies and field experiment results (Firestone et al.

1990). Most of the CDF files were originally generated by the staff of the NASA Climate Data System (NCDS), now the GSFC DAAC (Olsen and McClain 1992). Only one data source in the archive, the Comprehensive Ocean-Atmosphere Data Set (COADS), contained gridded pressure, humidity, and wind data (Woodruff et al. 1987 and Slutz et al. 1985). In addition, COADS data were available as monthly means spanning a 45-year period, 1946–1990, providing a relatively long time period for the averaging. To check whether trends existed in the data collected over this period, time series plots were generated at a Northern and a Southern Hemisphere site. These results are summarized in Section 9.3.

COADS is a cooperative effort involving several agencies or organizations, including the National Oceanic and Atmospheric Administration's (NOAA) National Climatic Data Center (NCDC), NOAA's Environmental Research Laboratories (ERL), the Cooperative Institute for Research in Environmental Sciences (CIRES), and the National Center for Atmospheric Research (NCAR). The effort seeks to provide a historical record of 70 million surface marine data reports starting in 1854. The COADS data in the NASA ocean color archive have been quality controlled and are organized in decadal groupings of related parameters (*trimmed groups*). Each decade's gridded product (at global 2° latitude by 2° longitude resolution, or 90 latitude by 180 longitude points) is derived by binning edited marine observations, such as those available from ships of opportunity, and providing averages for each month within the decade (NSSDC Master Directory 1993). As shown in Table 14, two COADS trimmed groups from each decade, beginning with the 1940s, were needed to compute the climatology for each meteorological parameter.
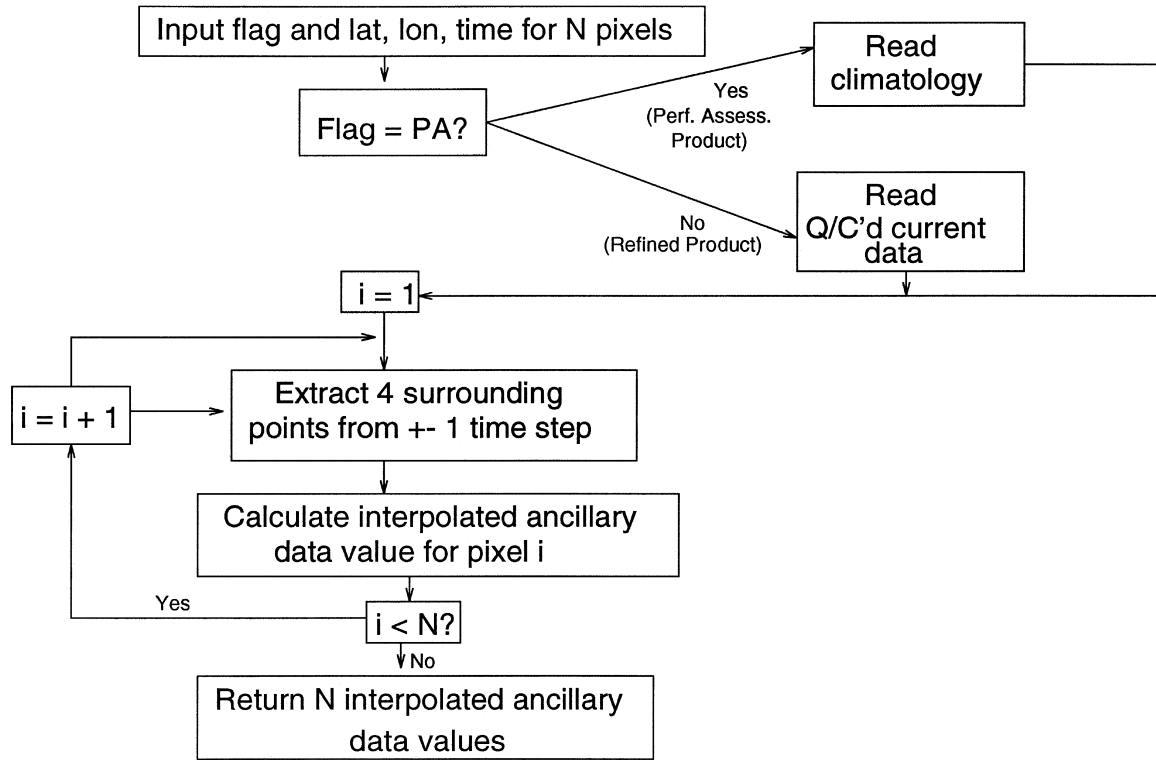
Fig. 23. Schematic for the retrieval of ancillary data used in the SDPS for the generation of level-2 products. Note the use of climatological ancillary fields for the generation of the performance assessment product.

Table 14. CDF file names and surface meteorological parameters used in climatology creation.

File Name	Parameters	Temporal Coverage
4601-4912_COADS_MSTG_GROUP3	Relative Humidity	January 1946 → December 1949
5001-5912_COADS_MSTG_GROUP3	Relative Humidity	January 1950 → December 1959
6001-6912_COADS_MSTG_GROUP3	Relative Humidity	January 1960 → December 1969
7001-7912_COADS_MSTG_GROUP3	Relative Humidity	January 1970 → December 1979
COADS_MSTG2_GROUP3_8001-8912	Relative Humidity	January 1980 → December 1989
COADS_G3_90	Relative Humidity	January 1990 → December 1990
4601-4912_COADS_MSTG_GROUP4	Wind Speed and Pressure	January 1946 → December 1949
5001-5912_COADS_MSTG_GROUP4	Wind Speed and Pressure	January 1950 → December 1959
6001-6912_COADS_MSTG_GROUP4	Wind Speed and Pressure	January 1960 → December 1969
7001-7912_COADS_MSTG_GROUP4	Wind Speed and Pressure	January 1970 → December 1979
COADS_MSTG2_GROUP4_8001-8912	Wind Speed and Pressure	January 1980 → December 1989
COADS_G4_90	Wind Speed and Pressure	January 1990 → December 1990

7.3 COADS TIME SERIES

To ascertain whether the COADS monthly data exhibited any major trends over the January 1946 to December 1990 sampling period, time series plots were generated for two widely separated sites: Melbourne, Australia, at 150° E,38° S (Figs. 24–26) and Cape Hatteras, North Carolina, at 75° W,35° N (Figs. 27–29). Separate plots were run for each of the surface parameters, pressure, wind speed, and relative humidity. The data were extracted from individual files, one file per decade, in the NASA CDF, using the program TIMENV in the VAX SEAPAK

package developed at GSFC (McClain et al. 1991a and 1991b). TIMENV produced one ASCII file per site and parameter, the contents of which were plotted using Golden Software Inc.'s Grapher package on an 80486 PC.

Figs. 24 and 29 (wind speed) are the only ones appearing to have a substantial trend. In order to assess whether this trend was observed at the global scale, a COADS time series of monthly wind speed averages was generated (Fig. 30). The series was generated by reading COADS data stored in NASA CDF, using an Interactive Data Language (IDL) program. IDL is an integrated environment from Research Systems, Inc. providing visualization of sci-
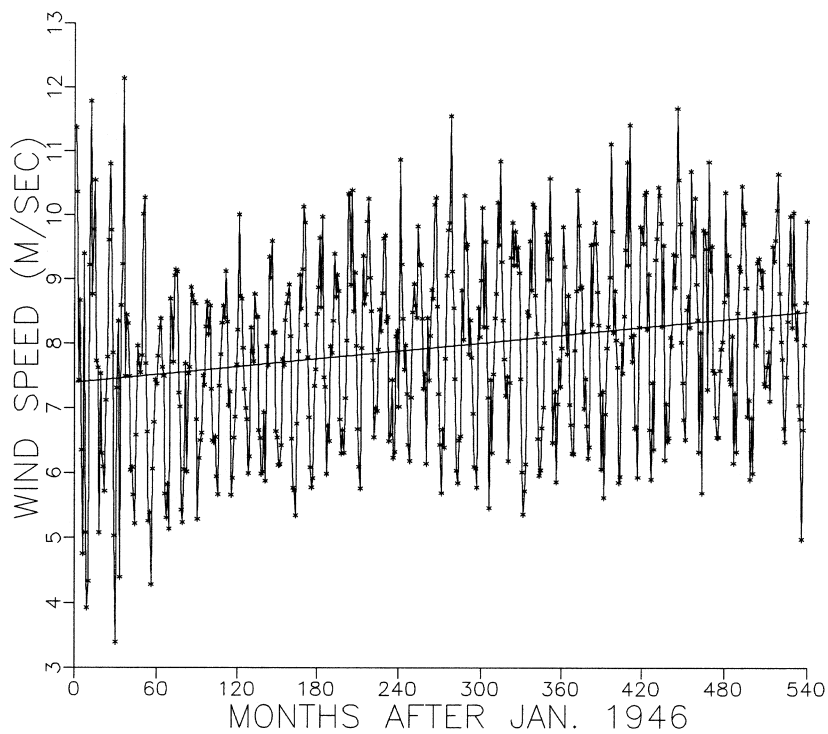
Fig. 24. Time series of monthly COADS surface wind speed at Cape Hatteras, North Carolina, 35N,75W, 1946–1991. The regression for the series is indicated by the solid line.
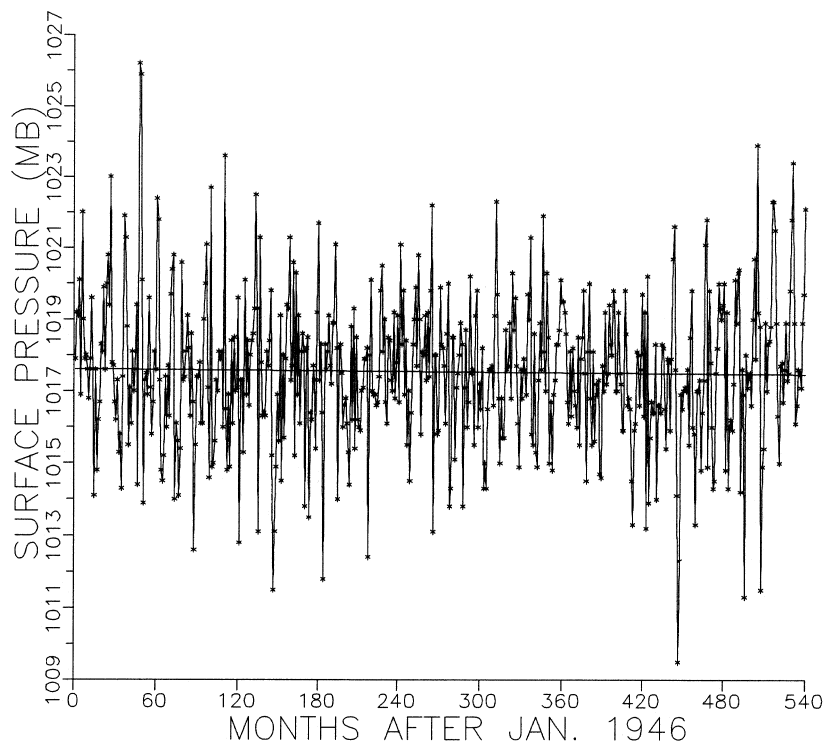
Fig. 25. Time series of monthly COADS surface pressure at Cape Hatteras, North Carolina, 35N,75W, 1946–1991. The regression for the series is indicated by the solid line.
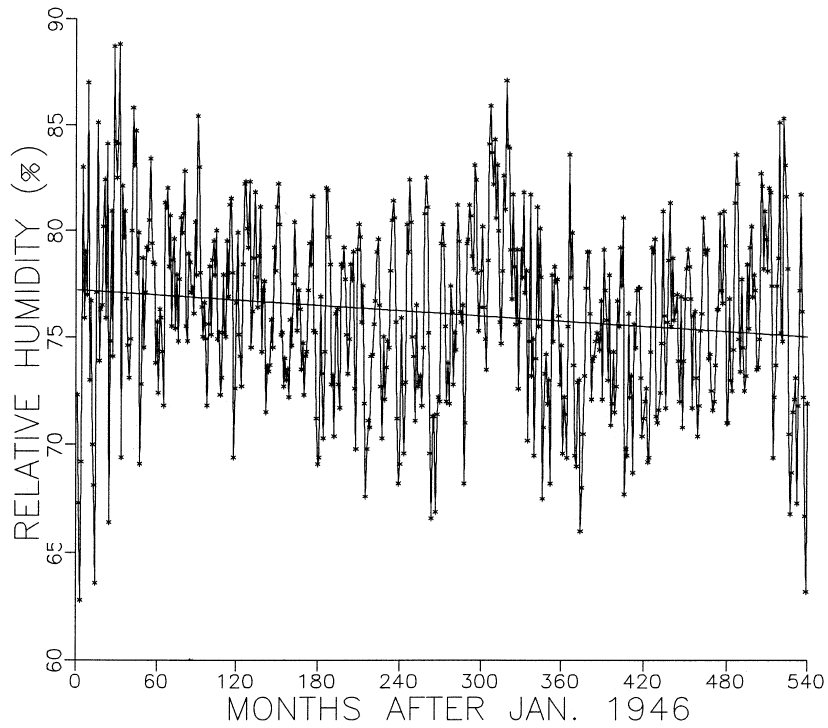
Fig. 26. Time series of monthly COADS surface relative humidity at Cape Hatteras, North Carolina, 35N,75W, 1946–1991. The regression for the series is indicated by the solid line.
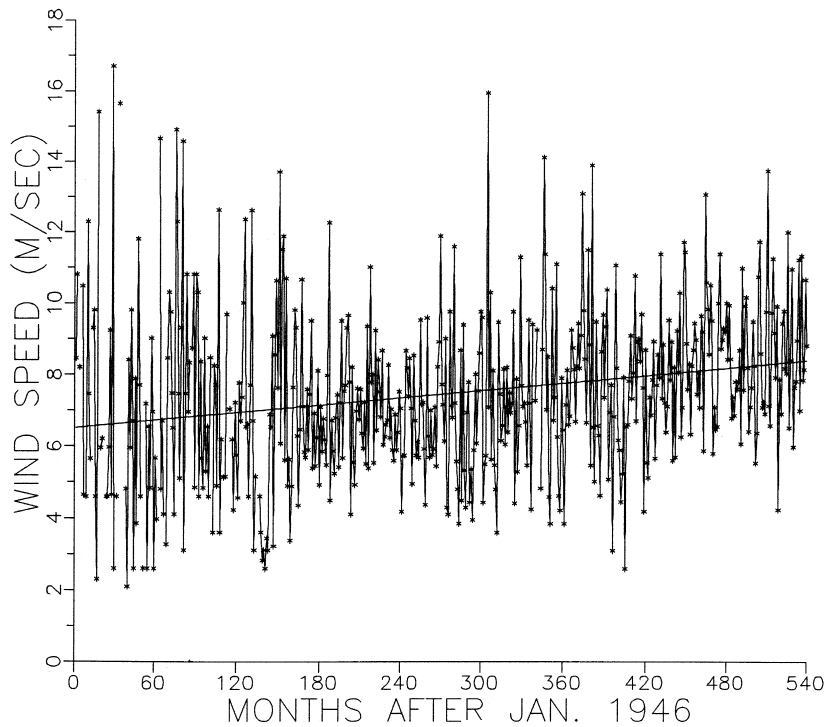
Fig. 27. Time series of monthly COADS surface wind speed at Melbourne, Australia, 38S,150E, 1946–1991. The regression for the series is indicated by the solid line.
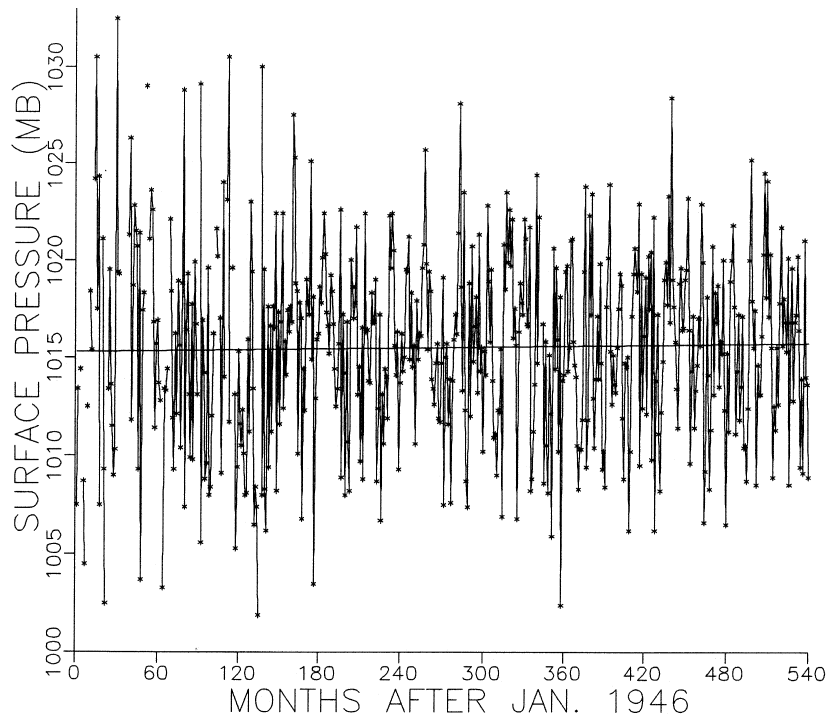
Fig. 28. Time series of monthly COADS surface pressure at Melbourne, Australia, 38S,150E, 1946–1991. The regression for the series is indicated by the solid line.
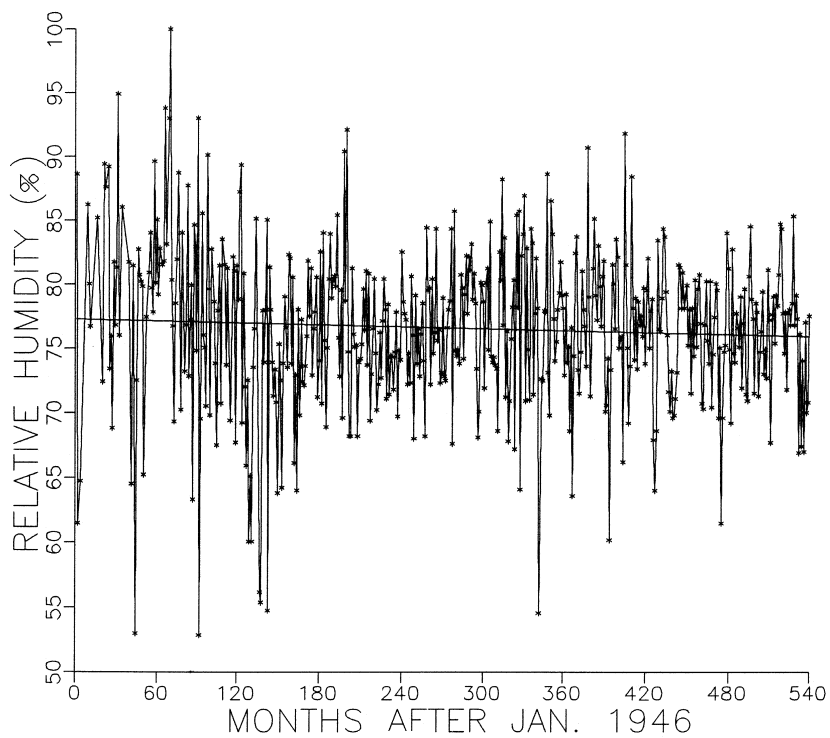
Fig. 29. Time series of monthly COADS surface relative humidity at Melbourne, Australia, 38S,150E, 1946–1991. The regression for the series is indicated by the solid line.
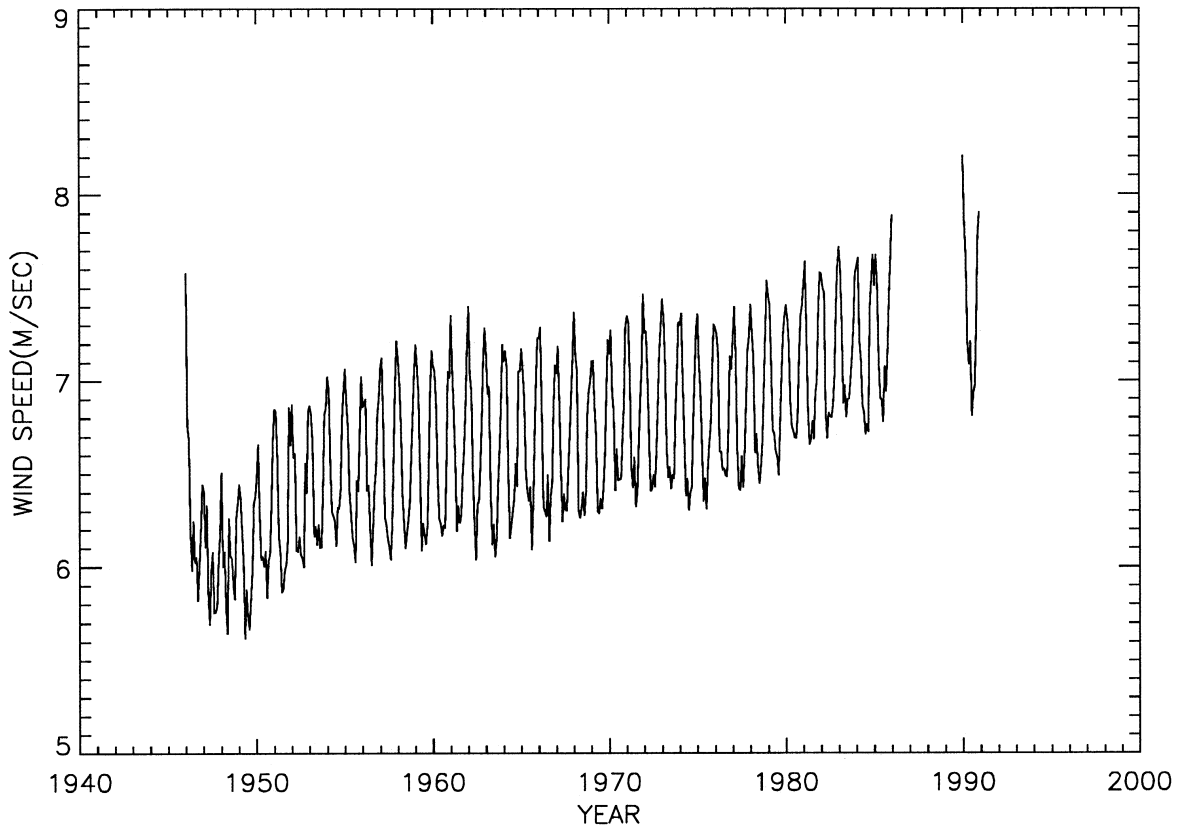
Fig. 30. Time series of monthly global average wind speeds from COADS, 1946–1990.

entific and engineering data arrays, by representing them as images or graphical displays (Research Systems, Inc., 1992a and 1992b). This figure shows a noticeable increase of 1–$1.5\,\mathrm{m\,s^{-1}}$ during the sampling period. However, consistent with the findings of Cardone et al. (1990), it is likely that the increase is explained by the increasing use of anemometers instead of Beaufort scale in the post-1950 era. Also, Cardone et al. point out that the anemometers measure winds at an average height of 19.3 m, rather than the 10 m used for shipborne measurements. In the study, the trends are largely eliminated when winds corrected to 20 m are used throughout. Since the wind (and also, pressure, humidity, and ozone) climatologies are used primarily for qualitative comparisons with near-real time data, as part of the ancillary QC procedure, the presence of a trend would have minimal impact on the generation of SeaWiFS data. Nevertheless, further analyses prior to system integration are planned, so as to determine the most appropriate averaging period for climatology generation. The COADS data set remains the best choice for the climatology, since it contains all three meteorological parameters with a relatively long time record.

7.4 OZONE DATA SET

The total ozone climatology was generated from daily ASCII files, covering the period 1 November 1978 to 31 January 1992, stored on 2 CD-ROMs produced by the NIMBUS TOMS Ozone Processing Team (OPT) at GSFC (Bowman and Krueger 1985). The data in these files were derived from the gridded TOMS (GRIDTOMS) orbital data set, and are global with a resolution of 1.0° in latitude by 1.25° in longitude (180 latitude by 288 longitude points). Since the original grid cells were equal in area, the OPT used an interpolation scheme poleward of 50° latitude to create an equal-angle grid of constant 1.25° longitude resolution.

7.5 CLIMATOLOGY GENERATION

In order to store and verify the data in the climatologies, a set of software programs were written (summarized in Table 15). All software was run under the UNIX operating system on Silicon Graphics, Inc. (SGI) Iris workstations. Program WPHCLM read the COADS GROUP3 and GROUP4 CDF files from disk, after staging from write-once read-many (WORM) times platters attached to a Digital Equipment Corp. (DEC) MicroVAX II system and conversion to a network CDF form readable under UNIX. For humidity climatology creation, GROUP3 CDF files for the decades of 1940–1980 inclusive, and for the year 1990, were read and averages, standard deviations, and the number of observations were generated by month of the year,

e.g., January statistics were computed from January 1946, 1947,...,1990 data, etc.

Similarly, GROUP4 CDF files were read to generate wind speed and atmospheric pressure statistics. Program O3CLM read daily ozone ASCII files furnished by the OPT for the period November 1978 → January 1992. The files were read directly from two CD-ROMs attached to an SGI Iris workstation. Averages, standard deviations, and number of observations were then generated by month of the year and placed in an HDF file (Univ. of Illinois 1989 and 1993), using the same specification as for the meteorological fields.

7.6 DISPLAY AND ANIMATION

Since the meteorological and ozone climatologies will be the only ancillary data source available for generation of the SeaWiFS performance assessment products, it was essential that their accuracy be verified. To accomplish this, the IDL software package was used. Version 3.0 of IDL supports the reading and writing of files stored in the HDF format, for display with the IDL tools. An extensive user-created library provides additional capabilities, including animation of images used to generate movie loops of the monthly statistics in the HDF files.

Two primary IDL procedures were written to facilitate the visualization of the gridded global climatologies stored as Scientific Data Sets (SDS) in HDF files, on an X-windows terminal: SDSIMAGE and SDSANIMATE (see Table 15). SDSIMAGE displays the contents of an SDS residing in an HDF file to an IDL window of any size and position, using user-specified gray scaling, zoom factors, and annotation. A sample call to SDSIMAGE while under the IDL interface is as follows:

```
IDL> img = SDSANIMATE  (mode, hdfnam, sdslab,
          refno, flag, xzoom, yzoom, window,
          sclmin, sclmax, xsize, ysize, xpos,
          ypos, title)
```

where:

img A two-dimensional array containing global wind, pressure, humidity, or ozone data, in a scaled byte (if mode is B or IB) or floating point (if mode is D or ID) representation. The size of the dimensions of img are governed by the data type (COADS or TOMS) and the xzoom and yzoom factors described below.

mode The mode for running a procedure. If D, return floating point data but do not display an image; if ID, return floating point data and display a scaled image; if B, return scaled byte data but do not display an image; and if IB, return scaled byte data and also display a scaled image.

hdfnam HDF name containing the SDS of interest, including full directory specification.

sdslab SDS object annotation (label) pointing to the SDS of interest. If the SDS is located by its reference number (refno), sdslab is ignored. The label can be found by running the NCSA Collage utility, specifying as input the HDF pointed to by hdfnam.

refno SDS reference number pointing to SDS of interest. If the SDS is located by its label, refno is ignored. The reference number can be found by running the NCSA Collage utility, specifying as input the HDF pointed to by hdfnam.

flag An indicator for whether sdslab or refno will be used to identify the SDS of interest. Specify flag=0 to use sdslab, or flag=1 to use refno.

xzoom A zoom factor along the line direction. A bilinear interpolation scheme is used to create values on a new grid, given the original grid, xzoom, and yzoom. A value of 1 will result in no zooming being done.

yzoom A zoom factor along the pixel direction. A bilinear interpolation scheme is used to create values on a new grid, given the original grid, xzoom, and yzoom. A value of 1 will result in no zooming being done.

window ID of IDL window where data will be displayed (ignored for a mode value of B or D). If negative, window will be created, otherwise an existing window is assumed.

sclmin A minimum data value for byte scaling. Data at sclmin will be set to 0 gray level (black), with all values between sclmin and sclmax being linearly scaled to cover the gray range 0–255.

sclmax A maximum data value for byte scaling. Data at sclmax will be set to 255 gray level (white), with all values between sclmin and sclmax being linearly scaled to cover the gray range 0–255.

xsize The size of the IDL window in the x (along-line) direction; valid only for an input value of window less than 0.

ysize The size of the IDL window in the y (along-pixel) direction; valid only for an input value of window less than 0.

xpos The x position of the lower left corner of the IDL window created (in device coordinates).

ypos The y position of the lower left corner of the IDL window created (in device coordinates).

title The title of the IDL display window.

The second procedure, SDSANIMATE, makes successive calls to SDSIMAGE, one per month for the parameter of interest. SDSANIMATE displays a histogram and scaled image for each month in the climatology, at the original grid's resolution. The window with each scaled image exactly
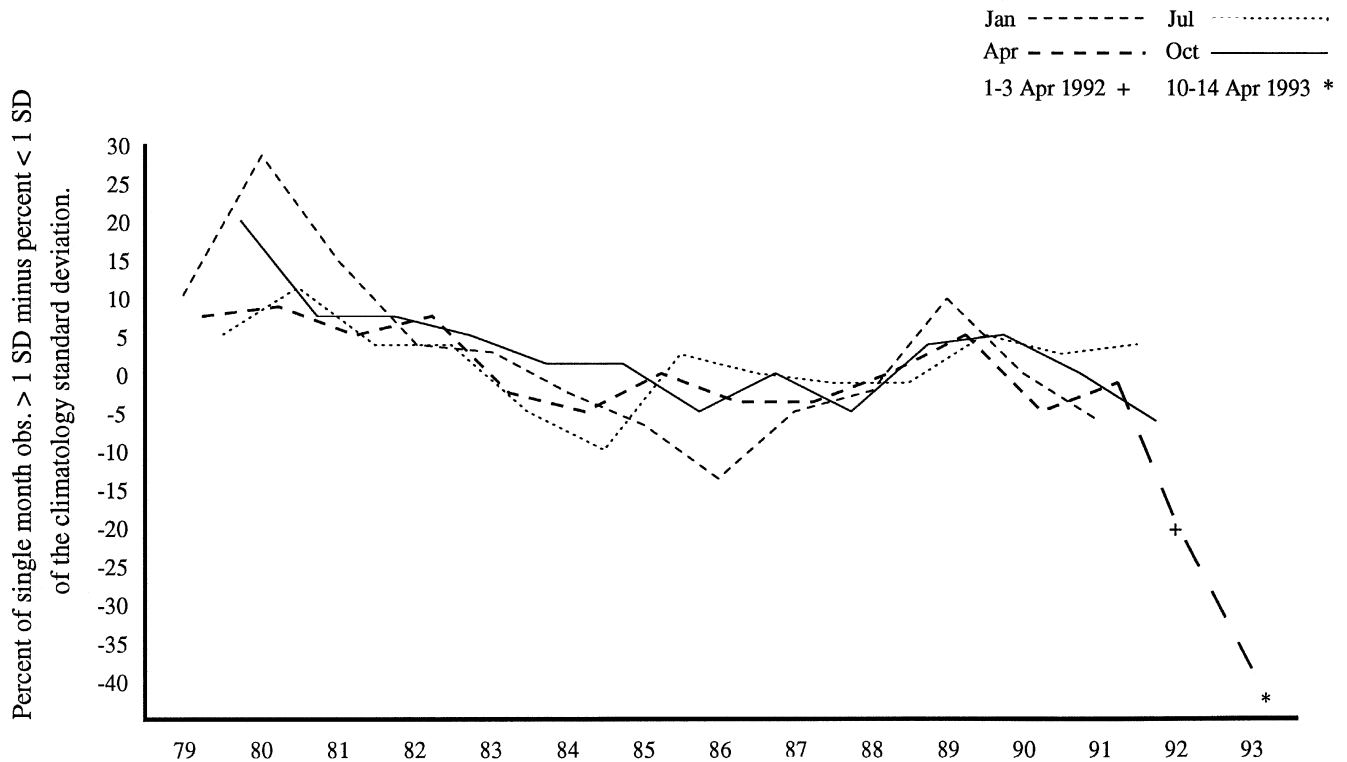
Fig. 31. Comparison of single month ozone distributions versus 13-year climatology.

overlays a window containing a histogram for the image, so the user can switch back and forth between the windows. After the 12 monthly climatology images and histograms are displayed, a loop of the images is begun in a seaparate window. The user can interactively change the looping speed or the color palette applied to the loop.

7.7 DISCUSSION

SDSANIMATE was run on each of the four parameter climatology HDF files as a means of checking the data. The results for the monthly average fields are shown in Plates 15–18. Plate 15 shows the monthly average ozone based on data collected from 1978–1991. Note the migration of the black bands near the poles, indicating a lack of data due to the low sun angle during the winter season in each hemisphere. Also note the low ozone values at the South Pole in October, consistent with findings described in the literature. Likewise, Plates 16, 17, and 18 illustrate familiar global meteorological patterns, such as the zones of high pressure, low relative humidities, and light winds found over the subtropical oceans, as well as, the expected seasonal fluctuations in the magnitude and location of these and other global circulation features.

During the course of this analysis, it has become clear that the averaging period of 13 years for the ozone climatology is too long, given the downward trend in average global ozone during this time. It should also be noted that the downward trend for 1992 and 1993 was even more precipitous than for the period 1978–1991 (Fig. 31). Fig. 31 shows the percentages of observations within each month which are more than 1 standard deviation (1σ) *above* the 13-year climatology standard deviation for that month, as compared with the percentages of observations more than 1σ *below* the 13-year climatology standard deviation. The percentages are plotted for each month during the averaging period. Note the general tendency for more observations to have negative percentages over time, that is, there are relatively more observations one or more standard deviations *below* the climatological value than there are one or more standard deviations *above* climatology.

The trend for more negative percentages has become even more dramatic since 1991, perhaps due to the effects on atmospheric chemistry and circulation of the Mt. Pinatubo volcanic eruption in the Philippines (Kerr 1993 and Gleason et al. 1993). A full 40% more of the observations are greater than 1σ below the mean than are greater than 1σ above the mean, indicating a highly shifted distribution. Therefore, it is likely that a new ozone climatology will be generated prior to the launch of SeaWiFS for use in the SDPS, covering a much shorter period on the order of 2–3 years. If ozone continues on a downward trend over time, the climatology would need to be computed periodically during the lifetime of SeaWiFS.

C. McClain, J. Comiso, R. Fraser, J. Firestone, B. Schieber, E. Yeh, K. Arrigo, and C. Sullivan

Chapter 8

CZCS Sensor Ringing Mask Comparison

CHARLES R. MCCLAIN

NASA Goddard Space Flight Center, Greenbelt, Maryland

EUENG-NAN YEH

General Sciences Corporation, Laurel, Maryland

ABSTRACT

Three different methods for handling CZCS bright target recovery are described and compared. The three techniques are the Mueller (Mueller 1988), SEAPAK (McClain et al. 1991a and 1991b, and Brock et al. 1991), and Miami DSP (Evans and Gordon 1993) methods. A CZCS test scene from the Bering Sea (orbit 2,746 from 10 May 1979) which includes both large and broken clouds, is used for the comparison. The three methods yield similar results in terms of the number of pixels flagged as bright target contaminated and the average pigment values within the scene. If the *additional mask* value in the Miami DSP method is set to the minimum value of one pixel, however, the total number of ringing pixels decreases substantially. The SEAPAK analysis using the Brock et al. inputs seriously underestimates the ringing in the test scene. This is not surprising because the Brock et al. input parameters are optimized for a desert-to-ocean transition rather than a cloud-to-ocean transition.

8.1 INTRODUCTION

The CZCS bright target recovery, also referred to as ringing and electronic overshoot, occurred on the down-scan side of bright objects, such as clouds, ice, or desert regions onto darker areas. The result was anomalous data that could not be corrected resulting in erroneous derived products. The bright target recovery characteristics of the CZCS were not well characterized prior to the launch of the sensor. The occurrence of CZCS ringing was somewhat erratic, at times difficult to predict, and the down-scan extent of the effect was frequently irregular. As a consequence, different analysis methodologies by different investigators were developed in an attempt to determine where and to what (down-scan) extent the data were corrupted.

Three different techniques to quantify CZCS ringing, i.e., the Mueller (1988), Miami DSP, and SEAPAK, (McClain et al. 1991a and 1991b, and Brock et al. 1991) methods, are described and compared. This study was undertaken in preparation for the launch of SeaWiFS which will also exhibit bright target recovery characteristics. It is expected, however, that the effect will be better quantified as a function of bright target exposure duration and radiance during the prelaunch sensor characterization by Hughes/Santa Barbara Research Center (SBRC), the company responsible for building the SeaWiFS instrument.

8.2 THE SEAPAK METHOD

The SEAPAK method utilizes Level-1 670 nm (band 4) and 750 nm (band 5) data. Band 5 is used to identify land and cloud pixels and band 4 is used determine if a ringing mask is to be applied. Fig. 32 shows a schematic of the algorithm. Values for band 4 (`SATGREY`), band 5 (`LANCLD`) and pixel-to-pixel band 4 difference (`DELTA`) thresholds, and the number of pixels (equated to `DISTANCE`) to be masked in the down-scan direction are adjustable on a scene-by-scene basis. If a pixel value exceeds the band 4 and band 5 threshold values, the band 4 grey level value is compared to the value of the adjacent down-scan pixel and, if the difference exceeds the value of `DELTA`, the subsequent N pixels (where N is equal to `DISTANCE`) are masked.

The algorithm is not computationally intensive and is implemented in both user interactive and batch processing modes. The interactive mode allows the input parameters to be varied and the product to be viewed without exiting the program, thereby allowing fine tuning of the input parameter values.

8.3 THE MUELLER METHOD

The Mueller (1988) method uses only band 5. Unlike the SEAPAK method, the ringing distance (in number of pixels) varies as a function of the cumulative excess target brightness and the sensor gain factor G (G equals 1.00,
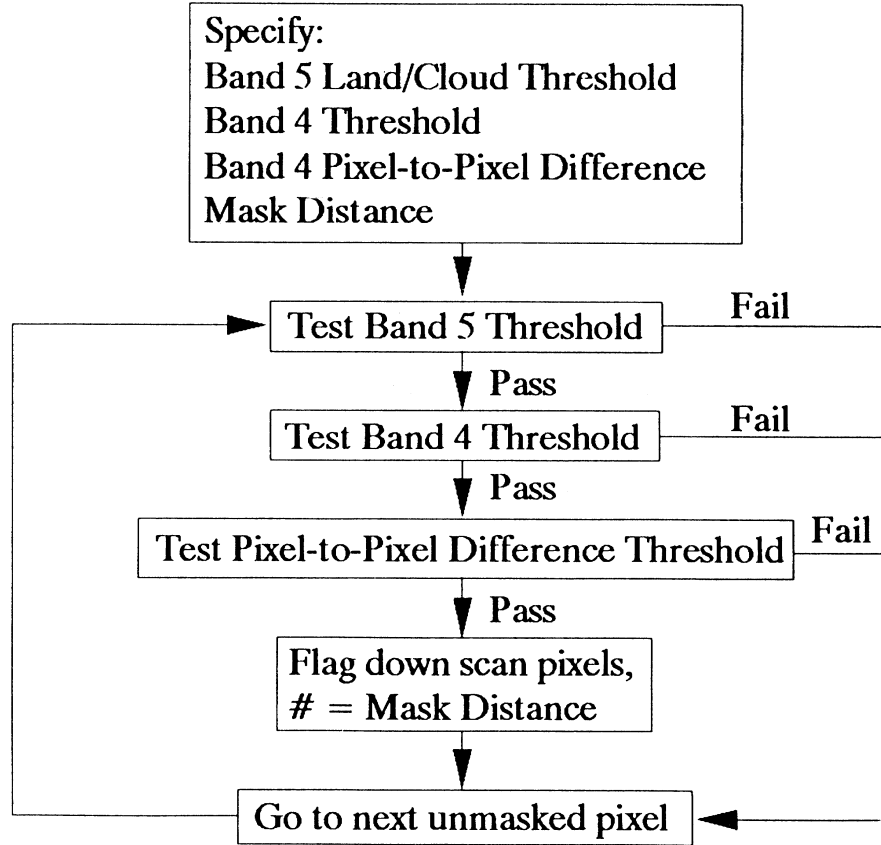
Fig. 32. Processing schematic for the SEAPAK method. A *pass* means the pixel value exceeds the threshold value.

1.25, 1.50, and 2.10 for gains 1–4, respectively). The excess target radiance, B, is computed as:

$$
\begin{aligned}
B &= L_t(750) - \frac{L_c(750)}{G}, \quad \text{if } L_t(750) > \frac{L_c(750)}{G}, \\
B &= 0, \qquad\qquad\qquad\;\; \text{if } L_t(750) \le \frac{L_c(750)}{G},
\end{aligned}
\tag{34}
$$

where $L_t(750)$ is the total 750 nm radiance and $L_c(750)$ is the cloud radiance threshold ($2.45\,\mathrm{mW\ cm^{-2}\ \mu m^{-1}\ sr^{-1}}$). The effect of a bright pixel is assumed to be negligible for distances greater than 50 pixels.

The B values are averaged over 10 pixels to generate five $\langle B \rangle$ values which are used to compute DISTANCE using the formulation

$$
\text{DISTANCE} = \alpha + \beta \big[\ln\langle B \rangle_s + \ln G \big],
\tag{35}
$$

where α and β were estimated to be 3.9 and 30.8, respectively, and

$$
\langle B \rangle_s = \sum_{i=1}^{5} \langle B \rangle_i e^{-0.32i}.
\tag{36}
$$

The input values for the Mueller method used on the test scene are listed in Table 16.

Table 16. Algorithm input values used for this study.

SEAPAK Method	
LANCLD†	Grey Level = 21
SATGREY	Grey Level = 210
DELTA	Grey Level = 10
DISTANCE	4 and 20 pixels
Mueller Method	
α (intercept)	3.9 pixels
β (slope)	30.8 pixels
$L_c(750)$	$2.45\,\mathrm{mW\ cm^{-2}\ \mu m^{-1}\ sr^{-1}}$
Miami DSP Method	
Saturation Threshold	Grey Level = 60
Difference Threshold	Grey Level = 9
Cloud Mask Value‡	Grey Level = 255
Maximum Distance	40 pixels
Additional Mask	20 pixels

†Band 5 ‡Corresponds to LANCLD=21

8.4 THE MIAMI DSP METHOD

The method applied in the Miami DSP system uses the CZCS level-2 normalized water-leaving radiances at 520 nm, $L_{WN}(520)$, as a reference to determine the extent

of sensor overshoot in the open ocean (Evans and Gordon 1993). In the generation of the level-2 products, a land and cloud mask is applied using a constant threshold radiance in band 5. Pixels down-scan of a bright target are flagged if $L_{WN}(520)$ exceeds a saturation threshold $(0.7\,\mathrm{mW}\ \mathrm{cm}^{-2}\ \mu\mathrm{m}^{-1}\ \mathrm{sr}^{-1})$ or the difference between successive pixels exceeds a difference threshold $(0.1\,\mathrm{mW}\ \mathrm{cm}^{-2}\ \mu\mathrm{m}^{-1}\ \mathrm{sr}^{-1})$. The normalized water-leaving radiance values for the range of 0–$3.0\,\mathrm{mW}\ \mathrm{cm}^{-2}\ \mu\mathrm{m}^{-1}\ \mathrm{sr}^{-1}$ are scaled to grey scales from 0–255, respectively.

The values of 0.7 and $0.1\,\mathrm{mW}\ \mathrm{cm}^{-2}\ \mu\mathrm{m}^{-1}\ \mathrm{sr}^{-1}$ equate to grey levels of 60 and 9, respectively, for the saturation and difference thresholds. The threshold tests are applied over a maximum distance of 40 pixels in down-scan direction of a bright pixel. Finally, additional pixels are added unconditionally to the ringing mask. For the global CZCS processing (Feldman et al. 1989), 20 pixels (or equivalently, 5 GAC pixels) were added to the mask. Input values for the Miami DSP method are listed in Table 16 and are the equivalent values as those used in the global CZCS processing.

8.5 RESULTS

The CZCS scene used for this study is a Bering Sea scene (orbit 2,746, 10 May 1979, and sequential day 130) which was chosen because it includes both large clouds and broken clouds. Plate 19 depicts the pigment concentrations with white (a grey value of 255) representing pixels flagged by the land/cloud and ringing masks. The upper left panel represents the case where only the land/cloud mask (band 5 at 21 counts) was applied resulting in 45% of the data being identified as either land or clouds. Pixels seriously affected by ringing can be easily identified as very low pigment on the down-scan side of the clouds. The results of the three ringing mask algorithms are summarized in Tables 17 and 18.

The SEAPAK input values applied to the Bering Sea test scene (Plate 19) are listed in Table 16 for two cases. The first case applies values derived by Brock et al.

(1991) based on analyses of many scenes from the Arabian Sea (DISTANCE equal to 4). Their analyses emphasized data from scans transitioning from the Arabian desert to the ocean. The second case uses DISTANCE equal to 20 based on an interactive analysis of the Bering Sea scene.

Table 17. Results of sensor ringing mask algorithm comparison. The total number of pixels in the scene is 262,144. For SEAPAK 1 DISTANCE is equal to 4 and for SEAPAK 2 DISTANCE is equal to 20.

Method Used	Flagged (F)	Ringing (R)	R/F_{NoMask} Ratio
No Mask	117,123†	0	0.0%
SEAPAK 1	144,531	27,408	23.4
SEAPAK 2	196,145	79,022	67.5
Mueller	212,829	95,706	81.7
Miami DSP	210,413	93,290	79.7

† The total number of land and cloud pixels.

Table 18. Mean (μ) pigment concentrations and standard deviations (σ) for various ringing mask algorithms (valid range is 0.042–$37.8\,\mathrm{mg}\ \mathrm{m}^{-3}$).

Method	μ	σ
No Mask	2.40	4.14
SEAPAK 2	3.50	4.94
Mueller	3.36	4.79
Miami DSP	3.74	5.25

The SEAPAK (DISTANCE equal to 20), Mueller, and Miami DSP methods yielded similar results in terms of the number of pixels flagged and average pigment values. If the *additional mask* value in the Miami DSP method is set to the minimum value of one pixel, the total number of ringing pixels decreases substantially to 51,720. The SEAPAK analysis using the Brock et al. inputs seriously underestimated the ringing in the Bering Sea scene (not shown). This is not entirely surprising because the parameters were optimized for a desert-to-ocean transition rather than a cloud-to-ocean transition.

Chapter 9

Sun Glint Flag Sensitivity Study

CHARLES R. MCCLAIN
NASA Goddard Space Flight Center, Greenbelt, Maryland

EUENG-NAN YEH
General Sciences Corporation, Laurel, Maryland

ABSTRACT

The statistical wind speed dependent surface slope distribution of Cox and Munk (1954a and 1954b) is used to estimate the sun glint affected area in a CZCS image. The probability of a pixel being contaminated by glitter is a function of sea surface wind speed and satellite viewing geometry. In the sample case presented, the areal extent of the flag expands very little as wind speed increases beyond about $7\,\mathrm{m\ s^{-1}}$.

9.1 INTRODUCTION

The ocean surface waves deform the ocean surface resulting in randomly oriented facets which reflect incoming solar radiance in many directions other than the direction of specular reflection from a flat surface. Directly reflected light can result in saturation of the CZCS bands and the standard atmospheric correction algorithm (Gordon et al. 1988) does not explicitly estimate the sun glint radiance, although, low levels of sun glint are removed from the imagery because the algorithm interpreted glint radiance as aerosol radiance. Ocean color sensors are equipped with the capability of tilting the scan plane away from the sun in order to minimize the glint effect. However, under certain conditions (low solar zenith angle or moderate to high wind speeds) it is difficult to avoid sun glint.

The statistical model of wind wave slope distribution proposed by Cox and Munk (1954a and 1954b) and discussed in Viollier et al. (1980) assumes that the distribution of wave facet orientation is approximately isotropic and Gaussian and is solely a function of surface wind velocity. Consequently, with knowledge of the solar and observation viewing geometry, the pattern and intensity of the reflected solar radiance can be estimated.

9.2 METHOD

Plate 20 depicts pigment concentrations derived from a CZCS Mediterranean Sea image (orbit 2,573, 20 April 1979, sequential day 110) having a scanner tilt angle of zero degrees. The relatively high pigment values (blue and green areas of upper left panel) near the scene center are the result of sun glint corruption, and should be flagged as

invalid. The CZCS level-2 processing and glint flag analyses processing were accomplished using SEAPAK (McClain et al. 1991a and 1991b).

The probability of a pixel being contaminated by glitter is a function of sea surface wind speed, W, and satellite viewing geometry, namely, the solar azimuth and zenith angles (Φ_0 and θ_0, respectively) and satellite azimuth and zenith angles (Φ and θ, respectively). A probability parameter, P_σ, is defined by

$$P_\sigma \;=\; \frac{1}{\pi\sigma^2}\,\exp\left[\frac{-\tan^2\theta_n}{\sigma^2}\right], \qquad (37)$$

where σ^2 is the mean square surface slope distribution which increases linearly with wind speed:

$$\sigma^2 \;=\; 0.003 + 0.00512\,W \qquad (38).$$

The zenith angle, θ_n, of the vector normal to the surface vector for which glint will be observed can be derived from the surface reflection angle, ω:

$$\cos 2\omega \;=\; cos\theta\cos\theta_0 + \sin\theta\sin\theta_0\cos(\Phi-\Phi_0), \quad (39)$$

where

$$\theta_n \;=\; \cos^{-1}\left[\frac{\cos\theta+\cos\theta_0}{2\cos\omega}\right]. \qquad (40)$$

A pixel will be flagged as sun glint contaminated if the calculated value of P_σ is greater than, or equal to, a given threshold value. For a known viewing geometry, the sea surface wind speed and the assigned threshold value, (an estimate of the sun glint affected area) can be determined. The number of pixels flagged decreases as the threshold value increases, and increases with wind speed (37).

C. McClain, J. Comiso, R. Fraser, J. Firestone, B. Schieber, E. Yeh, K. Arrigo, and C. Sullivan

Plate 20 shows the sun glint flags for different sea surface wind speeds (1, 3, 5, 7, 9, 11, and 13 m s^{-1}) and threshold values (1.0, 1.5, and 2.0). The First GARP (Global Atmospheric Research Program) Global Experiment (FGGE) 1,000 mb wind speed and the FNOC surface wind speed at the center of the scene at local noon were both 5 m s^{-1}. This indicates that a P_σ value between 1.5 and 2.0 is optimal, i.e., all contaminated pixels are flagged with a minimum amount of loss of valid data.

9.3 CONCLUSIONS

If the ocean were a perfectly flat surface, the mirror image of the reflected sun would be seen at the single specular point. As the wind speed increases, the ocean surface is ruffled by the wind and the glint area expands. The Cox and Munk algorithm can be used to estimate the areal extent of the contaminated region. The procedure described above requires values for P_σ and W. In the case presented, a value of $P_\sigma = 1.5$ would be an adequate value. This example indicates that the areal extent of the flag expands very little as wind speed increases beyond about 7 m s^{-1}. Other approaches would be to estimate the sun glint radiance as described in Viollier et al. (1980) and remove the glint explicitly from the total observed radiance, or simply to set a flag based on some threshold value of the glint radiance.

Glossary

ASCII	American Standard Code for Information Interchange
Case 1	Water whose reflectance is determined solely by absorption.
Case 2	Water whose reflectance is significantly influenced by scattering.
CDF	(NASA) Common Data Format
CD-ROM	Compact Disk-Read Only Memory
CEC	Commission of the European Communities
CIRES	Cooperative Institute for Research in Environmental Sciences
COADS	Comprehensive Ocean-Atmosphere Data Set
CVT	Calibration and Validation Team
CZCS	Coastal Zone Color Scanner
DAAC	Distributed Active Archive Center
DEC	Digital Equipment Corporation
DSP	Not an acronym, an image display and analysis package developed at RSMAS University of Miami.
EOSDIS	Earth Observing System Data and Information System
ERL	(NOAA) Environmental Research Laboratories
ESA	European Space Agency
FGGE	First GARP Global Experiment
FNOC	Fleet Numerical Oceanography Center
GARP	Global Atmospheric Research Program
GMT	Greenwich Mean Time
GP	Global Processing (algorithm)
GRIDTOMS	Gridded TOMS (data set)
GSFC	Goddard Space Flight Center
HDF	Hierarchical Data Format
IDL	Interactive Data Language
JGOFS	Joint Global Ocean Flux Study
JRC	Joint Research Center
Level-0	Raw data.
Level-1	Calibrated radiances.
Level-2	Derived products.
Level-3	Gridded and averaged derived products.
NASA	National Aeronautics and Space Administration
NCAR	National Center for Atmospheric Research
NCDC	(NOAA) National Climatic Data Center
NCDS	NASA Climate Data System
NCSA	National Center for Supercomputing Applications
NET	NIMBUS Experiment Team
NIMBUS	Not an acronym, a series of NASA experimental weather satellites containing a wide variety of atmosphere, ice, and ocean sensors.
NMC	National Meteorological Center
NOAA	National Oceanic and Atmospheric Administration
NSSDC	National Space Science Data Center
OCEAN	Ocean Colour European Archive Network
OPT	Ozone Processing Team
PC	(IBM) Personal Computer
QC	Quality Control
RSMAS	Rosenstiel School for Marine and Atmospheric Sciences (University of Miami)

SDPS	SeaWiFS Data Processing System
SDS	Scientific Data Set
SEAPAK	Not an acronym, an image display and analysis package developed at GSFC.
SeaWiFS	Sea-viewing Wide Field-of-view Sensor
SGI	Silicon Graphics, Inc.
SO	Southern Ocean (algorithm)
TOMS	Total Ozone Mapping Spectrometer
UARS	Upper Atmosphere Research Satellite
UTM	Universal Transverse Mercator (projection)
UV	Ultraviolet
VAX	Virtual Address Extension
WORM	Write Once Read Many (times)

Symbols

a	Formulation coefficient
$A(k)$	Absorptivity.
b	Formulation coefficient
B	Excess target radiance
C	Chlorophyll a pigment, or just pigment concentration.
$[C + P]$	Pigment concentration defined as mg chlorophyll a plus phaeopigments m^{-3}.
C_{13}	Pigment concentration derived using CZCS bands 1 and 3.
C_{23}	Pigment concentration derived using CZCS bands 2 and 3.
d_i	Distance from the ith observation point to the point of interest.
d_j	Distance from the jth observation point to the point of interest.
$E_{\rm rem}$	Percentage of energy removed from a wavelength band.
$F_0(\lambda)$	Incident solar irradiance.
$G(\lambda)$	$\dot{R}_a(\lambda_i)/\dot{R}_a(670) = (670/\lambda)^\gamma\, T_{2r}(670)/T_{2r}(\lambda_i)$
i	Interval index.
I_0	Incident radiant intensity.
I_1	Radiant intensity after traversing through an absorbing medium.
I_2	Reflected radiant energy received by the satellite sensor.
j	Interval index.
k	Wavenumber of light $(1/\lambda)$.
k_1	Beginning wavenumber
k_2	Ending wavenumber
$L(\lambda)$	Radiance.
$L_a(\lambda)$	Aerosol radiance.
$L_c(\lambda)$	Cloud radiance threshold
$L_r(\lambda)$	Rayleigh radiance.
$L_{r0}(\lambda)$	Rayleigh radiance at standard atmospheric pressure, P_0.
$L_s(\lambda)$	Subsurface water radiance.
$L_t(\lambda)$	Total radiance at the sensor.
$L_u(\lambda)$	Upwelled spectral radiance.
$L_W(\lambda)$	Water-leaving radiance.

C. McClain, J. Comiso, R. Fraser, J. Firestone, B. Schieber, E. Yeh, K. Arrigo, and C. Sullivan

m	Index of refraction.
$n(\lambda)$	An exponent conceptually similar to the Ångström exponent.
N	Total number of points or pixels.
P	Phaeopigment concentration.
P_0	Standard atmospheric pressure (1,013.25 mb).
P_σ	Phaeopigment concentration.
q	Water transmittance factor.
R	Reflectance.
R_a	Aerosol reflectance.
$\dot{R}_a$	$R_a/(qT_{2r})$.
R_r	Rayleigh reflectance.
R_s	Subsurface reflectance.
R_t	Total reflectance at the sensor.
$\dot{R}_t$	$(R_t - R_r)/(qT_{2r})$.
$S(\lambda)$	$L_a(\lambda)/L_a(670)$.
t_1	First observation time.
t_2	Second observation time.
$t(k)$	Spectral transmission as a function of wavenumber.
$t(\lambda)$	Diffuse transmittance of the atmosphere.
T_{2r}	Two-way diffuse transmittance for Rayleigh attenuation.
T_{oz}	Diffuse transmittance of ozone.
$V_i(t_j)$	The ith spatial location at observation time t_j.
W	Wind speed.
x	Abscissa or longitudinal coordinate.
y	Ordinate or meridional coordinate.
α	Percent albedo, tilt angle, or formulation coefficient (intercept).
β	Formulation coefficient (slope)
γ	Ångström exponent.
Δk	Equivalent bandwidth.
ΔP	Pressure deviation from standard pressure, P_0.
θ	Satellite zenith angle.
θ_0	Solar zenith angle.
θ_n	The zenith angle of the vector normal to the surface vector for which glint will be observed.
λ	Wavelength of light.
μ	Mean value or cosine of the satellite zenith angle.
μ_0	Cosine of the solar zenith angle.
ν_j	The jth temporal weighting factor.
ρ	Fresnel reflectivity.
σ	Standard deviation.
σ^2	The mean square surface slope distribution.
τ_{ox}	Oxygen optical thickness at 750 nm.
τ_r	Rayleigh optical thickness.
τ_{r0}	Rayleigh optical thickness at standard atmospheric pressure, P_0.
Φ	Satellite azimuth angle.
Φ_0	Solar azimuth angle.
ω	The surface reflection angle.
ω_i	Spatial weighting factor.

REFERENCES

Andersen J.H., 1991: CZCS level 2 generation. *OCEAN Technical Series, Nos. 1–8, Ocean Colour European Archive Network,* 49 pp.

Anderson, R.F., 1992: Southern Ocean processes study. *U.S. JGOFS Planning Report Number 16,* Woods Hole Oceanographic Institution, Woods Hole, Massachusetts, 114 pp.

André, J.-M. and A. Morel, 1989: Simulated effects of barometric pressure and ozone content upon the estimate of marine phytoplankton from space. *J. Geophys. Res.,* **94,** 1,029–1,037.

——, and ——, 1991: Atmospheric corrections and interpretation of marine radiances in CZCS imagery, revisited. *Oceanol. Acta,* **14,** 3–22.

Ångström , A., 1964: The parameters of atmospheric turbidity. *Tellus,* **16,** 64–75.

Balch, W.M., R. Evans, J. Brown, G. Feldman, C.R. McClain, and W. Esaias, 1992: The remote sensing of ocean primary productivity: Use of a new data compilation to test satellite algorithms. *J. Geophys. Res.,* **97,** 2,279–2,290.

Banse, K., and C.R. McClain, 1986: Satellite-observed winter blooms of phytoplankton in the Arabian Sea. *Mar. Ecol.,* **34,** 201–211.

Barale, V., C.R. McClain, and P. Malanotte-Rizzoli, 1986: Space and time variability of the surface color field in the northern Adriatic Sea. *J. Geophys. Res.,* **91,** 12,957–12,974.

Bowman, K.P., and A.J. Krueger, 1985: A global climatology of total ozone from the Nimbus 7 Total Ozone Mapping Spectrometer. *J. Geophys. Res.,* **90,** 7,967–7,976.

Bricaud, A., and A. Morel, 1987: Atmospheric corrections and interpretation of marine radiances in CZCS imagery: use of a reflectance model. *Oceanol. Acta,* **7,** 33–50.

Brock, J.C., C.R. McClain, M.E. Luther, and W.W. Hay, 1991: The phytoplankton bloom in the northwest Arabian Sea during the southwest monsoon of 1979. *J. Geophys. Res.,* **96,** 20,623–20,642.

——, and ——, 1992: Interannual variability in phytoplankton blooms observed in the northwestern Arabian Sea during the southwest monsoon. *J. Geophys. Res.,* **97,** 733–750.

Cardone, V.J., J.G. Greenwood, and M.A. Cane, 1990: On trends in historical marine wind data. *J. Climate,* **3,** 113–127.

Clark, D.K., 1981: Phytoplankton pigment algorithms for the Nimbus-7 CZCS. *Oceanography from Space,* J.F.R. Gower, Ed., Plenum Press, New York 227–237.

Comiso, J.C., N.G. Maynard, W.O. Smith, Jr., and C.W. Sullivan, 1990: Satellite ocean color studies of Antarctic ice edges in summer/autumn. *J. Geophys. Res.,* **95,** 9,481–9,496.

——, C.R. McClain, C.W. Sullivan, J.P. Ryan, and C.L. Leonard, 1993: Coastal Zone Color Scanner pigment concentrations in the Southern Ocean and relationships to geophysical surface features. *J. Geophys. Res.,* **98,** 2,419–2,451.

Cox, C., and W. Munk, 1954a: Measurement of the roughness of the sea surface from photographs of the sun's glitter. *J. Opt. Soc. Am.,* **44,** 838–850.

——, and ——, 1954b: Statistics of the sea surface derived from sun glitter. *J. Mar. Res.,* **13,** 198–277.

Curran, R.J., 1972: Ocean color determination through a scattering atmosphere. *Appl. Opt.,* **11,** 1,857–1,866.

——, H.L. Kyle, L.R. Blaine, J. Smith, and T.D. Clem, 1981: Multichannel scanning radiometer for remote sensing cloud physical parameters. *Rev. Sci. Instrum.,* **52,** 1,546–1,555.

Darzi, M., 1992: Cloud Screening for Polar Orbiting Visible and IR Satellite Sensors, *NASA Tech. Memo. 104566, Vol. 7,* S.B. Hooker and E.R. Firestone, Eds., NASA Goddard Space Flight, Greenbelt, Maryland, 7 pp.

Eckstein, B.A., and J.J. Simpson, 1991: Cloud screening Coastal Zone Color Scanner images using channel 5. *Int. Remote Sensing,* **12,** 2,359–2,377.

Esaias, W., G. Feldman, C.R. McClain, and J. Elrod, 1986: Satellite observations of oceanic primary productivity. *Eos Trans. AGU,* **67,** 835–837.

Evans, R.H., and H.R. Gordon, 1993: CZCS "system calibration:" a retrospective examination. *J. Geophys. Res.,* (submitted).

Fasham, M.J.R., H.W. Ducklow, and S.M. McKelvie, 1990: A nitrogen-based model of plankton dynamics in the oceanic mixed layer. *J. Mar. Res.,* **48,** 591–639.

Feldman, G., N. Kuring, C. Ng, W. Esaias, C. McClain, J. Elrod, N. Maynard, D. Endres, R. Evans, J. Brown, S. Walsh, M. Carle, and G. Podesta, 1989: Ocean Color: Availability of the global data set. *Eos Trans. AGU,* **70,** 634.

Firestone, J.K., G. Fu, M. Darzi, and C.R. McClain, 1990: NASA's SEAPAK software for oceanographic data analysis: An update. *Proc. Sixth Int. Conf. Interactive Information Processing Systems for Meteor., Oceanogr., and Hydrol.,* Am. Meteor. Soc., Anaheim, California, 260–267.

Frost, B.W., 1991: The role of grazing in nutrient rich areas of the open seas. *Limnol. Oceanogr.,* **36,** 1,616–1,630.

Fukuchi, M., 1980: Phytoplankton chlorophyll stocks in the Antarctic ocean. *J. Oceanogr. Soc. Japan,* **36,** 73–84.

Gleason, J.F., P.K. Bhartia, J.R. Herman, R. McPeters, P. Newman, R.S. Stolarski, L. Flynn, G. Labow, D. Larko, C. Seftor, C. Wellemeyer, W.D. Komhyr, A.J. Miller, and W. Planet, 1993: Record low global ozone in 1992. *Science,* **260,** 523–526.

Gordon, H.R., 1978: Removal of atmospheric effects from satellite imagery of the oceans. *Appl. Opt.,* **17,** 1,631–1,636.

——, and D.K. Clark, 1981: Clear water radiances for atmospheric correction of Coastal Zone Color Scanner imagery. *Appl. Opt.,* **20,** 4,175–4,180.

——, ——, J.W. Brown, O.B. Brown, R.H. Evans, and W.W. Broenkow, 1983: Phytoplankton pigment concentrations in the Middle Atlantic Bight: Comparison of ship determinations and CZCS estimates. *Appl. Opt.,* **22,** 20–36.

——, and D.J. Castaño, 1987: Coastal Zone Color Scanner atmospheric correction algorithm: multiple scattering effects. *Appl. Opt.,* **11,** 2,111–2,122.

——, J.W. Brown, and R.H. Evans, 1988: Exact Rayleigh scattering calculations for use with the Nimbus-7 Coastal Zone Color Scanner. *Appl. Opt.,* **27,** 862–871.

Hooker, S.B., W.E. Esaias, G.C. Feldman, W.W. Gregg, and C.R. McClain, 1992: An Overview of SeaWiFS and Ocean Color. *NASA Tech. Memo. 104566, Vol. 1,* S.B. Hooker and E.R. Firestone, Eds., NASA Goddard Space Flight Center, Greenbelt, Maryland, 24 pp.

——, C.R. McClain, and A. Holmes, 1993: Ocean color imaging: CZCS to SeaWiFS. *Mar. Tech. Soc. J.,* **27,** 3–15.

Kerr, R.A., 1993: Ozone takes a nose dive after the eruption of Mt. Pinatubo. *Science,* **260,** 490–491.

McClain, C.R., and L.P. Atkinson, 1985: A note on the Charleston Gyre. *J. Geophys. Res.,* **90,** 11,857–11,861.

——, J.A. Yoder, L.P. Atkinson, J.O. Blanton, T.N. Lee, J.J. Singer, and F.E. Muller-Karger, 1988: Variability of surface pigment concentrations in the South Atlantic Bight. *J. Geophys. Res.,* **93,** 10,675–10,697.

——, M. Darzi, J. Firestone, E-n. Yeh, G. Fu, and D. Endres, 1991a: SEAPAK Users Guide, Version 2.0, Vol. I—System Description. *NASA Tech. Memo. 100728,* 158 pp.

——, ——, ——, ——, ——, and ——, 1991b: SEAPAK Users Guide, Version 2.0, Vol. II—Descriptions of Programs. *NASA Tech. Memo. 100728,* NASA Goddard Space Flight Center, Greenbelt, Maryland, 586 pp.

——, C.J. Koblinsky, J. Firestone, M. Darzi, E-n. Yeh, and B. Beckley, 1991c: An examination of some Southern Ocean data sets, *EOS Trans. AGU,* **72,** 345–351.

——, W.E. Esaias, W. Barnes, B. Guenther, D. Endres, S.B. Hooker, G. Mitchell, and R. Barnes, 1992a: Calibration and Validation Plan for SeaWiFS, *NASA Tech. Memo. 104566, Vol. 3,* S.B. Hooker and E.R. Firestone, Eds., NASA Goddard Space Flight Center, Greenbelt, Maryland, 41 pp.

——, E-n. Yeh, and G. Fu, 1992b: An Analysis of GAC Sampling Algorithms: A Case Study. *NASA Tech. Memo. 104566, Vol. 4,* S.B. Hooker and E.R. Firestone, Eds., NASA Goddard Space Flight Center, Greenbelt, Maryland, 20 pp.

Mitchell, B.G., and O. Holm-Hansen, 1991: Bio-optical properties of Antarctic peninsula waters: Differentiation from temperate ocean models. *Deep-Sea Res.,* **38,** 1,009–1,028.

Morel, A., and L. Prieur, 1977: Analysis of variations in ocean color. *Limnol. Oceanogr.,* **22,** 709–722.

Mueller, J.L., 1988: Nimbus-7 CZCS: electronic overshoot due to cloud reflectance. *Appl. Opt.,* **27,** 438–440.

——, 1993: The First SeaWiFS Intercalibration Round-Robin Experiment, SIRREX-1, July 1992. *NASA Tech. Memo. 104566, Vol. 14,* S.B. Hooker and E.R. Firestone, Eds., NASA Goddard Space Flight Center, Greenbelt, Maryland, 60 pp.

——, and R.W. Austin, 1992: Ocean optics protocols. *NASA Tech. Memo. 104566, Vol. 5,* S.B. Hooker and E.R. Firestone, Eds., NASA Goddard Space Flight Center, Greenbelt, Maryland, 45 pp.

Muller-Karger, F.E., C.R. McClain, T.R. Fisher, W.E. Esaias, and R. Varela, 1989: Pigment distribution in the Caribbean Sea: Observations from space. *Prog. Oceanogr.,* **23,** 23–64.

——, ——, R.N. Sambrotto, and G.C. Ray, 1990: A comparison of ship and CZCS-mapped distributions of phytoplankton in the Southeastern Bering Sea. *J. Geophys. Res.,* **95,** 11,483–11,499.

National Space Science Data Center, 1991: NSSDC CDF User's Guide for UNIX Systems, version 2.1. *Publication NSSDC-WDC-A-R&S 91-30,* 245 pp.

——, 1993: NODIS (NSSDC's On-line Data and Information Service) [database on-line] Master Directory [cited July 1993] Data Set Information Search; identifier: Multiple Key Word Search—TOMS and COADS.

Olsen, L.M., and C.R. McClain, 1992: Cooperative efforts in support of ocean research through NASA's Climate Data System. *Proc. Eighth Int. Conf. on Interactive Inform. and Processing Systems for Meteor., Oceanogr., and Hydrol.,* Am. Meteor. Soc., 206–211.

Platt, T., and S. Sathyendranath, 1988: Ocean primary production: Estimation by remote sensing at local and regional scales. *Science,* **241,** 1,613–1,620.

Research Systems, Inc., 1992a: *Interactive Data Language (IDL) User's Guide, Ver. 3.0.* Boulder, Colorado, 356 pp.

——, 1992b: *Interactive Data Language (IDL) Reference Guide, Version 3.0.* Boulder, Colorado, 424 pp.

Slutz, R.J., S.J. Lubker, J.D. Hiscox, S.D. Woodruff, R.L. Jenne, P.M. Steurer, and J.D. Elms, 1985: *Comprehensive Ocean-Atmosphere Data Set; Release 1.* Climate Research Program, Boulder, Colorado, 263 pp.

Smith, R.C., and W.H. Wilson, 1981: Ship and satellite bio-optical research in the California Bight. *Oceanography from Space,* J.F.R. Gower, Ed., Plenum Press, New York, 281–294.

——, B.B. Prézelin, K.S. Baker, R.R. Bidigare, N.P. Boucher, T. Coley, D. Karentz, S. MacIntyre, H.A. Matlick, D. Menzies, M. Ondrusek, Z. Wan and K.J. Waters, 1992: Ozone depletion: Ultraviolet radiation and phytoplankton biology in Antarctic waters. *Science,* **255,** 952–959.

Sørensen, B., 1981: Recommendations of the 2nd international workshop on atmospheric correction of satellite observation of sea water colour. March 30–April 1, Ispra, Italy, 49 pp.

Sturm, B., 1981: The atmospheric correction of remotely sensed data and the quantitative determination of suspended matter in marine water surface layers. *Rem. Sens. in Meteor., Oceanogr., and Hydrol.,* A.P. Cracknell, Ed., John Wiley & Sons, 163–197.

——, 1993: CZCS data processing algorithms. *Ocean Colour: Theory and Applications in a Decade of CZCS Experience,* V. Barale and P.M. Schlittenhardt (Eds.), ECSC, EEC, EAEC, Brussels and Luxembourg, Kluwer Academic Publishers, Norwell, Massachusetts, 95–116.

Sullivan, C.W., C.R. McClain, J.C. Comiso, and W.O. Smith, Jr., 1988: Phytoplankton standing crops within an Antarctic ice edge assessed by satellite remote sensing. *J. Geophys. Res.,* **93,** 12,487–12,498.

University of Illinois at Urbana-Champaign, 1989: *NCSA HDF Specification.* 43 pp.

——, 1993: *NCSA HDF Calling Interfaces and Utilities, Version 3.2.* 121 pp.

Viollier, M., D. Tanré, and P.Y. Deschamps, 1980: An algorithm for remote sensing of water color from space. *Bound.-Layer Meteor.,* **18,** 247–267.

Williams, S.P., E.F. Szajna, and W.A. Hovis, 1985: Nimbus 7 Coastal Zone Color Scanner (CZCS), Level 2 Data Product Users' Guide. *NASA Tech. Memo. 86202,* NASA Goddard Space Flight Center, Greenbelt, Maryland, 57 pp.

Woodruff, S.D., R.J. Slutz, R.L. Jenne, and P.M. Steurer, 1987: A comprehensive ocean-atmosphere data set. *Bull. Am. Meteor. Soc.,* **68,** 1,239–1,250.

Woodward, R.H., R.A. Barnes, C.R. McClain, W.E. Esaias, W.L. Barnes, and A.T. Mecherikunnel, 1993: Modeling of the SeaWiFS Solar and Lunar Observations. *NASA Tech. Memo. 104566, Vol. 10,* S.B. Hooker and E.R. Firestone, Eds., NASA Goddard Space Flight Center, Greenbelt, Maryland, 26 pp.

The SeaWiFS Technical Report Series

Vol. 1

Hooker, S.B., W.E. Esaias, G.C. Feldman, W.W. Gregg, and C.R. McClain, 1992: An Overview of SeaWiFS and Ocean Color. *NASA Tech. Memo. 104566, Vol. 1,* S.B. Hooker and E.R. Firestone, Eds., NASA Goddard Space Flight Center, Greenbelt, Maryland, 24 pp., plus color plates.

Vol. 2

Gregg, W.W., 1992: Analysis of Orbit Selection for SeaWiFS: Ascending vs. Descending Node. *NASA Tech. Memo. 104566, Vol. 2,* S.B. Hooker and E.R. Firestone, Eds., NASA Goddard Space Flight Center, Greenbelt, Maryland, 16 pp.

Vol. 3

McClain, C.R., W.E. Esaias, W. Barnes, B. Guenther, D. Endres, S. Hooker, G. Mitchell, and R. Barnes, 1992: Calibration and Validation Plan for SeaWiFS. *NASA Tech. Memo. 104566, Vol. 3,* S.B. Hooker and E.R. Firestone, Eds., NASA Goddard Space Flight Center, Greenbelt, Maryland, 41 pp.

Vol. 4

McClain, C.R., E. Yeh, and G. Fu, 1992: An Analysis of GAC Sampling Algorithms: A Case Study. *NASA Tech. Memo. 104566, Vol. 4,* S.B. Hooker and E.R. Firestone, Eds., NASA Goddard Space Flight Center, Greenbelt, Maryland, 22 pp., plus color plates.

Vol. 5

Mueller, J.L., and R.W. Austin, 1992: Ocean Optics Protocols. *NASA Tech. Memo. 104566, Vol. 5,* S.B. Hooker and E.R. Firestone, Eds., NASA Goddard Space Flight Center, Greenbelt, Maryland, 43 pp.

Vol. 6

Firestone, E.R., and S.B. Hooker, 1992: SeaWiFS Technical Report Series Summary Index: Volumes 1–5. *NASA Tech. Memo. 104566, Vol. 6,* S.B. Hooker and E.R. Firestone, Eds., NASA Goddard Space Flight Center, Greenbelt, Maryland, 9 pp.

<u>Vol. 7</u>

Darzi, M., 1992: Cloud Screening for Polar Orbiting Visible and IR Satellite Sensors. *NASA Tech. Memo. 104566, Vol. 7,* S.B. Hooker and E.R. Firestone, Eds., NASA Goddard Space Flight Center, Greenbelt, Maryland, 7 pp.

<u>Vol. 8</u>

Hooker, S.B., W.E. Esaias, and L.A. Rexrode, 1993: Proceedings of the First SeaWiFS Science Team Meeting. *NASA Tech. Memo. 104566, Vol. 8,* S.B. Hooker and E.R. Firestone, Eds., NASA Goddard Space Flight Center, Greenbelt, Maryland, 61 pp.

<u>Vol. 9</u>

Gregg, W.W., F.C. Chen, A.L. Mezaache, J.D. Chen, J.A. Whiting, 1993: The Simulated SeaWiFS Data Set, Version 1. *NASA Tech. Memo. 104566, Vol. 9,* S.B. Hooker and E.R. Firestone, Eds., NASA Goddard Space Flight Center, Greenbelt, Maryland, 17 pp.

<u>Vol. 10</u>

Woodward, R.H., R.A. Barnes, C.R. McClain, W.E. Esaias, W.L. Barnes, and A.T. Mecherikunnel, 1993: Modeling of the SeaWiFS Solar and Lunar Observations. *NASA Tech. Memo. 104566, Vol. 10,* S.B. Hooker and E.R. Firestone, Eds., NASA Goddard Space Flight Center, Greenbelt, Maryland, 26 pp.

<u>Vol. 11</u>

Patt, F.S., C.M. Hoisington, W.W. Gregg, and P.L. Coronado, 1993: Analysis of Selected Orbit Propagation Models for the SeaWiFS Mission. *NASA Tech. Memo. 104566, Vol. 11,* S.B. Hooker, E.R. Firestone, and A.W. Indest, Eds., NASA Goddard Space Flight Center, Greenbelt, Maryland, 16 pp.

<u>Vol. 12</u>

Firestone, E.R., and S.B. Hooker, 1993: SeaWiFS Technical Report Series Summary Index: Volumes 1–11. *NASA Tech. Memo. 104566, Vol. 12,* S.B. Hooker and E.R. Firestone, Eds., NASA Goddard Space Flight Center, Greenbelt, Maryland, 28 pp.

<u>Vol. 13</u>

McClain, C.R., K.R. Arrigo, J. Comiso, R. Fraser, M. Darzi, J.K. Firestone, B. Schieber, E-n. Yeh, and C.W. Sullivan, 1993: Case Studies for SeaWiFS Calibration and Validation, Part 1. *NASA Tech. Memo. 104566, Vol. 13,* S.B. Hooker and E.R. Firestone, Eds., NASA Goddard Space Flight Center, Greenbelt, Maryland, 52 pp., plus color plates.

C. McClain, J. Comiso, R. Fraser, J. Firestone, B. Schieber, E. Yeh, K. Arrigo, and C. Sullivan

COLOR PLATES
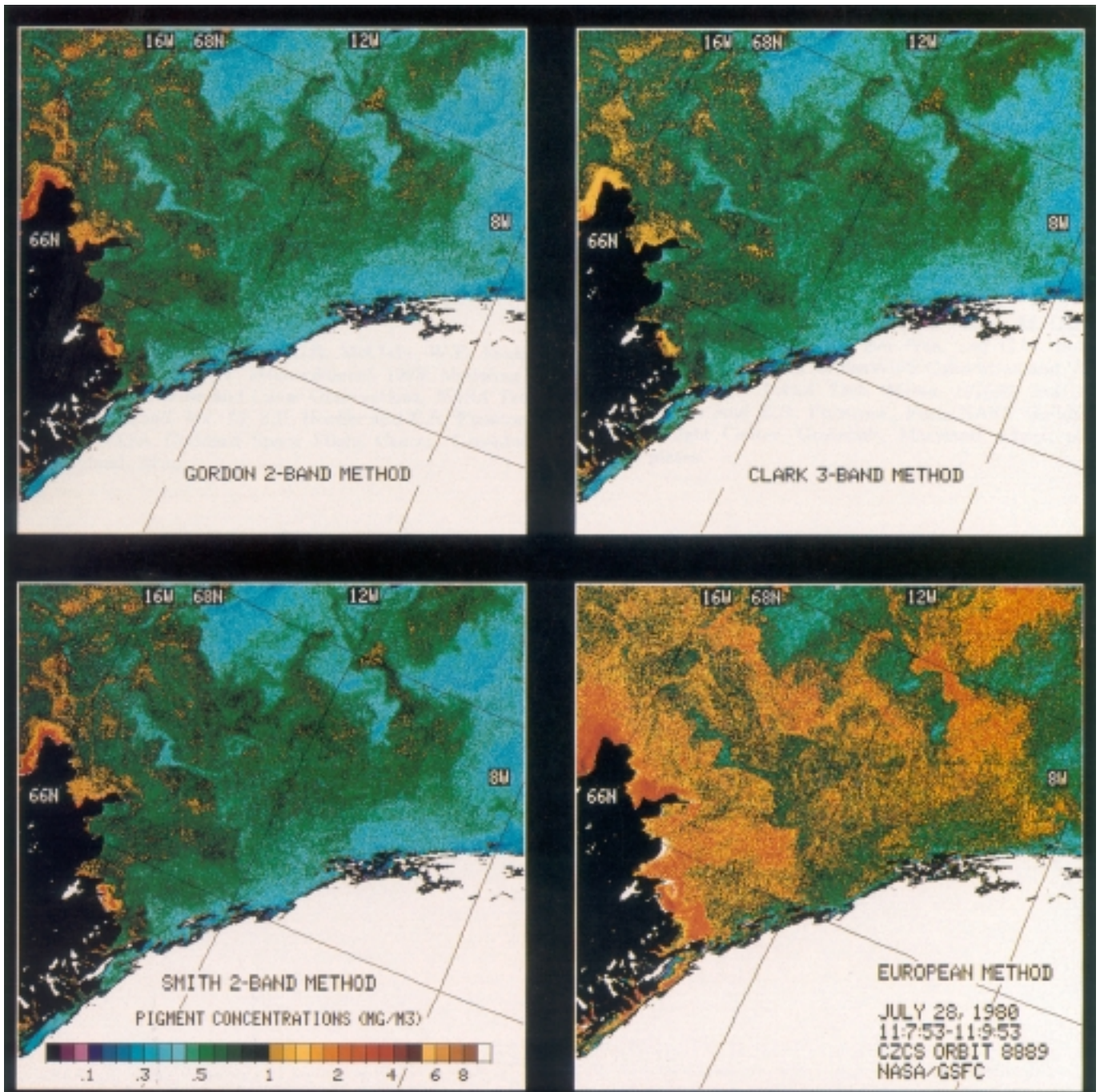
PLATE 1. Pigment concentration images derived for scene 1 using the Gordon 2-band, Clark 3-band, Smith-Wilson, and European methods.

C. McClain, J. Comiso, R. Fraser, J. Firestone, B. Schieber, E. Yeh, K. Arrigo, and C. Sullivan
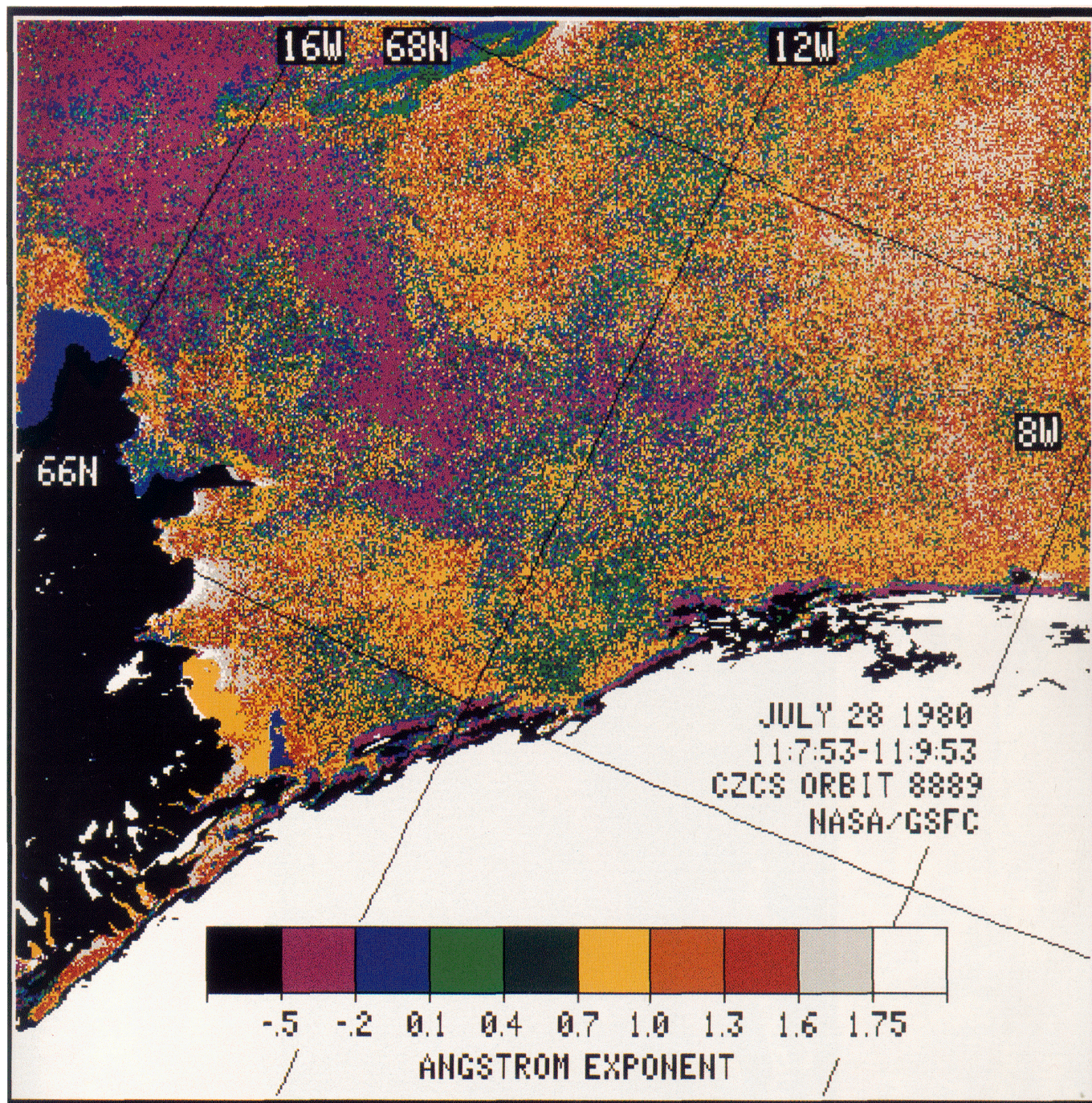
PLATE 2. The Ångström exponents derived from the European method for scene 1.
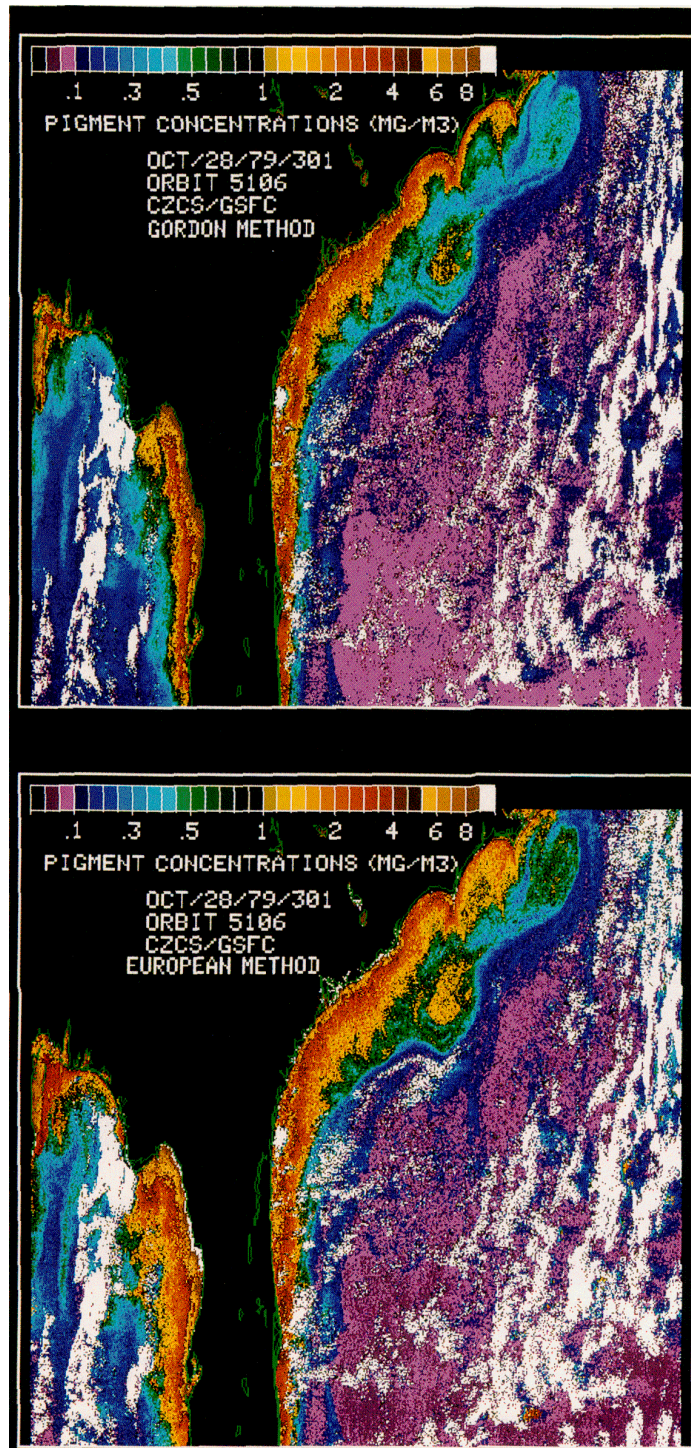
PLATE 3. Pigment concentration images derived for scene 2 using the Gordon 2-band and European methods.

C. McClain, J. Comiso, R. Fraser, J. Firestone, B. Schieber, E. Yeh, K. Arrigo, and C. Sullivan
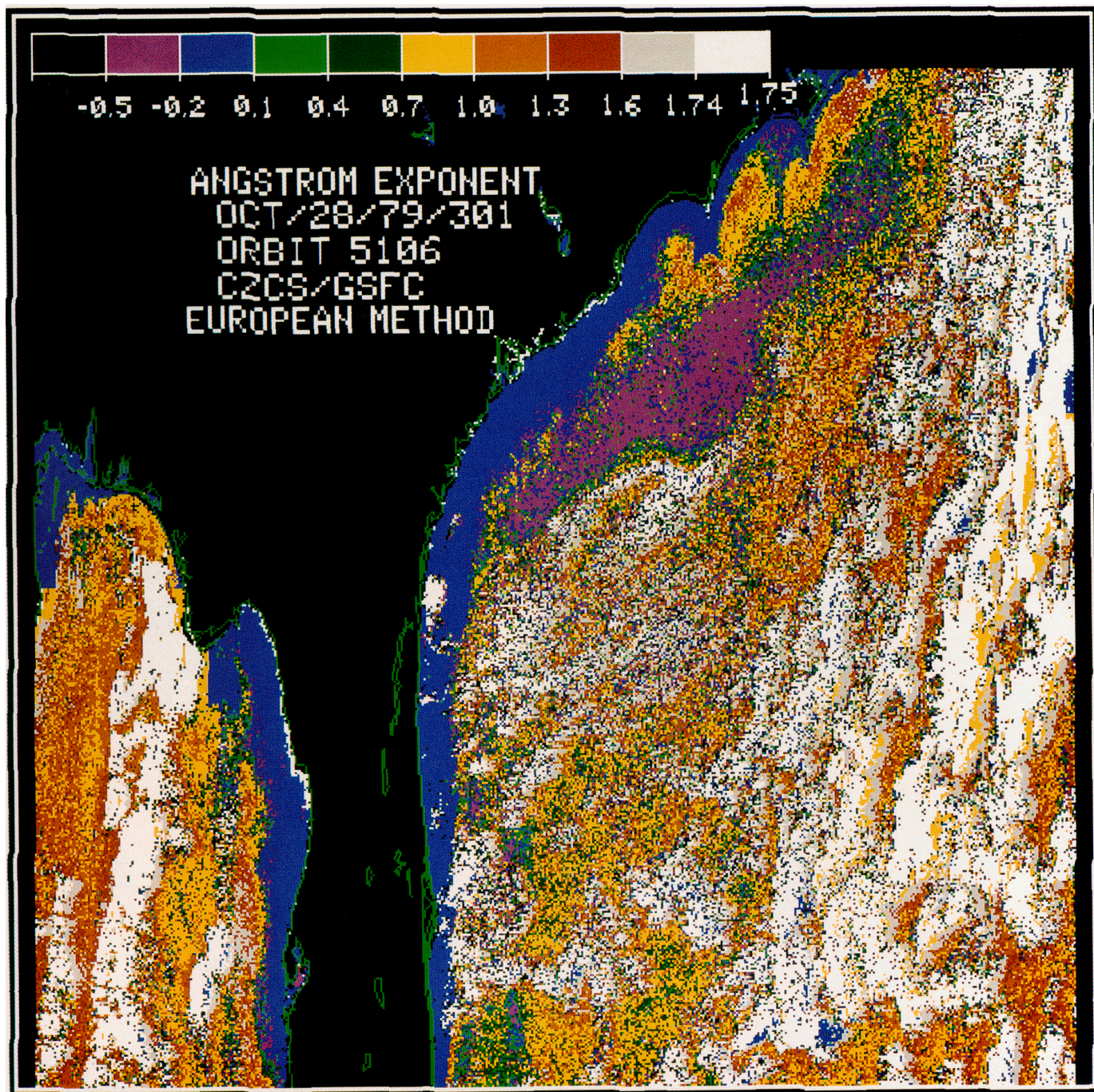
PLATE 4. The Ångström exponent derived from the European method for scene 2.
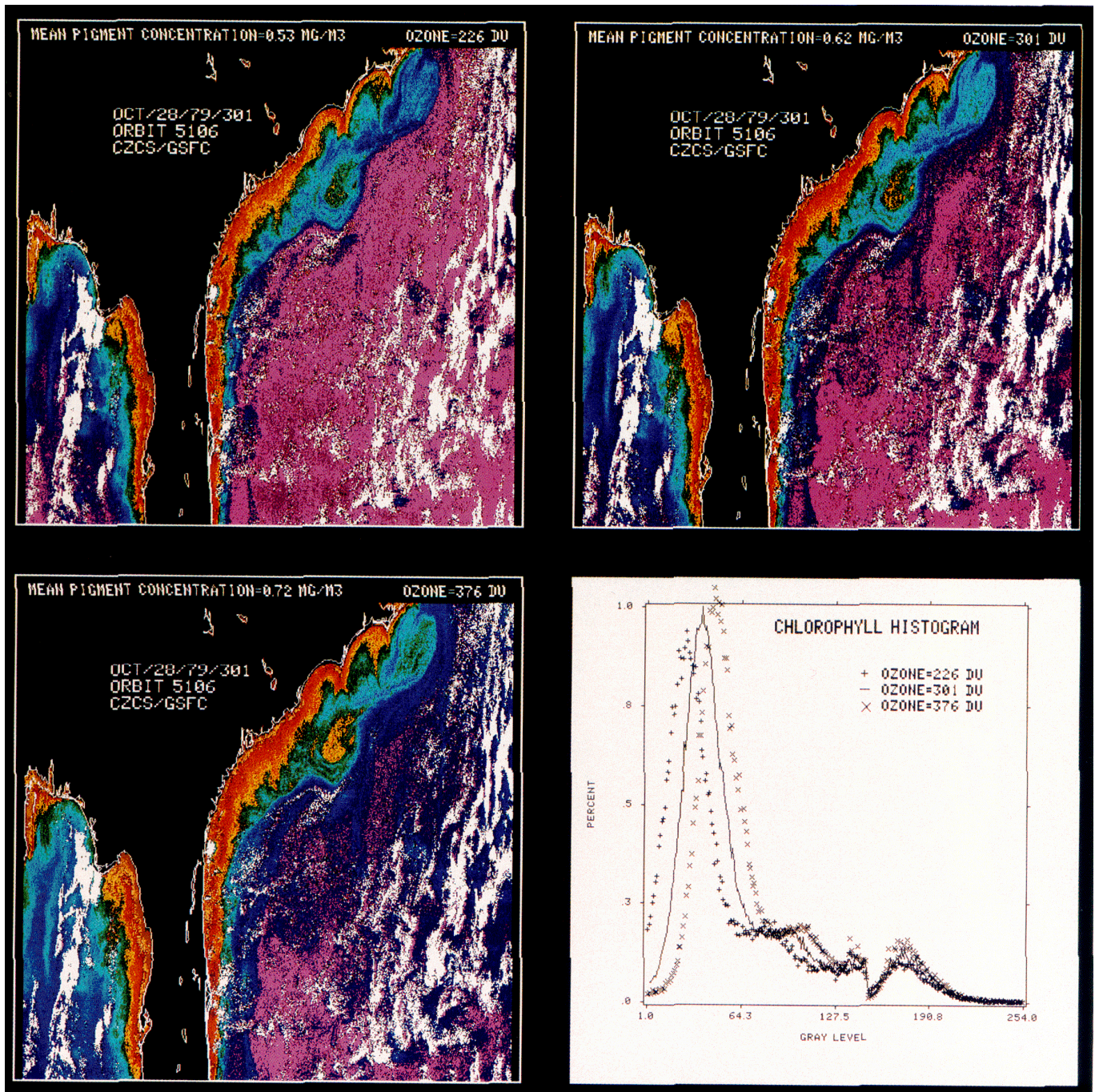
PLATE 5. Composite of three pigment concentration images using three different ozone concentrations and the frequency distributions of log[pigment concentration]. The color ranges are 0–0.10 (purple hues), 0.10–0.45 (blue hues), 0.45–1.0 (green hues), 1.0–1.6 (yellow hues), 1.6–3.0 (orange hues), 3.0–4.5 (red hues), greater than 4.5 (brown hues). Mean pigment concentrations for the entire image and the ozone concentration are given at the top of each panel.

C. McClain, J. Comiso, R. Fraser, J. Firestone, B. Schieber, E. Yeh, K. Arrigo, and C. Sullivan
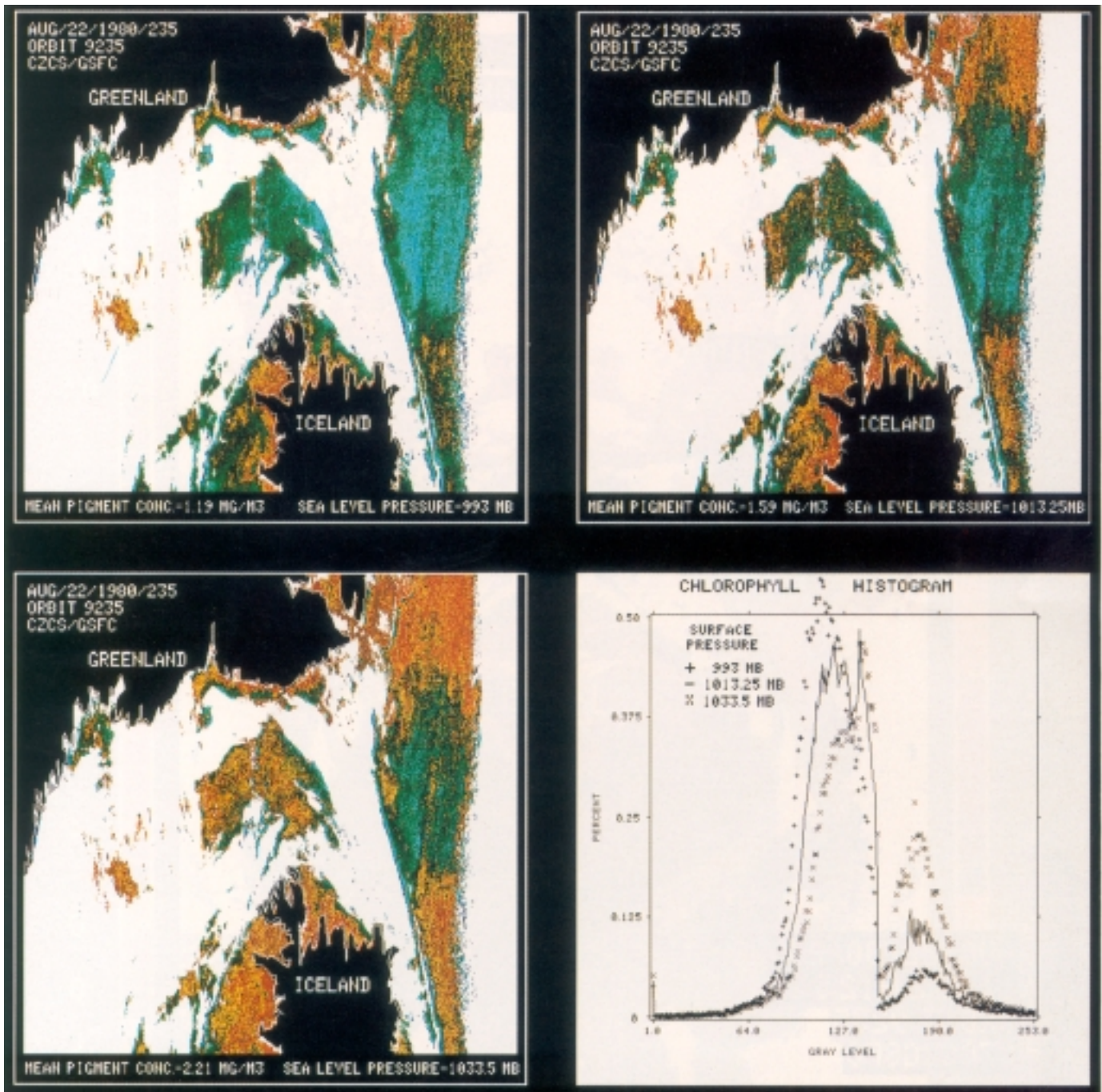
PLATE 6. Composite of three pigment concentration images using three different surface pressures and the frequency distributions of log[pigment concentration]. The color ranges are 0–0.10 (purple hues), 0.10–0.45 (blue hues), 0.45–1.0 (green hues), 1.0–1.6 (yellow hues), 1.6–3.0 (orange hues), 3.0–4.5 (red hues), greater than 4.5 (brown hues). Mean pigment concentrations for the entire image and the surface pressure are given at the bottom of each panel. The fourth panel shows the frequency distributions of log[pigment] for the three analyses.
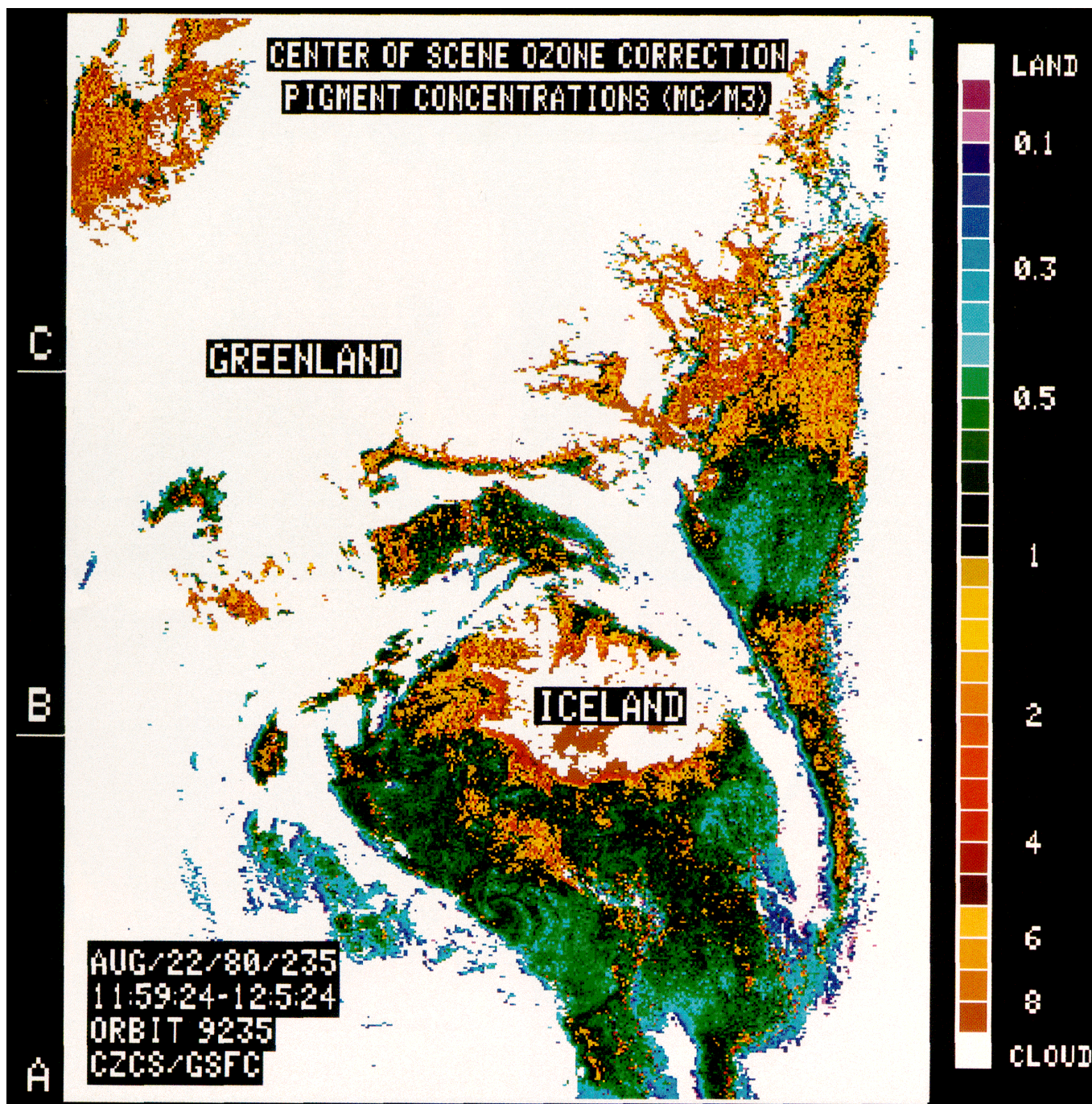
PLATE 7. Pigment concentration image derived using center of scene ozone and standard surface pressure values.

C. McClain, J. Comiso, R. Fraser, J. Firestone, B. Schieber, E. Yeh, K. Arrigo, and C. Sullivan
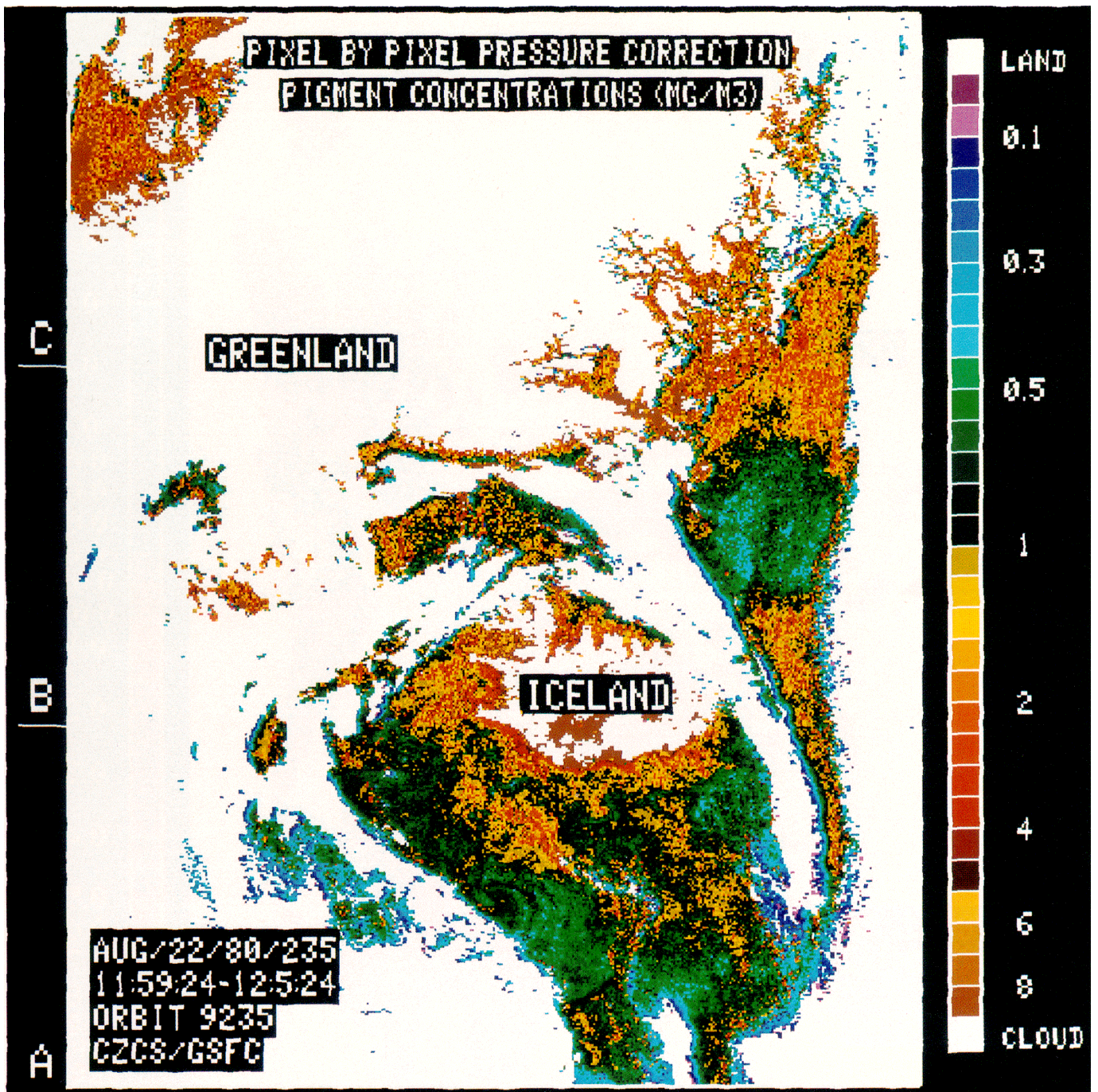
PLATE 8. Pigment concentration image derived using a pixel-by-pixel pressure correction and the center of scene ozone value.
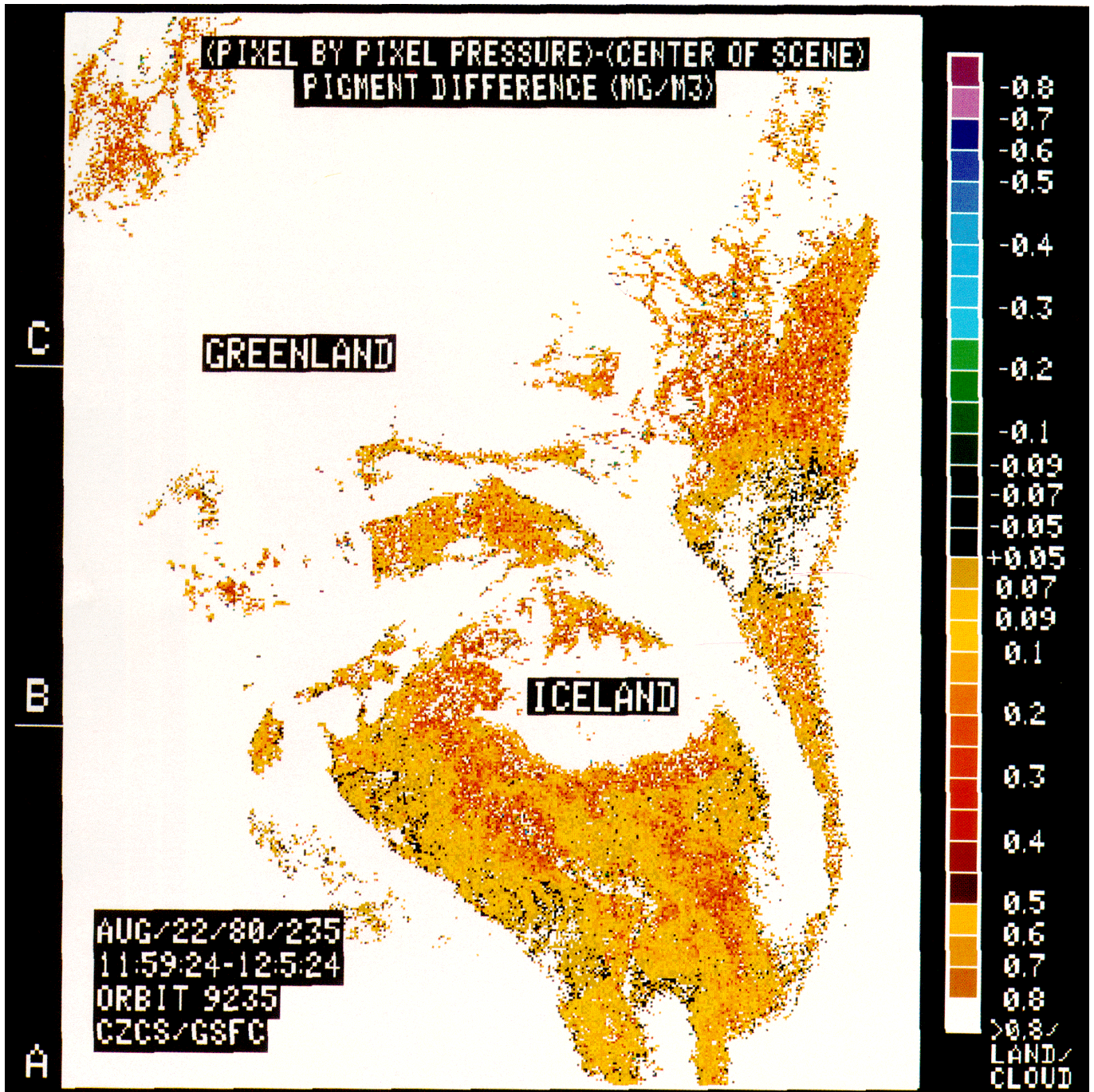
PLATE 9. Pigment concentration difference image, Plate 8 minus Plate 7.

C. McClain, J. Comiso, R. Fraser, J. Firestone, B. Schieber, E. Yeh, K. Arrigo, and C. Sullivan
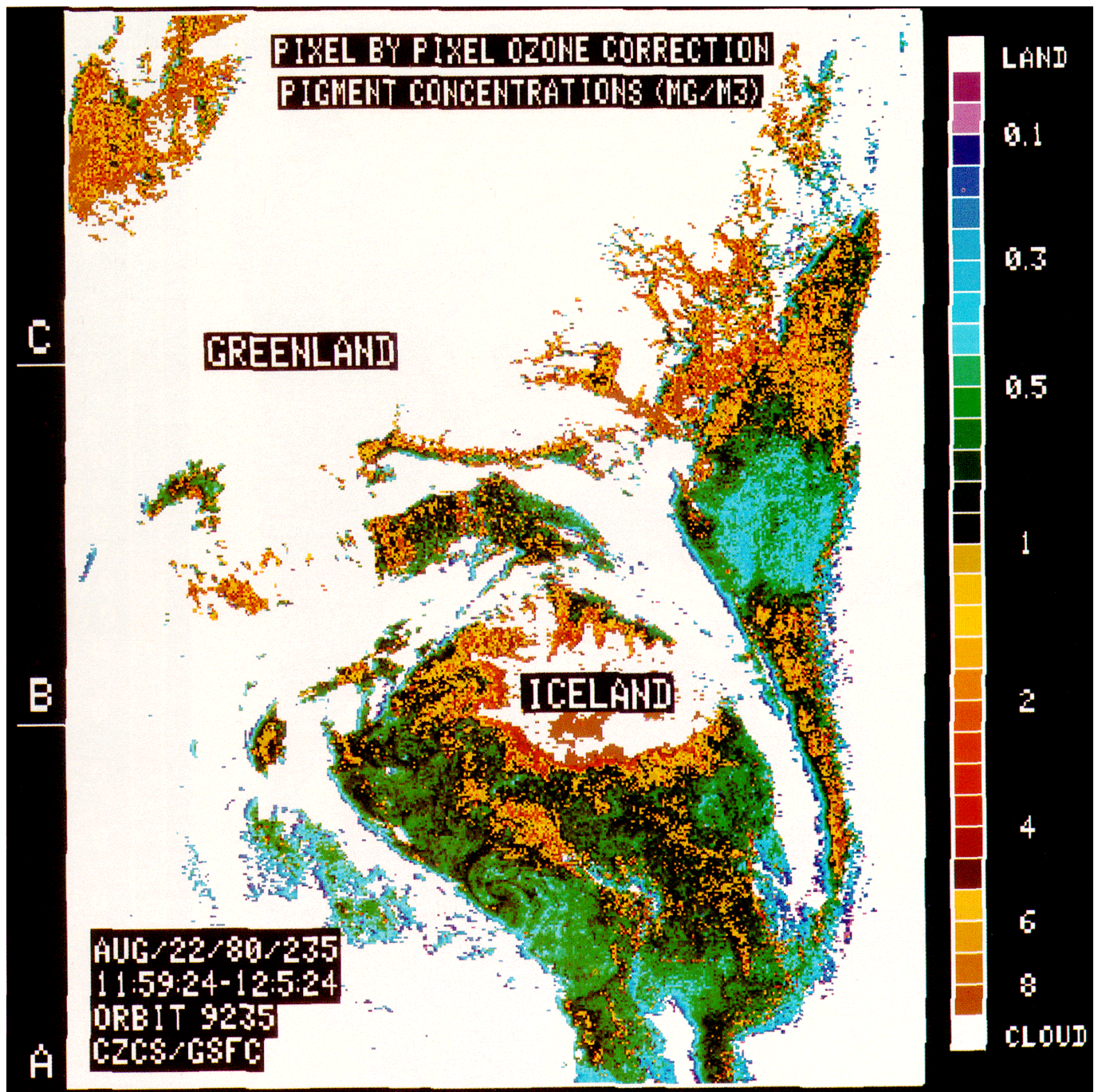
PLATE 10. Pigment concentration image derived using a pixel-by-pixel ozone correction and a standard pressure value.
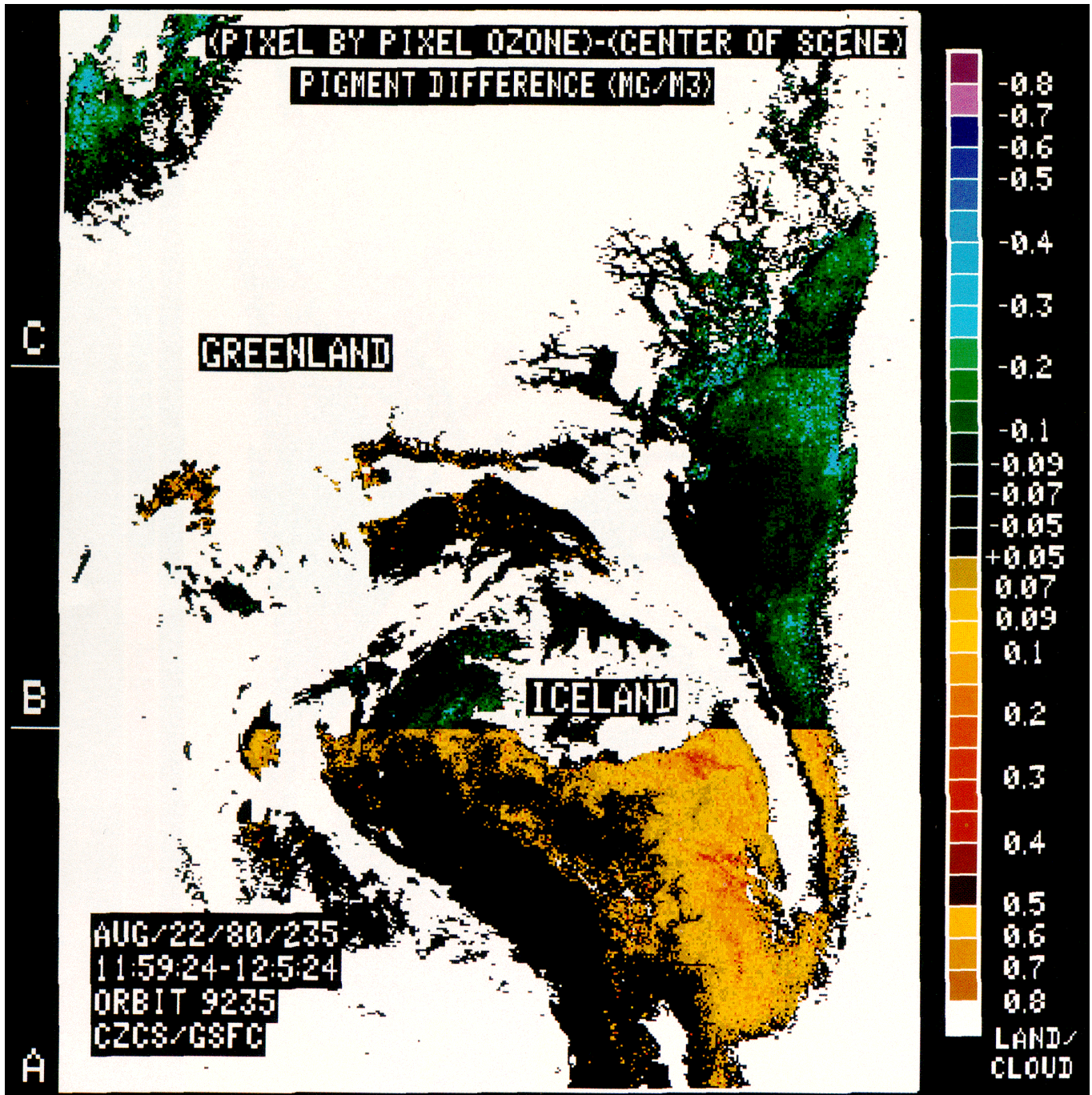
PLATE 11. Pigment concentration difference image, Plate 10 minus Plate 7.

C. McClain, J. Comiso, R. Fraser, J. Firestone, B. Schieber, E. Yeh, K. Arrigo, and C. Sullivan
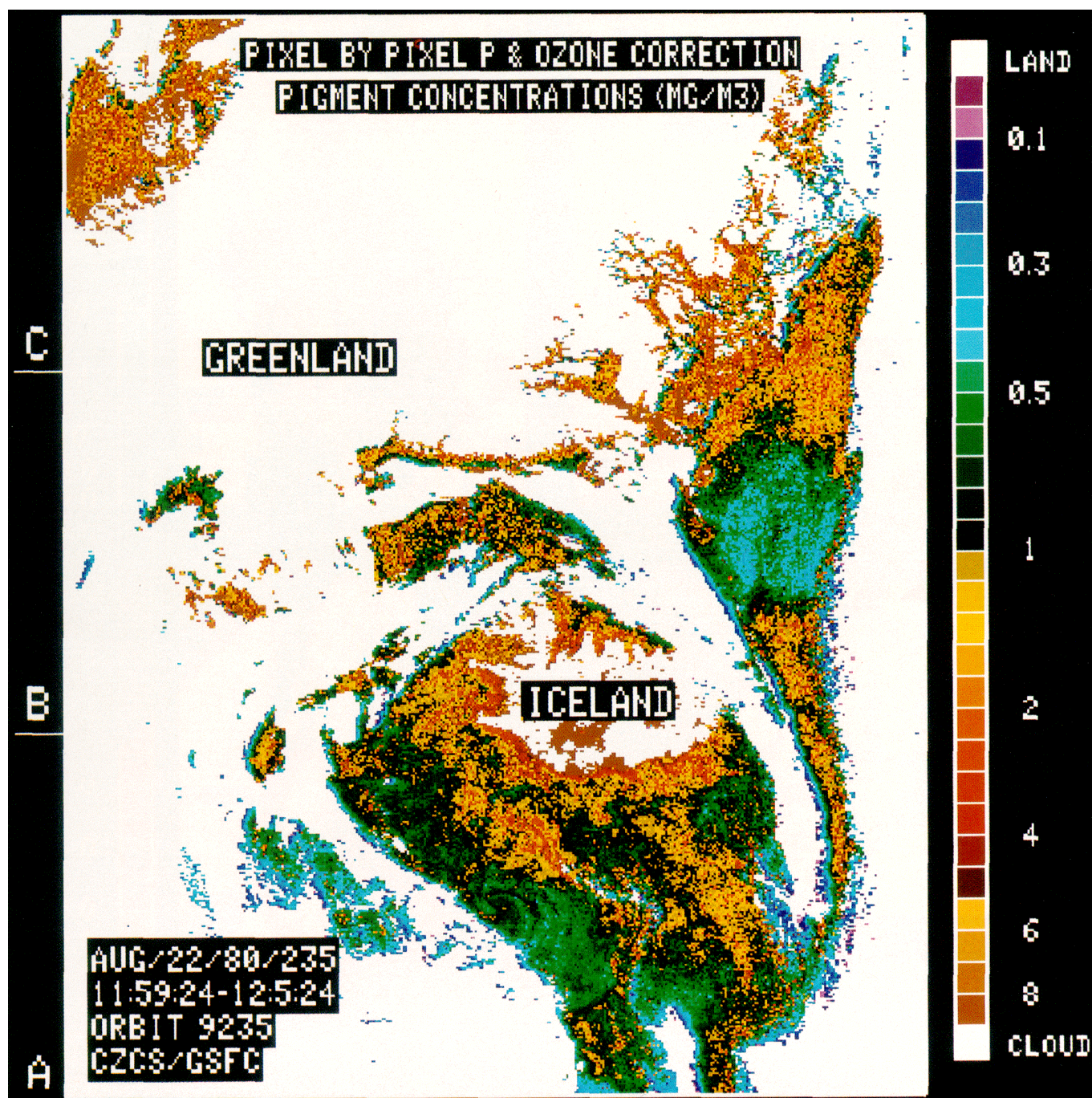
PLATE 12. Pigment concentration image derived using both pixel-by-pixel pressure and ozone corrections.
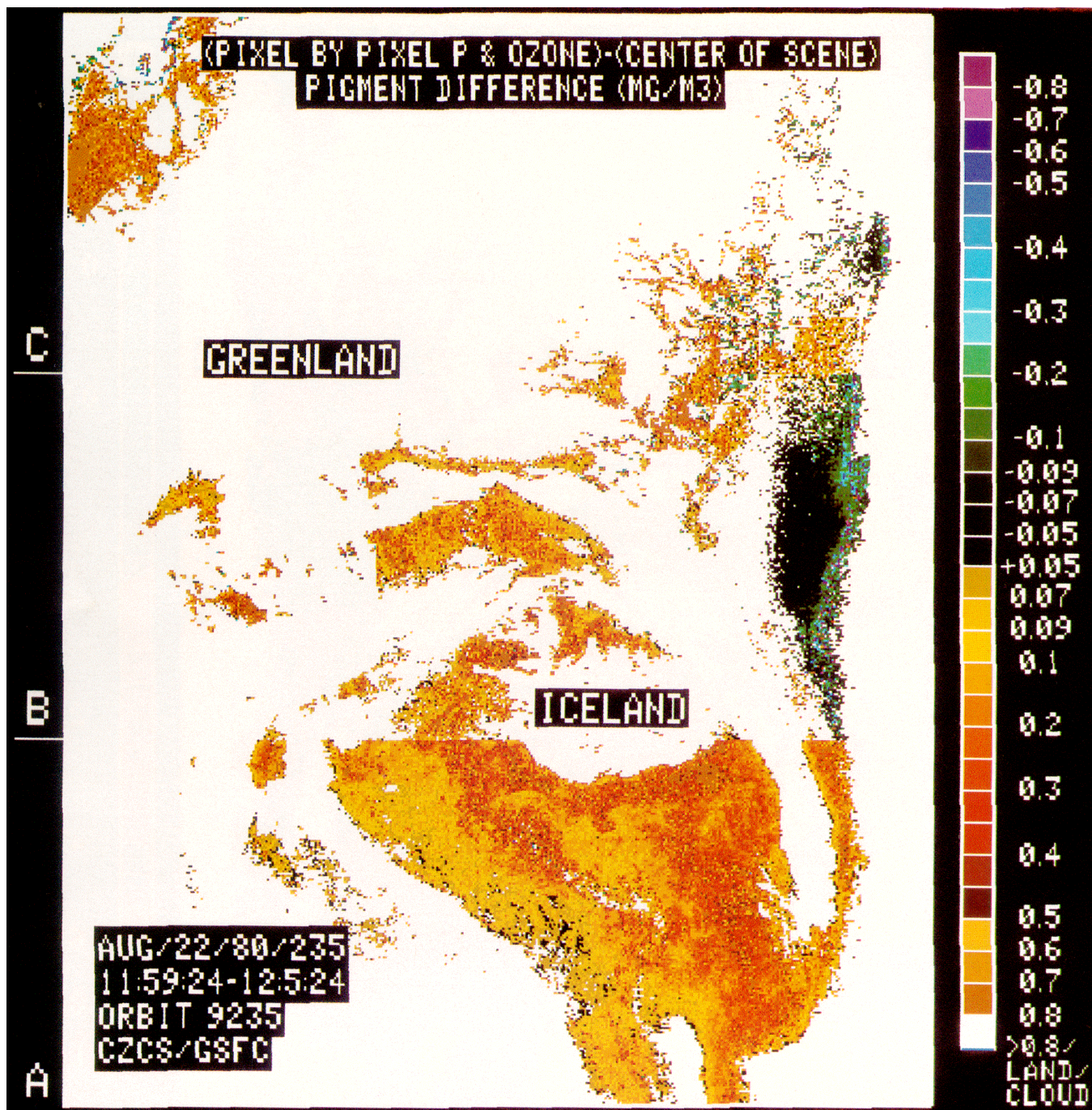
PLATE 13. Pigment concentration difference image, Plate 12 minus Plate 7.

C. McClain, J. Comiso, R. Fraser, J. Firestone, B. Schieber, E. Yeh, K. Arrigo, and C. Sullivan
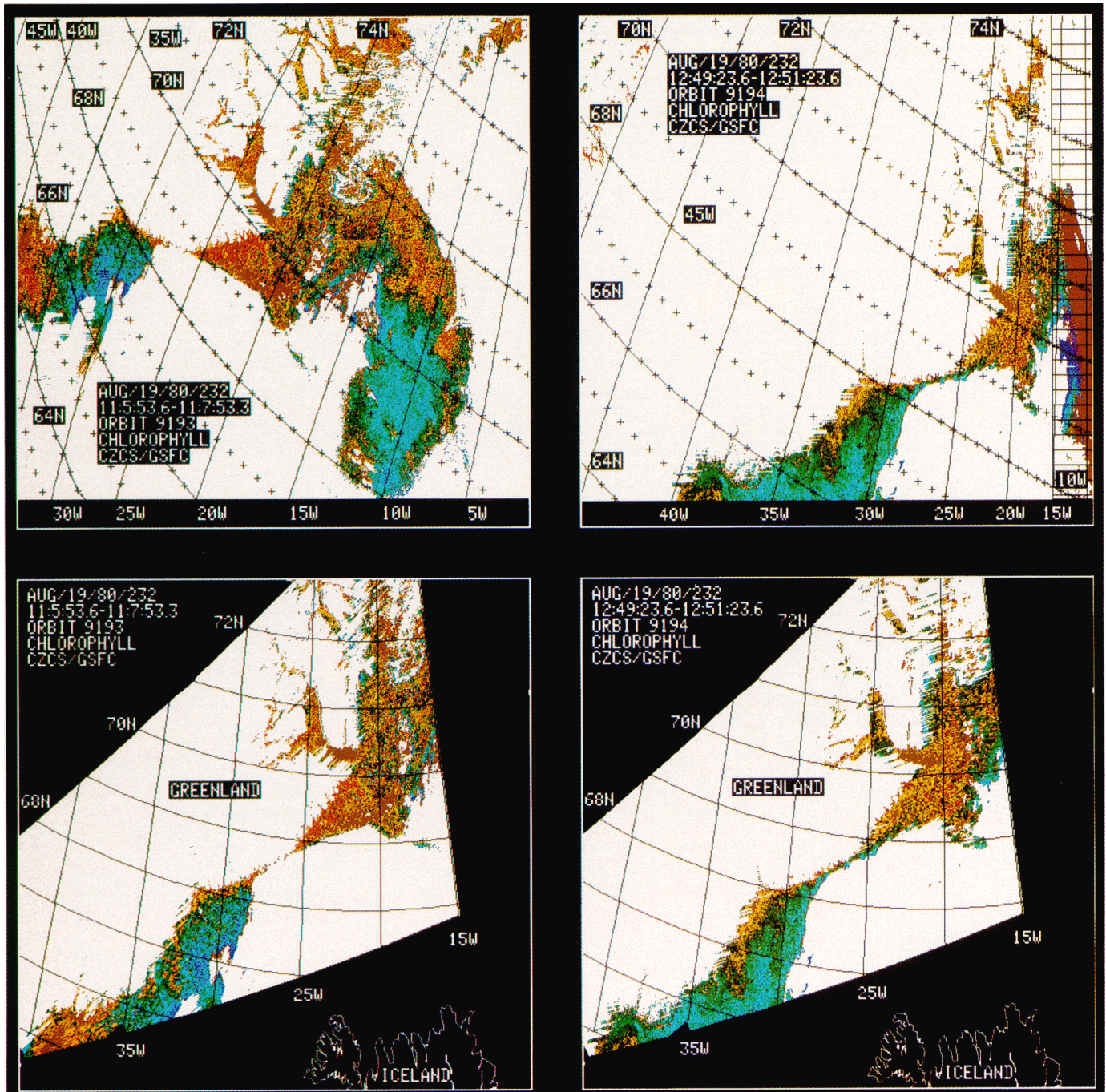
PLATE 14. Unmapped (upper two panels) and mapped (lower two panels) pigment concentration images. The color ranges are 0–0.10 (purple hues), 0.10–0.45 (blue hues), 0.45–1.0 (green hues), 1.0–1.6 (yellow hues), 1.6–3.0 (orange hues), 3.0–4.5 (red hues), greater than 4.5 (brown hues).
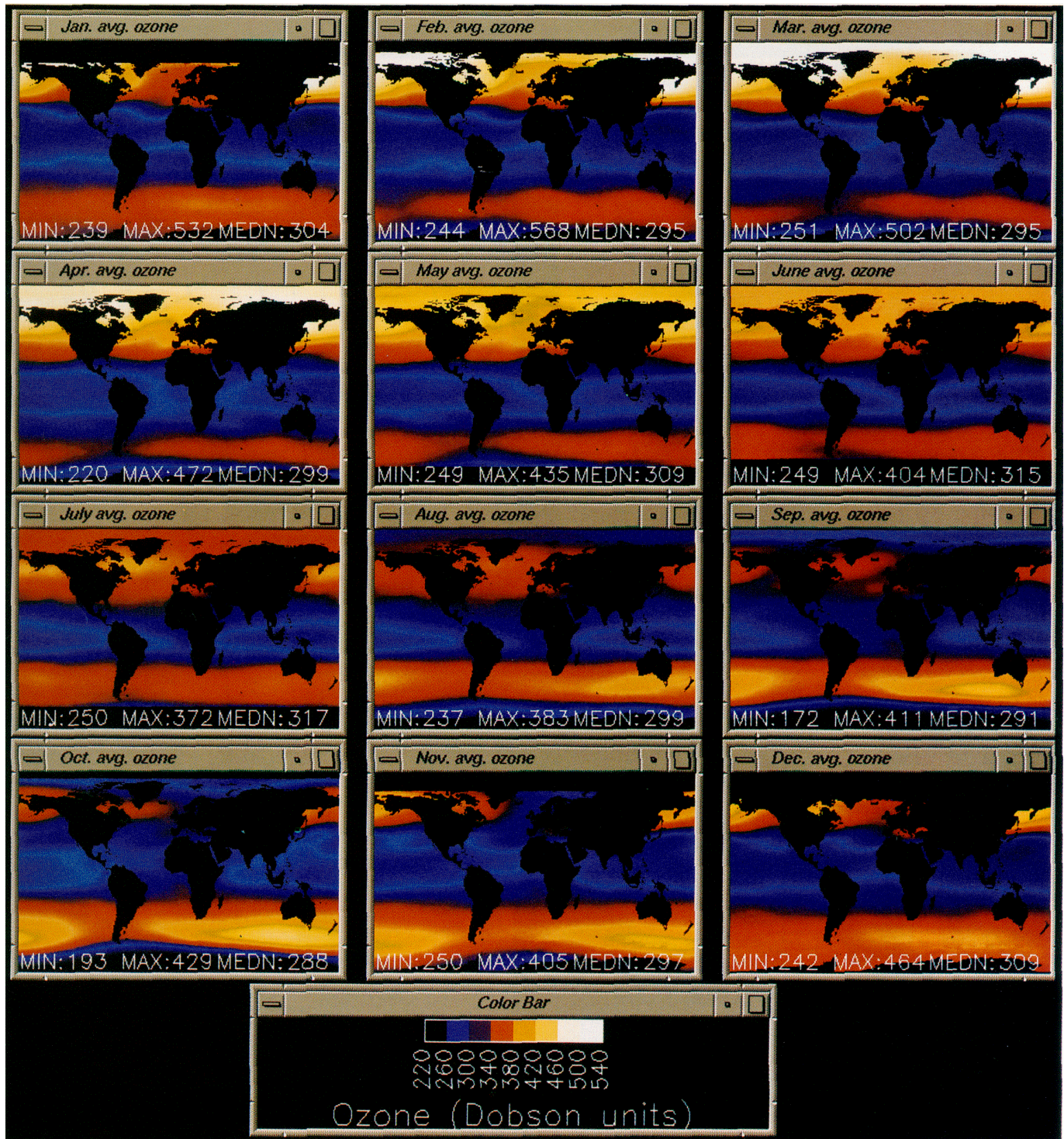
PLATE 15. Monthly average total ozone images, based on data from NIMBUS-7 TOMS collected between November 1978 and January 1992. The images were generated with SDSIMAGE and SDSNANIMATE, procedures written using IDL.

C. McClain, J. Comiso, R. Fraser, J. Firestone, B. Schieber, E. Yeh, K. Arrigo, and C. Sullivan

PLATE 16. Monthly average surface wind speed images, based on data from COADS between 1946 and 1990. The images were generated with `SDSIMAGE` and `SDSANIMATE`, procedures written using IDL.
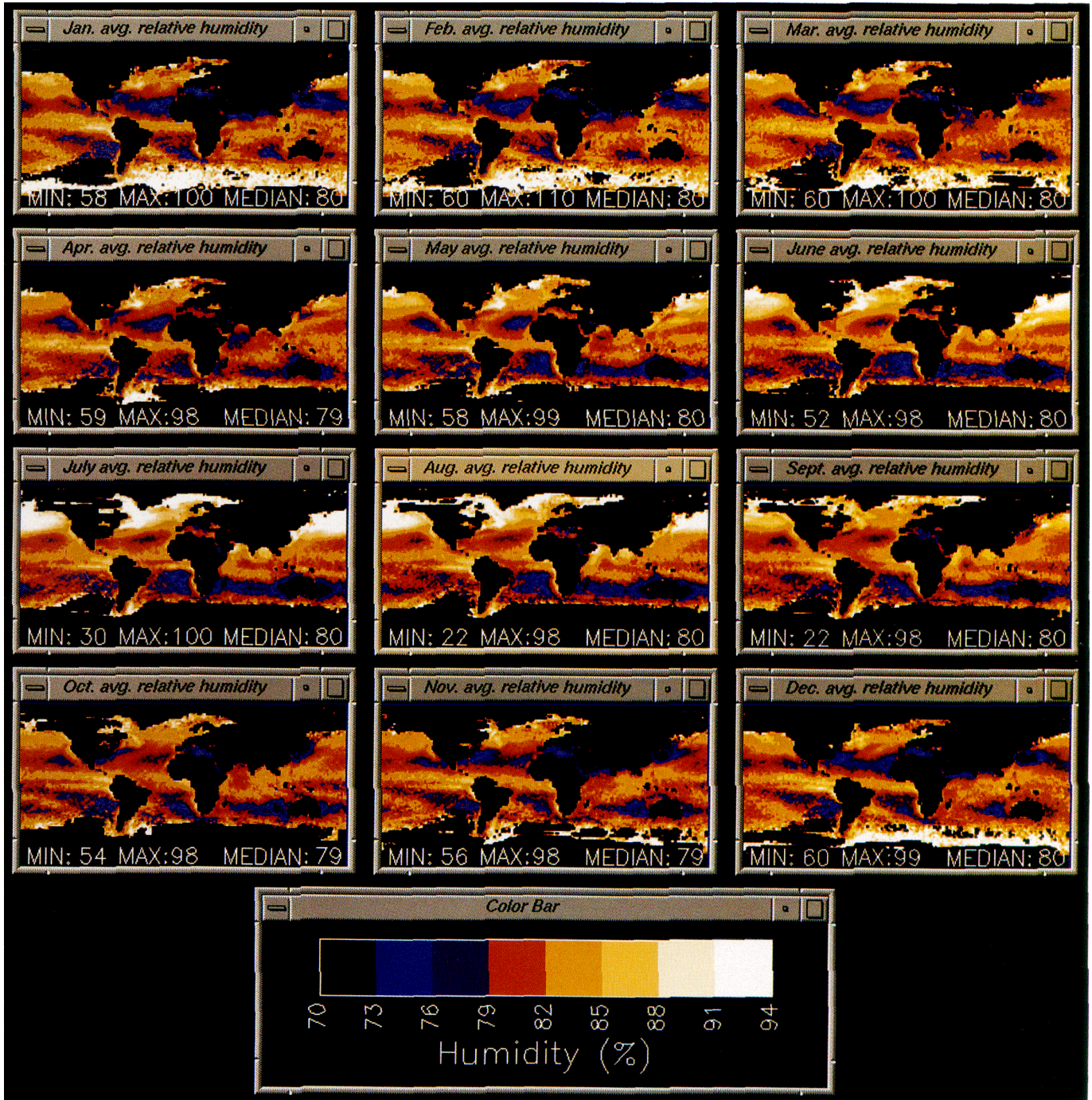
PLATE 17. Similar to Plate 16, except illustrates monthly average surface pressure images.

C. McClain, J. Comiso, R. Fraser, J. Firestone, B. Schieber, E. Yeh, K. Arrigo, and C. Sullivan
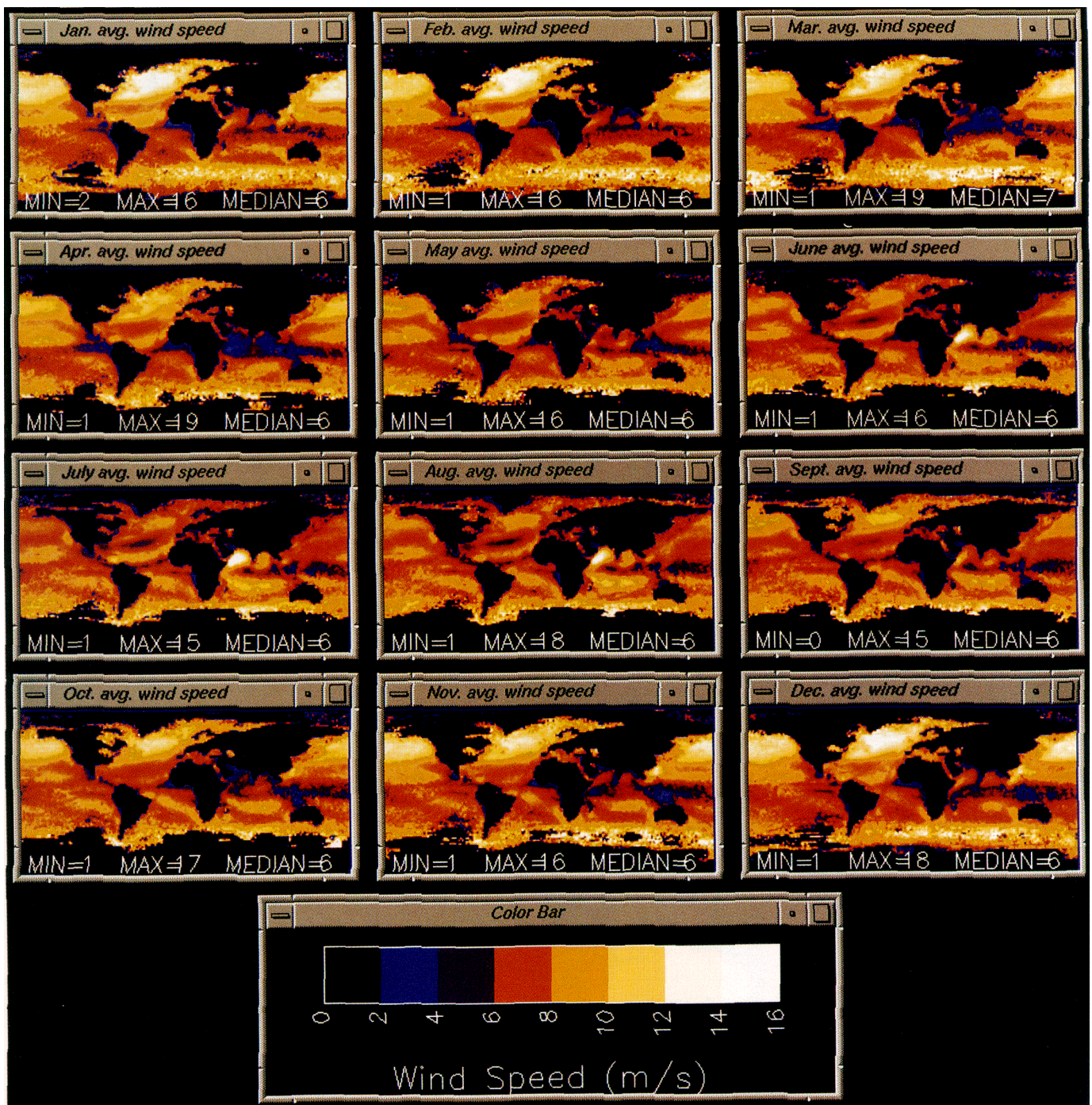
PLATE 18. Similar to Plate 16, except illustrates monthly average surface relative humidity images.
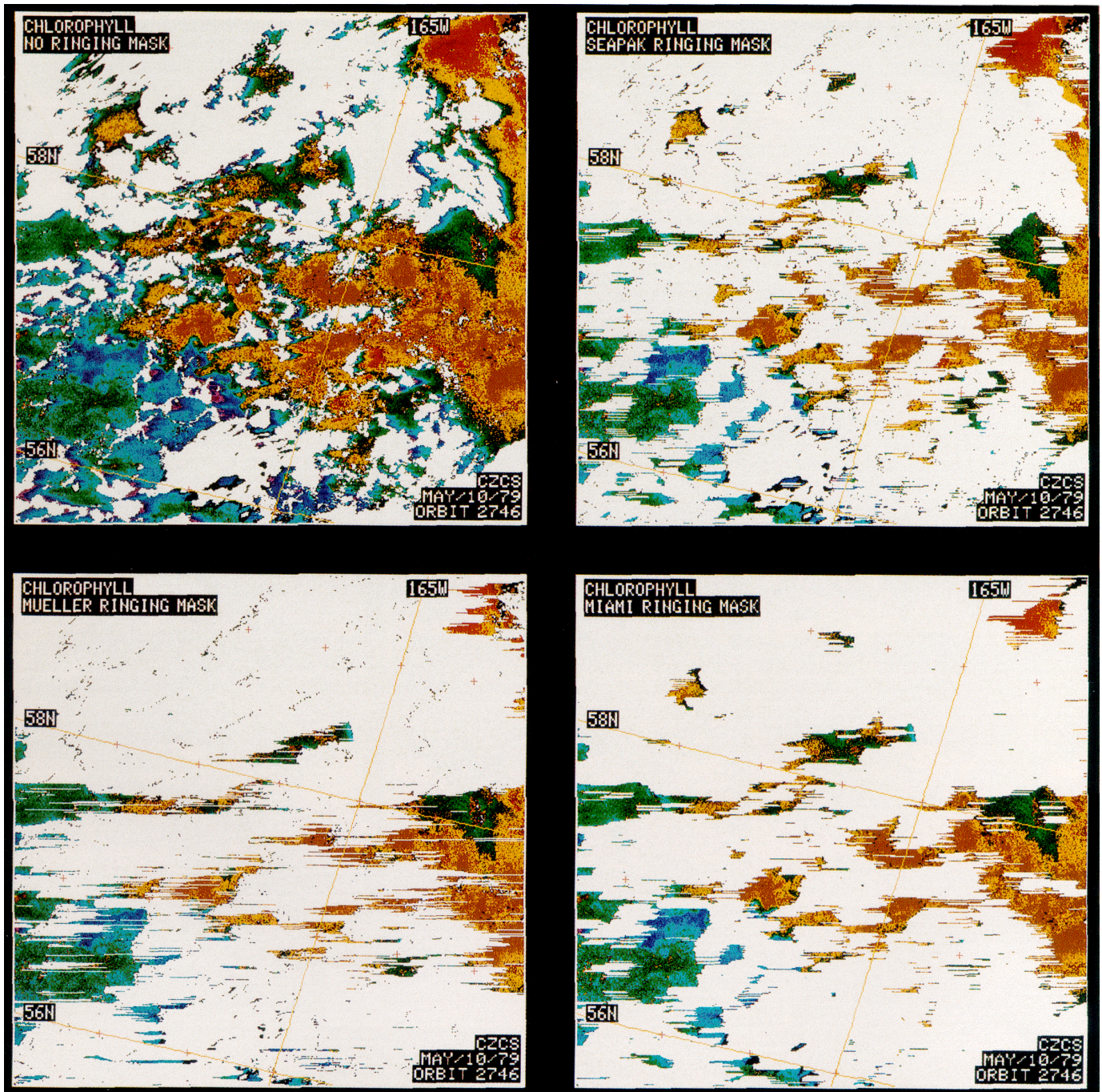
PLATE 19. Pigment concentration images using no ringing mask, the SEAPAK mask (`DISTANCE=20`), the Mueller mask, and the Miami DSP mask generation methods.

C. McClain, J. Comiso, R. Fraser, J. Firestone, B. Schieber, E. Yeh, K. Arrigo, and C. Sullivan
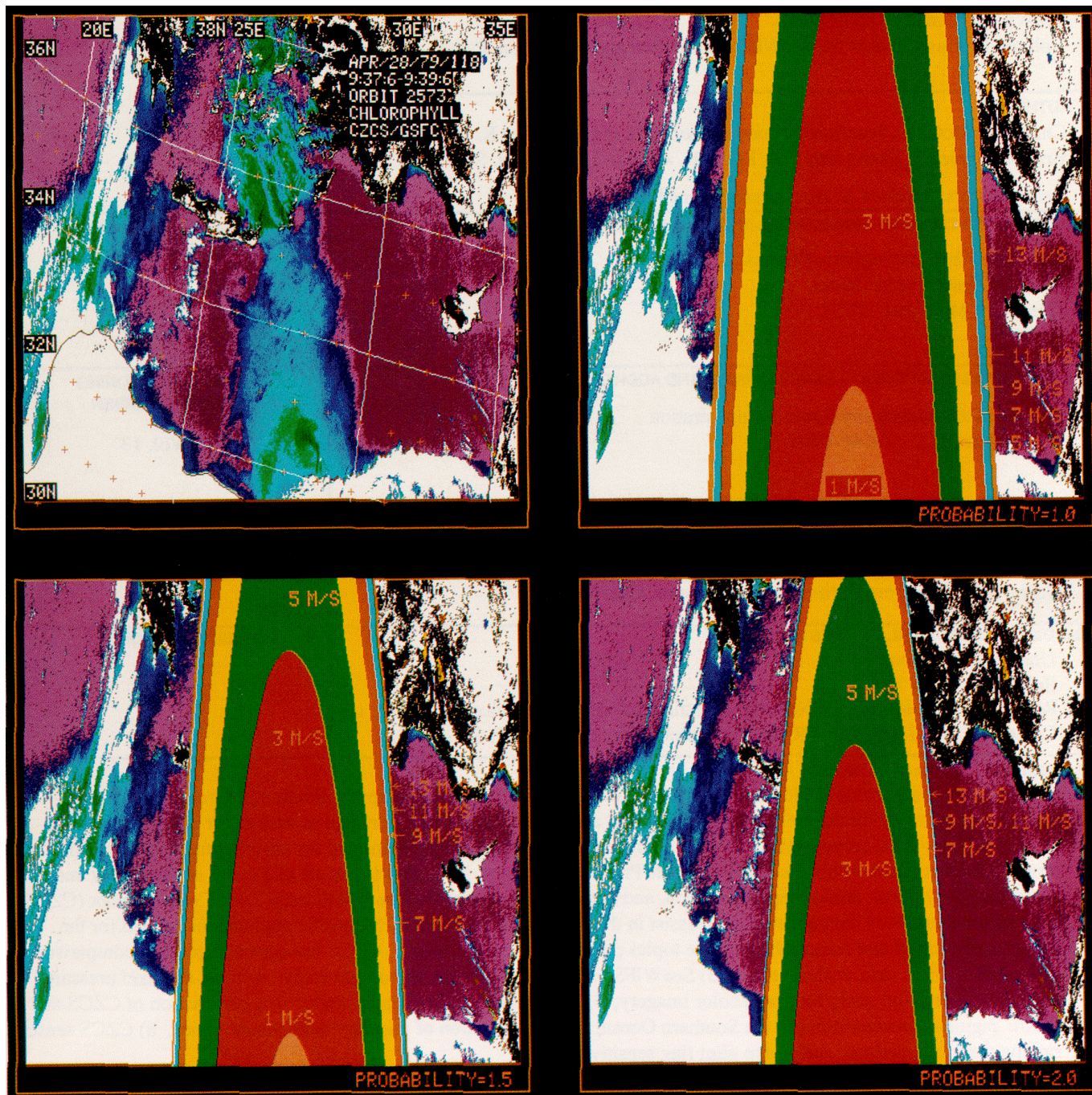
PLATE 20. Unmasked (upper left panel) and sun glint flagged (upper right and lower two panels) pigment concentration images. Color ranges are 0–0.10 (purple hues), 0.10–0.45 (blue hues), 0.45–1.0 (green hues). Wind speeds to generate the glint flags are 1 (pink), 3 (red), 5 (green), 7 (yellow), 9 (orange), 11 (cyan), and $13\,\mathrm{m\ s^{-1}}$ (tan).

REPORT DOCUMENTATION PAGE

1. AGENCY USE ONLY *(Leave blank)*	2. REPORT DATE December 1993	3. REPORT TYPE AND DATES COVERED Technical Memorandum

4. TITLE AND SUBTITLE
SeaWiFS Technical Report Series
Volume 13–Case Studies for SeaWiFS Calibration and Validation, Part 1

5. FUNDING NUMBERS

6. AUTHOR(S)
Charles R. McClain, Josefino C. Comiso, Robert S. Fraser, James K. Firestone,
Brian D. Schieber, Eueng-nan Yeh, Kevin R. Arrigo, Cornelius W. Sullivan

Series Editors: Stanford B. Hooker and Elaine R. Firestone

7. PERFORMING ORGANIZATION NAME(S) AND ADDRESS(ES)

Laboratory for Hydrospheric Processes
Goddard Space Flight Center
Greenbelt, Maryland 20771

8. PERFORMING ORGANIZATION REPORT NUMBER

94B00042
Code 970.2

9. SPONSORING/MONITORING AGENCY NAME(S) AND ADDRESS(ES)

National Aeronautics and Space Administration
Washington, D.C. 20546–0001

10. SPONSORING/MONITORING AGENCY REPORT NUMBER

TM–104566, Vol. 13

11. SUPPLEMENTARY NOTES
James K. Firestone, Brian D. Schieber, Eueng-nan Yeh, and Elaine R. Firestone: General Sciences Corporation, Laurel, Maryland; Kevin R. Arrigo: Oak Ridge Institute for Science and Education, Oak Ridge, Tennessee; Cornelius W. Sullivan: University of Southern California, Los Angeles, California..

12a. DISTRIBUTION/AVAILABILITY STATEMENT
Unclassified–Unlimited
Subject Category 48
Report is available from the Center for AeroSpace Information (CASI),
7121 Standard Drive, Hanover, MD 21076–1320; (301)621-0390

12b. DISTRIBUTION CODE

13. ABSTRACT *(Maximum 200 words)*

Although the Sea-viewing Wide Field-of-view Sensor (SeaWiFS) Calibration and Validation Program relies on the scientific community for the collection of bio-optical and atmospheric correction data as well as for algorithm development, it does have the responsibility for evaluating and comparing the algorithms and for ensuring that the algorithms are properly implemented within the SeaWiFS Data Processing System. This report consists of a series of sensitivity and algorithm (bio-optical, atmospheric correction, and quality control) studies based on Coastal Zone Color Scanner (CZCS) and historical ancillary data undertaken to assist in the development of SeaWiFS specific applications needed for the proper execution of that responsibility. The topics presented are as follows: 1) CZCS bio-optical algorithm comparison, 2) SeaWiFS ozone data analysis study, 3) SeaWiFS pressure and oxygen absorption study, 4) pixel-by-pixel pressure and ozone correction study for ocean color imagery, 5) CZCS overlapping scenes study, 6) a comparison of CZCS and *in situ* pigment concentrations in the Southern Ocean, 7) the generation of ancillary data climatologies, 8) CZCS sensor ringing mask comparison, and 9) sun glint flag sensitivity study.

14. SUBJECT TERMS SeaWiFS, Oceanography, Ocean Color, Bio-optical Algorithm, Ozone Data Analysis, Pressure, Oxygen, Absorption Study, Correction Study, Coastal Zone Color Scanner, CZCS, Pigment Concentration, Ancillary Data Climatologies, Sensor Ringing Mask, Sun Glint Flag

15. NUMBER OF PAGES
78

16. PRICE CODE

17. SECURITY CLASSIFICATION OF REPORT Unclassified	18. SECURITY CLASSIFICATION OF THIS PAGE Unclassified	19. SECURITY CLASSIFICATION OF ABSTRACT Unclassified	20. LIMITATION OF ABSTRACT Unlimited